An investigation of wave-dominated coral reef hydrodynamics

Thesis submitted by

Ron Karl Hoeke

Master of Physical Oceanography (Melbourne, Florida, USA)

In October 2010

for the degree of Doctor of Philosophy
School of Engineering and Physical Sciences
James Cook University

JAMES COOK UNIVERSITY
AUSTRALIA

Statement of the contributions of others

Research funding:

NOAA/University of Hawaii Joint Institute for Marine and Atmospheric Research (stipend for 3.5 years)	$72,000
US Geological Survey Coral Reef Project (project funding)	$40,000
AIMS@JCU (project funding)	$15,000
Graduate Research School, James Cook University	$2,800
NOAA Coral Reef Conservation Program (in kind support)	(NA)
US Geological Survey Coastal and Marine Geology (in kind support)	(NA)
NOAA Coral Reef Conservation Program (in kind support)	(NA)

Thesis committee:

Professor Peter Ridd, School of Engineering and Physical Sciences, James Cook University

Dr Richard Brinkman, Australian Institute of Marine Science

Professor Mark Merrifield, School of Ocean and Earth Science and Technology, University of Hawaii

Statistical and analytical support:

Dr. Curt Storlazzi (US Geological Survey)

Professor Peter Ridd

Dr. Jerome Aucan (Bermuda Institute of Ocean Science)

Dr. Edwin Elias (US Geological Survey)

Sean Vitousek (Stanford University)

Professor Mark Merrifield

Editorial support:

Professor Peter Ridd

Dr. Curt Storlazzi

Dr. Jerome Aucan

Professor Mark Merrifield

Dr. Gayle Kim Philip (University of Hawaii)

Amanda Toperoff (NOAA)

Dr. Rusty Brainard (NOAA)

Acknowledgements

First, I must thank my advisor Peter Ridd. He always provided insight and guidance, while maintaining good wit and cheer and, along with Thomas Stieglitz, showed me a bit of the Australian bush that I would have otherwise surely missed. Séverine Choukroun was a great fellow student who helped navigate the PhD candidature at James Cook University and to exchange research ideas with. I am also very appreciative of the academic and administrative assistance provided by the staff of the School of Engineering and the Graduate Research School, especially Barbara Pannach and Helene Marsh.

I owe big thanks to the support of the folks at the US Geological Survey's Marine and Coastal Geology Program, specifically to Edwin Elias, Mike Field, Josh Logan, Kathy Presto, and Curt Storlazzi. Without this support, the Hanalei Bay portion of this work would not have happened. In addition to material support, Curt in particular offered great encouragement and mentoring along the way.

I also owe big thanks to many people at the NOAA Pacific Islands Fisheries Science Center Coral Reef Ecosystem Division and the closely connected University of Hawaii's Joint Institute for Marine and Atmospheric Research. Rusty Brainard supported and encouraged my decision to return to graduate school; Kevin Wong kindly fostered my work towards the goals of the PhD research and also provided clear, lucid thinking on how to reach them. He, Lee Higa, Mike Seki, and especially Seema Balwani all helped steer the project through NOAA's requisite bureaucracy. John Rooney, Frances Lichowski, and Jonathon Weiss provided geospatial expertise, and Jake Asher, Marie Ferguson, and Frank Mancini picked project instruments off the sea floor when I couldn't get there. I cannot possibly sufficiently express my gratitude to my dearest friends and long-time co-workers Jamie Gove, Danny Merritt, Molly Timmers, Oliver Vetter, Jubilee-Felsing Watkins, and Chip Young, suffice to say they were all formative to me.

The inspiration for this course of study came largely from discussions with my dear friend Jerome Aucan, which occurred on Jen Homcy's front lanai in little Haleiwa town. Many of the ideas presented in this thesis have their root in these (sometimes late-night) discussions and any acknowledgments would be remiss without mentioning them. Sean Vitousek, Mark Merrifield, and others at the

University of Hawaii's School of Ocean and Earth Science and Technology also provided insight, support and assistance along the way.

I must also thank my mother and father, Rainer and Marcia Hoeke for their love and continued support, despite my now more than ten years of tertiary education. Gayle Kim Philip also has been patient throughout the more stressful periods of my PhD candidature. For that, and for her adventurous, funny and kind companionship, I will always thank her.

And lastly, but certainly not least, I must thank my grandfather, Ronald L. Cooksey, who helped open my eyes to the natural world and instilled a keen interest to try to discover how it all works. He would be proud.

Abstract

The coastal zone is of great societal and economic value. Understanding anthropogenic impacts and natural processes is a prerequisite to effective management of coastal resources, and a key part of this understanding is the prediction (both past and future) of the coastal zone's hydrodynamics. Methods of predicting the hydrodynamics of coral reef systems, which tend to be morphologically complex and subject to a variety of oscillatory and non-oscillatory motions over a large range of space and time scales, remain poorly developed.

Recent advances in numerical modeling have allowed the practical solution of the two- and three-dimensional shallow water Navier-Stokes equations at spatial scales on the order of tens of meters. This has allowed unprecedented prediction of coastal hydrodynamics, and its use is expanding, particularly in mid- to high latitude continental margins regions. Few researches have yet applied these advances to coral reef systems, however.

The goal of this work is to improve the understanding and prediction of relevant hydrodynamic processes in coral reef systems. This is accomplished by the combined analysis of in situ oceanographic instrument data and climate information, as well as the application of a coupled wave-flow numerical model at two different study sites. The study sites, Hanalei Bay and Midway Atoll, both in the Hawaiian Islands (Figure 1.1), constitute two fundamentally different reef morphologies, a fringing reef embayment and an atoll, respectively. Both are subjected to a wide range of wind-wave energy, which is shown to force the most energetic hydraulic motions at both sites.

Results include an evaluation of the numerical models used, a statistical analysis of wind-wave climate that identifies major modes of coastal circulation, and the calculation of flushing times and other coastal hydrodynamic metrics under different conditions. Model evaluation shows that if the spatially varying hydraulic roughness and wave dissipation approximations presented here are used, coupled wave/flow numerical model skill for steep and morphologically complex coral reefs may approach that of milder sloped mid-latitude continental margin coasts. The results also highlight important hydrodynamic differences between prevailing (wind and wave) conditions and episodic storm wave events. These events incur water

levels, current velocities, flushing rates, and inferred sediment transport several orders of magnitude greater than those of prevalent conditions. For instance, flushing (residence) times at both study sites are on the order of 1-3 days during prevalent conditions, whilst during large storm wave events flushing time may reduce to several hours. The high near-bed flows and associated shear stresses episodically mobilize and transport seafloor sediment and heavily impact the benthic biological community.

The number and magnitude of these episodic events are shown to exhibit high interannual variability linked to climate indices for El Niño/Southern Oscillation (ENSO) and the North Pacific Index (NPI). The historically small (but variable) number of these events (between 0 and approximately 20) indicate that annual differences in net sedimentation and water quality are very large at both sites, and most likely sensitive to long-term changes in annual recurrence. Additionally, large changes in sea level anomaly during these large wave events, evident in model predictions and confirmed by tide gauge data at Midway Atoll, introduce an unaccounted for variable in contemporary sea-level trend analyses, possibly at many *in situ* sea level monitoring sites in the Pacific and Indian Oceans.

Publications produced during the PhD Candidature

Peer-Reviewed:

Rooney, J., Wessel, P., **Hoeke, R. K**., Weiss, J., Baker, J., Parrish, F., Fletcher, C., Chojnacki, J., Garcia, M. O., and Vroom, P. (2008). "Geology and geomorphology of coral reefs of the Northwestern Hawaiian Islands", in B. Riegl and R. Dodge, [eds.], *Coral Reefs of the USA*. Berlin: Springer.

Hoeke, R. K., Gove, J. M., Smith, E., Wong, K. B., Brainard, R. E., Fisher-Pool, P., Lammers, M., Merritt, D., Vetter, O. J., and Young, C. W. (2009). "Coral reef ecosystem integrated observing system: In-situ oceanographic observations at the US Pacific islands and atolls." *Journal of Operational Oceanography*, 2, 3-14.

Hoeke, R. K., Storlazzi, C. D., and Ridd, P. V. (in press). "Hydrodynamics of a fringing coral reef embayment: Wave climate, wave field evolution, and episodic circulation." *Journal of Geophysical Research*.

Hoeke, R. K., Jokiel, P. L., and Buddemeier, R. W. (in press). "Projected growth and mortality of Hawaiian Corals over the next 100 years." *PLoS One.*

Hoeke, R. K., Storlazzi, C. D., and Ridd, P. V. (in internal review). "Hydrodynamics of a fringing coral reef embayment: flow fields, flushing times, and implications for water quality and sediment transport."

Hoeke, R. K., Aucan, J., and Merrifield, M. (submitted Feb 2011). "Sea-level Rise, Flooding, Flushing, and Wave Heights at a Coral Atoll." *Journal of Geophysical Research*.

Reports:

Hoeke, R. K., and Storlazzi, C. D. (2007). Hydrodynamic modeling of Hanalei Bay, p. 41-44. In M. E. Field, C. J. Berg and S. A. Cochran [eds.], Science and management in the Hanalei watershed; a trans-disciplinary approach: Proceedings from the Hanalei watershed workshop, 21-22 February 2007, U.S. Geological Survey Open File Report 2007-1219.

Hoeke, R.K. (2009). NOAA Ship Hi`ialakai. Cruise Report No. CRHI0901, National Oceanic and Atmospheric Administration (NOAA) Pacific Islands Fisheries Science Center Honolulu, Hawai'i.

Brainard R.E., Bainbridge S., Brinkman R., Eakin C.M., Field M., Gattuso J.P., Gledhill D., Gramer L., Hendee J., **Hoeke R.K.**, Holbrook S., Hoegh-Guldberg O., Lammers M., Manzello D., McManus M., Moffitt R., Monaco M., Morgan J., Obura D., Planes S., Schmitt R., Steinberg C., Sweatman H., Vetter O., Wong K. (2009). "An International Network of Coral Reef Ecosystem Observing Systems (I-CREOS)". *OceanObs Community White Paper*, Venice 2009.

Presentations:

Hoeke, R. K., and Storlazzi, C. D., (2007). "Predicting wave conditions in a coral embayment from offshore directional spectral model input", *Presented at the 10th International Workshop on Wave Hindcasting and Forecasting*. Turtle Bay, Hawaii.

Hoeke, R. K. (2007). "Overview of the Coral reef ecosystem integrated observing system of the U.S. flagged Pacific Islands." *Presented at the Workshop for Coral Reef Managers: Responding to Mass Coral Bleaching and Climate Change*, Lady Elliot Island, Queensland, Australia.

Hoeke, R. K., and Aucan, J. (2008). "Sea-Level Rise, Flooding, Flushing and Wave Heights at a Coral Atoll." *Presented at the AGU/ASLO/TOS Ocean Sciences 2008 Meeting*, Orlando, FL.

Hoeke, R. K., and Storlazzi, C. D. (2008). "Hydrodynamic modeling of a fringing reef embayment; Hanalei Bay, Hawaii." *Presented at 11th International Coral Reef Symposium*, Ft. Lauderdale, FL.

Hoeke, R. K., Jokiel, P. L., and Buddemeier, R. W. (2009). "Modeled Changes in Coral Growth and Mortality Over the Next 100 Years in the Hawaiian Archipelago." *Presented at 17th Hawai'i Conservation Conference*, Honolulu, Hawaii, USA.

Hoeke, R. K., Storlazzi, C. D., and Ridd, P. V. (2010). "The importance of episodic circulation to sedimentation patterns and distribution of benthic habitats in a fringing coral reef embayment." *Presented at the AGU/ASLO/TOS Ocean Sciences 2010 Meeting*, Portland, Oregon.

Contents

List of Figures

List of Tables

1. Introduction

Hydrodynamics control or strongly influence many ecological aspects of coral reefs, such as water quality, patterns of sedimentation, nutrient uptake, dispersal and recruitment of larvae, patterns of coral bleaching, and the degree of disturbance due to episodic storms [e.g. Dollar 1982; Hamner and Wolanski 1988; Andrews and Pickard 1990; Dollar and Tribble 1993; Hearn et al. 2001; Fabricius 2005; Madin and Connolly 2006]. Reef ecosystem health is of high value to human coastal communities in the tropics and sub-tropics [Moberg and Folke 1999; Moberg and Rönnbäck 2003]; furthermore, hydrodynamic processes often directly impact these coastal communities by driving coastal erosion, episodic inundation (coastal flooding) and the advection and dispersion of pollutants and other toxins [e.g. Gourbesville and Thomassin 2000; Paul et al. 2000; Yamano et al. 2007; Woodroffe 2008]. Thus, a thorough understanding of coral reef hydrodynamics is a necessary prerequisite for effective coastal management. This necessity is made more acute by human's increasing impact on the coastal zone in a period of rapid climate change [Lotze et al. 2006; Hoegh-Guldberg and Bruno 2010].

In this thesis, a detailed analysis is presented that furthers the state of knowledge of reef hydrodynamics by focusing on surface gravity (wind generated) waves and wave driven flows. The fundamental importance of surface gravity waves to reef hydrodynamics was identified fairly early [Munk and Sargent 1948; Von Arx 1948], and more recent studies have highlighted their dominant contribution for many different reef morphologies [e.g. Callaghan et al. 2006; Coronado et al. 2007; Monismith 2007; Hench et al. 2008]. Additionally, distribution of wave-generated bed shear stresses, resulting from the dissipation of wave energy, have been shown to be the pivotal factor in determining benthic community composition, particularly in wave-dominated areas [e.g. Dollar 1982; Dollar and Tribble 1993; Roger 1993; Grigg 1998; Fulton and Bellwood 2005; Storlazzi et al. 2005]. While the mean increase in water elevation (set-up) and associated barotropic mean flows resulting from this dissipation (or radiation stress gradient, see Longuet-Higgins and Stewart 1964; Tait 1972; Monismith 2007 for physical description) are conceptually easy to understand, parameterization and prediction of these processes over steep, rough, and morphologically complex coral reefs have proven problematic [Hearn 1999; Gourlay and Colleter 2005; Lowe et al. 2009].

The past decade has seen the development of a number of high resolution, iteratively coupled two- and three-dimensional (2D, 3D) wave-circulation numerical models. These models have a number of distinct advantages over the simplified one-dimensional (1D) analytical models often used to describe wave transformation and flow over coral reefs [Symonds et al. 1995; Hearn 1999; Gourlay and Colleter 2005]. First, real wave driven flows on morphologically complex coral reefs are inherently 2D [Lowe et al. 2009]. Second, while wave driven flows may dominate over most or part of the reef system, circulation of most reef systems is driven by a combination of forcing mechanisms (e.g. also by winds, tides, and buoyancy), and the importance of these mechanisms may vary spatially and temporally. The complex interactions between these different forcing mechanisms can only be fully explored through the use of these 2D and 3D numerical models [Lowe et al. 2009].

Prager [1991] was one of the first researchers to publish the results of a 2D numerical circulation model of a coral reef which included wave radiation stress forcing. While the model was able to qualitatively reproduce observed circulation patterns, highlighting the potentially high value of numerical models to describe coral reefs processes, the radiation stress calculation was extremely simplified and input wind and waves were not varied in time according to actual conditions, making rigorous validation impossible. Kraines et al. [1998] and Kraines et al. [1999] greatly improved radiation stress input to coral reef circulation models by directly spatially and temporally modeling wave breaking. These models suffer from a number of drawbacks, however, such as not including wave dissipation due to bottom friction (which may be a very large contribution [Lowe et al. 2005]), and coarse spatial resolution (e.g. 500 m grid cells), which is shown to be insufficient to reproduce important flow structures in this thesis (e.g. Figure 2.9). Perhaps the greatest drawback of these earlier coral reef models is that they are not truly coupled, i.e. estimates of wave dissipation are used to force circulation, but estimated circulation is not used to estimate wave dissipation. This means that complex interactions, such as combined wave-current boundary layers and resulting (enhanced) bed shear, cannot be investigated, and circulation patterns, especially at smaller scales, are more likely to be poorly estimated.

A newer generation high resolution coupled models, in which wave and circulation modules iteratively pass information back and forth, have been widely applied and validated on low-slope sedimentary coastlines [e.g. the North Sea coast of Holland and the U.S. East Coast Lesser et al. 2004; Warner et al. 2008]. However, they have been applied far less frequently on steeper erosional coasts Mulligan et al. 2008; and thus far only a handful of studies (including this one) have tested them on the still steeper, more complex coral reef systems [Vitousek et al. 2007; Lowe et al. 2009].

In an effort to better resolve and predict reef system hydrodynamics, we employ a combination of both long-term historical and short-term *in situ* oceanographic observations and a new generation coupled wave-flow numerical model at two different sites. The study sites, Hanalei Bay on the island of Kauai and Midway Atoll, both in the Hawaiian Archipelago (Figure 1.1), are highly representative of two of the three most common distinct coral reef morphologies: a fringing reef embayment on the coast of a volcanic high island and a low-lying coral atoll [Stoddart 1969]. Both locations are exposed to a wide variety of wind and swell conditions, including annual episodic wave heights in excess of 5 meters. Given the previously discussed of importance of episodic conditions, special attention is given to the episodic (storm) wave events occurring during the study periods at both sites. This is a significant departure from previous studies of coral reefs utilizing the new generation of coupled models, which cover only “normal” or “modal” conditions, [e.g. Lowe et al. 2009].

1.1 Thesis Layout

The following three chapters are divided into papers that have either been published (Chapter 2, [Hoeke et al. 2011]), submitted (Chapter 4), or are in the process of being submitted to peer-reviewed journals (Chapter 3). The first paper (Chapter 2) develops a wind-wave climatology for the Hawaiian archipelago from historical buoy observations and numerical hindcasts. The climatology is used to statistically characterize the hydrodynamic regimes observed by an 10-month record of in situ instrument data at Hanalei Bay. The paper goes on to evaluate and parameterize a numerical wave model required to calculate the propagation of waves over the bay’s complex bathymetry; these results provide insight into the hydrodynamic regimes observed.

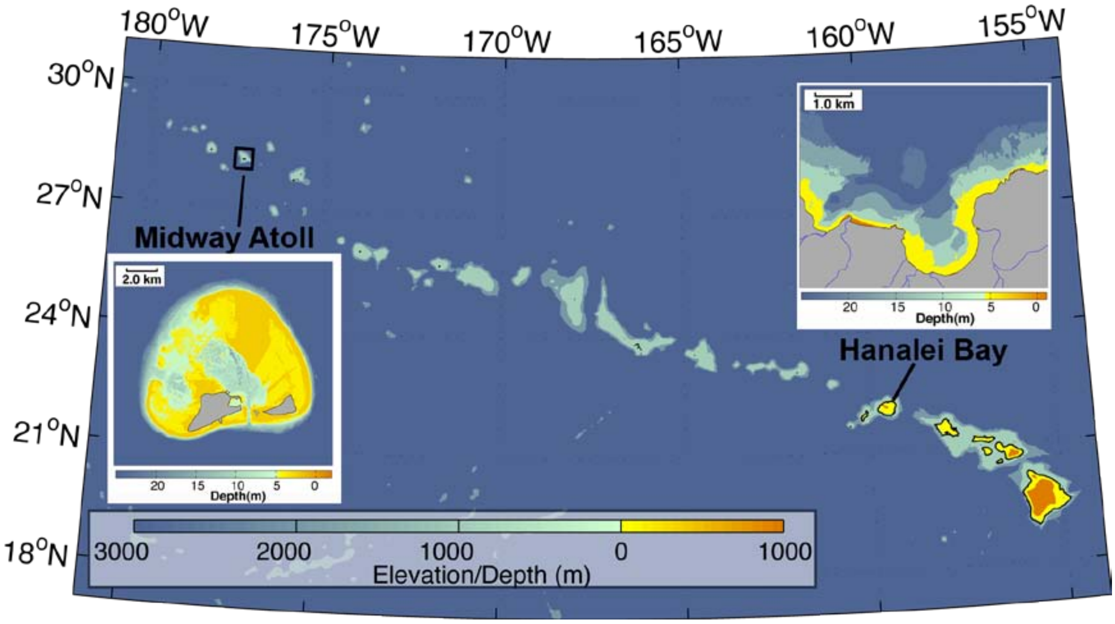

Figure 1.1 - Map of the Hawaiian Archipelago. The two study areas, Hanalei Bay (on the north coast of Kauai island) and Midway Atoll, are shown in the insets.

The second paper (Chapter 3) evaluates and parameterizes a coupled wave-flow numerical wave model for Hanalei Bay (on the island of Kauai) with special attention to the dissipation of wave energy and subsequent barotropic currents. The model is used to calculate overall circulation, mean flushing (residence) time, and spatial pattern of benthic shear stress under different wave conditions/hydrodynamic regimes, as well as the relative contribution of different forcing mechanisms (i.e. wind, tide, wave, and buoyancy). The implication of these results for water quality, sedimentation processes and ecosystem dynamics are examined in relation to climate variability, especially the Multi-variate El Niño/Southern Oscillation (ENSO) index [MEI: Wolter and Timlin 1998]. In particular the importance and decoupled nature of episodic sediment delivery from the steep-sided water shed to the bay and is removal by storm waves is identified.

The third paper (Chapter 4) presents an analysis of sea level anomaly (SLA), based on an approximately 60-year record of tidal heights measured in the lagoon of Midway Atoll. It is shown that SLA variability is highly dependent on the seasonal variations in wave climate described in paper one. The process of wave-driven SLA is examined through the application of the wave-flow coupled model developed in paper 2 to Midway Atoll. The model was able to predict SLA within the atoll to within less than a 30% margin of error, and provided insight into episodic storm waves driving large SLA events, which have the potential to inundate low-lying atoll islands as well as the (episodic) transport of sediment and other materials, into, out of, and within the atoll. The frequency and magnitude of these episodic storm wave events exhibits co-variance with the MEI and in particular the North Pacific Index [Trenberth and Hurrell 1994]. This wave-driven variability in the SLA events introduces a large and currently unaccounted for uncertainty in contemporary sea-level analyses of tide gauges e.g. [Firing et al. 2004; Church et al. 2006; Woodworth et al. 2009].

1.2 References

Andrews, J. C., and G. L. Pickard. 1990. The physical oceanography of coral-reef systems, p. 11-48. *In* Z. Dubinsky [ed.], Coral reefs. Elsevier.

Callaghan, D. P., P. Nielsen, N. Cartwright, M. R. Gourlay, and T. E. Baldock. 2006. Atoll lagoon flushing forced by waves. Coastal Engineering **53:** 691-704.

Church, J. A., N. J. White, and J. R. Hunter. 2006. Sea-level rise at tropical Pacific and Indian Ocean islands. Global and Planetary Change **53:** 155-168.

Coronado, C., J. Candela, R. Iglesias-Prieto, J. Sheinbaum, M. López, and F. J. Ocampo-Torres. 2007. On the circulation in the Puerto Morelos fringing reef lagoon. Coral Reefs **26:** 149-163.

Dollar, S. J. 1982. Wave stress and coral community structure in Hawaii. Coral Reefs **1:** 71-81.

Dollar, S. J., and G. W. Tribble. 1993. Recurrent storm disturbance and recovery: a long-term study of coral communities in Hawaii. Coral Reefs **12:** 223-233.

Fabricius, K. E. 2005. Effects of terrestrial runoff on the ecology of corals and coral reefs: review and synthesis. Mar. Pollut. Bull. **50:** 125-146.

Firing, Y. L., M. A. Merrifield, T. A. Schroeder, and B. Qiu. 2004. Interdecadal Sea Level Fluctuations at Hawaii. Journal of Physical Oceanography **34:** 2514-2524.

Fulton, C. J., and D. R. Bellwood. 2005. Wave-induced water motion and the functional implications for coral reef fish assemblages. Limnol. Oceanogr. **50:** 255-264.

Gourbesville, P., and B. A. Thomassin. 2000. Coastal environment assessment procedure for sustainable wastewater management in tropical islands: the Mayotte example. Ocean & Coastal Management **43:** 997-1014.

Gourlay, M. R., and G. Colleter. 2005. Wave-generated flow on coral reefs--an analysis for two-dimensional horizontal reef-tops with steep faces. Coastal Engineering **52:** 353-387.

Grigg, R. W. 1998. Holocene coral reef accretion in Hawaii: a function of wave exposure and sea level history. Coral Reefs **17:** 263-272.

Hamner, W. M., and E. Wolanski. 1988. Hydrodynamic forcing functions and biological processes on coral reefs: a status review. Proc 6th Int Coral Reef Symp **1**.

Hearn, C., M. Atkinson, and J. Falter. 2001. A physical derivation of nutrient-uptake rates in coral reefs: effects of roughness and waves. Coral Reefs **20:** 347-356.

Hearn, C. J. 1999. Wave-breaking hydrodynamics within coral reef systems and the effect of changing relative sea level. J. Geophys. Res. **104:** 30,007–030,019.

Hench, J. L., J. J. Leichter, and S. G. Monismith. 2008. Episodic circulation and exchange in a wave-driven coral reef and lagoon system. Limnol. Oceanogr **53:** 2681-2694.

Hoegh-Guldberg, O., and J. F. Bruno. 2010. The Impact of Climate Change on the World's Marine Ecosystems. Science **328:** 1523-1528.

Hoeke, R. K., Storlazzi, C. D., and Ridd, P. V. (in press). "Hydrodynamics of a fringing coral reef embayment: Wave climate, wave field evolution, and episodic circulation. J. Geophys. Res.

Kraines, S., T. Yanagi, M. Isobe, and H. Komiyama. 1998. Wind-wave driven circulation on the coral reef at Bora Bay, Miyako Island. Coral Reefs **17:** 133-143.

Kraines, S. B., A. Suzuki, T. Yanagi, M. Isobe, X. Guo, and H. Komiyama. 1999. Rapid water exchange between the lagoon and the open ocean at Majuro Atoll due to wind, waves, and tide. J. Geophys. Res. **104:** 15635-15653.

Lesser, G. R., J. A. Roelvink, J. A. T. M. Van Kester, and G. S. Stelling. 2004. Development and validation of a three-dimensional morphological model. Coastal Engineering **51:** 883-915.

Longuet-Higgins, M. S., and R. W. Stewart. 1964. Radiation stresses in water waves; a physical discussion, with applications. Deep Sea Research **11:** 529-562.

Lotze, H. K. and others 2006. Depletion, Degradation, and Recovery Potential of Estuaries and Coastal Seas. Science **312:** 1806-1809.

Lowe, R. J. and others 2005. Spectral wave dissipation over a barrier reef. J. Geophys. Res. **110:** 16.

Lowe, R. J., J. L. Falter, S. G. Monismith, and M. J. Atkinson. 2009. A numerical study of circulation in a coastal reef-lagoon system. J. Geophys. Res. **114:** C06022.

Madin, J. S., and S. R. Connolly. 2006. Ecological consequences of major hydrodynamic disturbances on coral reefs. Nature **444:** 477-480.

Moberg, F., and C. Folke. 1999. Ecological goods and services of coral reef ecosystems. Ecological Economics **29:** 215-233.

Moberg, F., and P. Rönnbäck. 2003. Ecosystem services of the tropical seascape: interactions, substitutions and restoration. Ocean & Coastal Management **46:** 27-46.

Monismith, S. G. 2007. Hydrodynamics of Coral Reefs. Annu. Rev. Fluid Mech. **39:** 37-55.

Mulligan, R. P., A. E. Hay, and A. J. Bowen. 2008. Wave-driven circulation in a coastal bay during the landfall of a hurricane. J. Geophys. Res. **113:** C05026.

Munk, W., and M. Sargent. 1948. Adjustment of Bikini Atoll to waves. Transactions, Am. Geo. Union **29:** 855-860.

Paul, J., M. Mclaughlin, D. Griffin, E. Lipp, R. Stokes, and J. Rose. 2000. Rapid movement of wastewater from on-site disposal systems into surface waters in the Lower Florida Keys. Estuaries and Coasts **23:** 662-668.

Prager, E. 1991. Numerical simulation of circulation in a Caribbean-type backreef lagoon. Coral Reefs **10:** 177-182.

Roger, C. S. 1993. Hurricanes and coral reefs: the intermediate disturbance hypothesis revisited. Coral Reefs **12:** 127-138.

Stoddart, D. R. 1969. Ecology and morphology of recent coral reefs. Biological Reviews **44:** 433-498.

Storlazzi, C. D., E. K. Brown, M. E. Field, K. Rodgers, and P. L. Jokiel. 2005. A model for wave control on coral breakage and species distribution in the Hawaiian Islands. Coral Reefs **24:** 43-55.

Symonds, G., K. P. Black, and I. R. Young. 1995. Wave-driven flow over shallow reefs. J. Geophys. Res. **100:** 2639–2648.

Tait, R. J. 1972. Wave Set-Up on Coral Reefs. J. Geophys. Res. **77:** 2207-2211.

Trenberth, K. E., and J. W. Hurrell. 1994. Decadal Atmosphere-Ocean Variations in the Pacifc. Climate Dynamics **9:** 303-319.

Vitousek, S., C. H. Fletcher, M. A. Merrifield, G. Pawlak, and C. D. Storlazzi. 2007. Model Scenerios of Shoreline Change at Kaanapali Beach, Maui, Hawaii: Seasonal and Extreme Events, p. 95-95. ASCE.

Von Arx, W. S. 1948. The circulation systems of Bikini and Rongelap lagoons. Eos Trans. AGU **29:** 861-870.

Warner, J. C., C. R. Sherwood, R. P. Signell, C. K. Harris, and H. G. Arango. 2008. Development of a three-dimensional, regional, coupled wave, current, and sediment-transport model. Computers & Geosciences **34:** 1284-1306.

Wolter, K., and M. S. Timlin. 1998. Measuring the strength of ENSO events - how does 1997/98 rank? Weather**:** 315-324.

Woodroffe, C. D. 2008. Reef-island topography and the vulnerability of atolls to sea-level rise. Global and Planetary Change **62:** 77-96.

Woodworth, P. L., N. J. White, S. Jevrejeva, S. J. Holgate, J. A. Church, and W. R. Gehrels. 2009. Evidence for the accelerations of sea level on multi-decade and century timescales. International Journal of Climatology **29:** 777-789.

Yamano, H. and others 2007. Atoll island vulnerability to flooding and inundation revealed by historical reconstruction: Fongafale Islet, Funafuti Atoll, Tuvalu. Global and Planetary Change **57:** 407-416.

2. Hydrodynamics of a bathymetrically complex fringing coral reef embayment: wave climate, in situ observations and wave prediction

Ron Hoeke[1,2], Curt Storlazzi[3], and Peter Ridd[2]

1. Joint Institute for Marine and Atmospheric Research (JIMAR)

   University of Hawaii and NOAA Pacific Islands Fisheries Science Center

   Honolulu, Hawaii, USA

2. School of Engineering and Physical Sciences

   James Cook University

   Townsville, Queensland, Australia

3. Coastal and Marine Geology Program

   US Geological Survey

   Santa Cruz, California, USA

Abstract

This paper examines the relationship between offshore wave climate and nearshore waves and currents at Hanalei Bay, Hawaii, an exposed bay fringed with coral reefs. Analysis of both offshore *in situ* data and numerical hindcasts identify the predominance of two wave conditions: a mode associated with local trade winds and an episodic pattern associated with distant-source long period swells. Analysis of 10 months of *in situ* data within the bay show that current velocities are up to an order of magnitude greater during long-period swell episodes than during trade wind conditions; overall circulation patterns are also fundamentally different. The current velocities are highly correlated with incident wave heights during the swell episodes; they are not during the modal trade-wind conditions. A phase-averaged wave model was implemented with the dual purpose of evaluating application to bathymetrically complex fringing reefs and to examine the propagation of waves into the nearshore, in an effort to better explain the large difference in observed circulation during the two

offshore wave conditions. The prediction quality of this model was poorer for the episodic condition than for the lower energy mode, however it illustrated how longer-period swells are preferentially refracted into the bay and make available far more nearshore wave energy to drive currents compared to waves during modal conditions.

The highly episodic circulation, the nature of which is dependent on complex refraction patterns of episodic, long-period swell, has implications for flushing and sediment dynamics for incised fringing reef-lined bays that characterize many high islands at low latitudes around the world.

2.1 Introduction

Hydrodynamic forcing of reef systems controls or strongly influences many ecological aspects of the reef, such as patterns of sedimentation and pollutants, nutrient uptake, dispersal and recruitment of larvae, patterns of coral bleaching, and degree of disturbance due to episodic storms [Hamner and Wolanski, 1988; Andrews and Pickard, 1990; Hearn, 1999; Madin and Connolly, 2006]. The importance of surface gravity waves to reef hydrodynamics was identified fairly early [Munk and Sargent, 1948; von Arx, 1948], and more recent studies have highlighted their dominant contribution for many different reef morphologies [e.g. Callaghan et al., 2006; Coronado et al., 2007; Hench et al., 2008; Monismith, 2007]. Additionally, distribution of wave-generated, bed shear stresses have been shown to be the pivotal factor in determining benthic community composition, particularly in wave-dominated areas [e.g., Dollar, 1982; Roger, 1993; Grigg, 1998; Fulton and Bellwood, 2005; Storlazzi et al., 2005]. While the mean increase in water elevation (set-up) and associated barotropic mean flows resulting from the dissipation of wave energy (radiation stress gradient Longuet-Higgins and Stewart, 1964; Tait, 1972; Monismith, 2007) is conceptually easy to understand, its parameterization and prediction over steep and morphologically complex coral reefs have proven problematic [Hearn, 1999; Gourlay and Colleter, 2005].

Here, we examine the wave-dependence of circulation in a semi-enclosed bay bordered by fringing reefs through (1) the quantification of wave climate and (2) an examination of circulation as indicated by 10-month period of *in situ* wave and current data. We then go on to (3) implement and validate a numerical wave model to examine the nearshore wave field. The prediction and validation of the wave field within the bay is a prerequisite to accomplishing numerical circulation modeling efforts within the bay, which will be presented in Chapter 3.

The study site, Hanalei Bay on the Hawaiian Island of Kauai (Figure 2.1), receives a high episodic sediment load from its steep-sided watersheds, and episodic wave events have been identified as important to the distribution, (re)suspension, and transport of these sediments [Calhoun et al., 2002; Draut et al., 2009; Storlazzi et al., 2009]. Such sedimentation has the potential to significantly impact reef ecosystems [Fabricius, 2005] and has been implicated in the major ecological degradation of a number of qualitatively similar fringing reef/watershed systems [Wolanski et al., 2003]. This makes understanding flushing mechanisms imperative for good governance of the bay’s ecological resources.

2.2 Methods

2.2.1 Study Area Description

Kauai (22.2°N, 159.5°W) is a subtropical high island of volcanic origin lying in the North Pacific trade wind belt. Tides in the area are mixed semidiurnal with neap ranges of around 0.4 m and spring ranges around 0.9 m [Storlazzi et al., 2009]. Trade wind conditions associated with the North Pacific subtropical anticyclone prevail; these winds are typically around 5–12 $m \cdot s^{-1}$ and generate wind waves generally 1–3 m in height with 6-10 s periods from the east to northeast [Moberly and Chamberlain, 1964]. Trade winds occur throughout the year, but are most prevalent during the spring and summer months. Hanalei Bay, approximately 2 km wide, is located on the island’s north side and faces roughly north-northwest (Figure 2.1b). This makes it partially sheltered from trade wind conditions, but exposed to seasonally high episodic swell events between October and May. These swells are usually generated from remote sources to the north and west (NW), with 1–5 m waves and 12–20 s periods common during these months; wave heights in excess of 6 m may occur several times a year. During these swell events, winds typically slacken or become westerly and rotate clockwise back to the northeast, as cyclonic low pressure systems producing the swell pass to the north, although this is not always the case. Tropical and extra-tropical cyclones (the latter known as ‘Kona’ storms) also occasionally impact the island; however, these mostly affect the south and west sides of the island.

Fringing reef platforms are found on the east and west sides of the bay; the western reef (‘Queen’s Reef’) generally has a more gradual reef slope (~ 6–12°) and deeper reef flat (~ 1–4 m), while the eastern side (‘Hanalei Reef’) is somewhat steeper (reef slope of 10° to nearly vertical) and has an extensive area of reef flat less then 1 m deep. A detached deeper reef (‘King’s Reef’) lies approximately 1 km offshore and has a minimum depth of ~16 m. This offshore reef affects incident-gravity wave refraction patterns and has been known to break when waves exceed 5 m. These reefs are composed primarily of coralline alga, with live coral cover ranging between 2% and 47%, with an average of about 18% [Friedlander and Brown, 2005]. Most other areas in the bay tend to be made up of flat or gently sloping sand or gravel, and are mostly carbonate in composition, especially at shallower depths [Calhoun et al., 2002]. A notable exception is the ‘Black Hole’, a 2–5 m deep depression at a depth of 12–15 m west and south of the mouth of the Hanalei River, where terrestrial material (siliciclastic and organic) comprises a large fraction of the sediment [Calhoun et al., 2002; Draut et al., 2009; Storlazzi et al., 2009]; it appears that terrestrial materials are also often deposited in other areas of the bay during river floods and subsequently resuspended and advected during later wave events [Draut et al., 2009].

Hanalei and the surrounding coasts are backed by Mount Wai’ale’ale (elevation 1570 m) and it is often identified as the ‘wettest place on earth’ with yearly rainfall totals at a rain gauge on the slopes averaging between 9 and 10 m [Calhoun and Fletcher, 1999; Polyakov et al., 2007]. The Hanalei river delivers an estimated annual fluvial sediment load of 1.76×10^4 Mg, the highest of such estimates for a single watershed in the Hawaiian Islands [Calhoun and Fletcher, 1999].

The Hanalei watershed is one of the three priority watersheds in Hawaii identified for focused action to address land-based pollution threats to coral reefs by the U.S. Coral Reef Task Force. These and other environmental concerns have prompted a number of studies in the area [e.g. Friedlander and Parrish, 1997; Calhoun et al., 2002; Friedlander and Brown, 2005; more recent studies are summarized by Field et al., 2007].

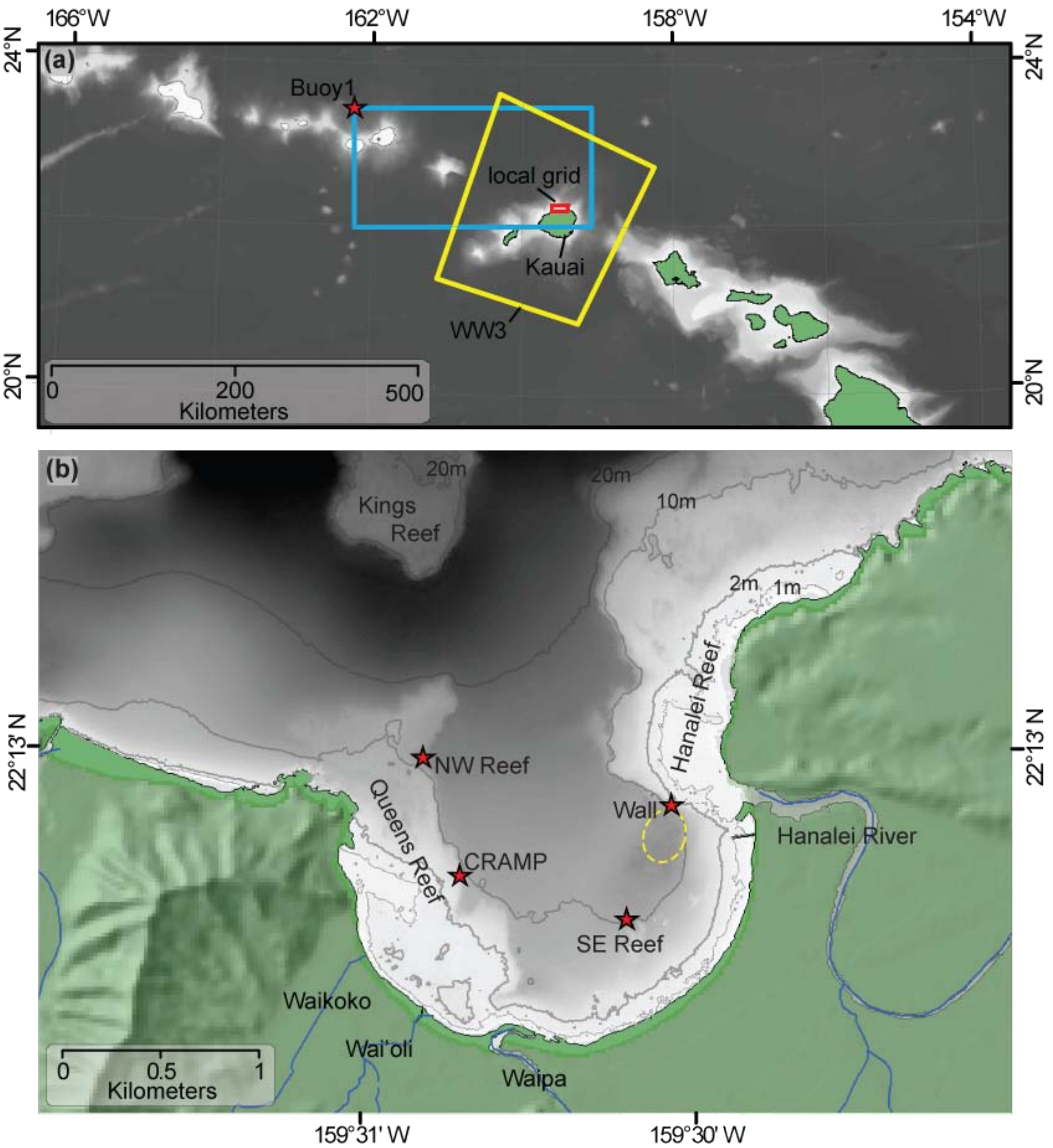

Figure 2.2: Study site location maps: (a) Hawaiian Archipelago with the position of NOAA NDBC Buoy 51001 (Buoy 1) indicated by a star at the northwest corner of the Buoy 1 input grid boundaries (blue); the WW3 input grid boundaries surround the island of Kauai (yellow); the local model grid boundaries are centered on Hanalei Bay, on the north coast of Kauai (red). (b) Hanalei Bay with Wall, SE Reef, CRAMP, and NW Reef mooring site positions and bathymetric contours indicated; the mouth of Hanalei River is on the east side of the bay and the Waipa, Wai'ole, and Waikoko streams are indicated. The 'Black Hole', outlined with a dotted yellow line, is just south of the Wall Site.

2.2.2 Determination of Wave Climate

The National Oceanographic and Atmospheric Administration's (NOAA) National Data Buoy Center (NDBC) Buoy 51001, 314 km northwest of Kauai in 3430 m of water (Figure 2.1a), was first deployed in 1981 as a non-directional wave and meteorology buoy, providing measurements of wave height and period, wind speed and direction, sea-level barometric pressure, and sea-surface water and air temperature (http://www.ndbc.noaa.gov). In 2005, it was upgraded to include directional wave measuring capacity. This buoy will be referred to as Buoy 1 for the remainder of the document. While it is located some distance from the study site (~ 300 km), the buoy measurements can be considered representative of trade wind wave and NW swell contributions to wave climate immediately offshore from the study site (modeling results presented here suggest this to be the case). Mean Wave height climatologies were constructed by calculating the mean, standard deviation, and minimum and maximum for each month for all available observations of significant wave height (H_s) between 1981 and 2009. Directional wave climatologies were constructed by discretizing all available bulk wave parameters of H_s into 2 s peak period (T_p) by 5° peak wave direction (θ_p) bins between years 2005 and 2009. These binned values were then analyzed for (1) mean bin event frequency of occurrence, and (2) mean significant wave height for each bin. This allows for an examination of how often (in a year or season) a particular wave direction/frequency event tends to occur and its average magnitude (height). The maximum entropy method [Lygre and Krogstad, 1986] was used to calculate directional wave energy spectra ($E_{(\sigma,\theta)}$) from Buoy 1 pitch and roll data. Conditions were classified as "trade wind" or "NW swell" when wave energy (E), defined as:

$$E = \int_{\sigma=j}^{\sigma=k} \int_{\theta=m}^{\theta=n} E_{(\sigma,\theta)} d\sigma d\theta \qquad [1]$$

integrated over frequency (σ) and directional (θ) sectors fell into a range of values associated with the respective conditions, as defined by the directional climatologies (see results for definition of these σ, θ, and E values). Additionally, the Buoy 1 directional spectra were used as input to the numerical wave models, as discussed below.

Since the time period of available Buoy 1 directional wave data was considered somewhat too short to effectively characterize directional wave climate (4 years), climatologies were also constructed from National Environmental Predictions Center (NCEP) Wave Watch III Version 2.22 NE Pacific Model (0.25° spatial resolution) output (referred to as WW3 for the remainder of the document, see http://polar.ncep.noaa.gov/waves and Tolman [2002] an overview). WW3 bulk parameter hindcast data (H_s, T_p, and θ_p) are available from 1996 to 2009. The same methods used to compute Buoy 1 directional climatologies were applied to WW3 hindcast data from the same location as Buoy 1. Additionally WW3 hindcast bulk wave parameters, spectral data, and gridded wind fields were tested as input to a fine-scale coastal wave model, as discussed below.

2.2.3 Nearshore In-situ Data Collection

Physical measurements inside the bay were recorded at four bottom-mounted acoustic Doppler current profiler (ADCP) mooring sites between June 7, 2006 and April 7, 2007. Details of these instrument platforms are given in Table 2.1 and their locations are plotted in Figure 2.1b and 1c. The Wall site, proximate to the near-vertical rise of Hanalei Reef from the seabed at around 10 m of a depth to approximately 2 m in this area, was located near the mouth of the Hanalei River. The SE Reef site, proximate to a small reef outcropping, was located near the center of the bay. The CRAMP site (co-located with a University of Hawai'i coral reef monitoring program site, Jokiel et al., 2004) was located on the western side of the bay at the base of the Queen's Reef forereef; the NW Reef site is 600 m north along the base of Queen's Reef from the CRAMP site.

Table 2.1: Instruments deployed in or near Hanalei Bay for this study. Deployments depths (h) and deployment dates are given; for deployment locations, refer to Figure 2.1b.

Site	Instrument	h(m)	dates
Wall	RD Instruments ADCP (600 kHz)	10.0	Jun7, 2006 – Apr24, 2007
NW Reef	Sontek ADCP (1 MHz)	14.5	Sep14, 2006 – Apr24, 2007
CRAMP	Nortek ADCP (1 MHz)	9.7	Jun7, 2006 – Sep7, 2006
SC Reef	Nortek ADCP (1 MHz)	10.5	Jun7, 2006 – Sep7, 2006

Sampling strategies allowed for water velocity profile and mean sea surface (observed tide) to be measured at least every 30 minutes, and directional wave parameters at least once an hour during observation periods. A high frequency cut-off 0.25 Hz (T = 4 s) seconds was used for the pressure (PUV) based wave calculations (Nortek and Sotek/YSI instruments) to remove potential measurement errors in the high frequency part of the spectrum, i.e. the pressure response factor corrections (Dean and Dalrymple, 1995). This cut-off is lower (more conservative) than that suggested by the instrument manufacturers, even at the deepest mooring (14.5 m).

Neglecting these higher frequencies in wave calculations is not considered a significant source of error in this study. Measured wave energy in these higher frequencies at the Wall site, which used acoustic surface tracking to help characterize waves, was very low (<<5% of total); also peak frequencies measured at Buoy 1 (see description below) were < 0.2 Hz 99.9% of the time between years 2005 and 2009. Harmonic analysis [Pawlowicz et al., 2002] of pressure time series at the Wall and NW Reef sites (both) resulted in six astronomic tidal constituents (M2, S2, O1, K1, N2, and SK3) with signal-to-noise ratios greater than 10; these were used to predict tidal elevations during model runs.

2.2.4 Wave Model Implementation

The SWAN model (version 40.72AB), a phase-averaged solution of the discrete spectral balance of wave-action density [Booij et al., 1999], was selected to estimate wave fields within the bay. This approach conserves action density (*N*), defined as wave energy (*E*) divided by relative frequency (σ). The propagation of *N* in time (*t*), space (*x*,*y*), and frequency and direction (σ, θ) is described by:

$$\frac{\partial}{\partial t}N + \frac{\partial}{\partial x}c_x N + \frac{\partial}{\partial y}c_y N + \frac{\partial}{\partial \sigma}c_\sigma N + \frac{\partial}{\partial \theta}c_\theta N = \frac{S_{tot}}{\sigma} \qquad [2]$$

In the second and third terms, the velocities c_x and c_y are components of group speed; the third and fourth represent frequency shifting and refraction due to changes in current and depth, respectively; c_σ and c_θ describing the rates of change. The wave field propagation (left side) is balanced by the source terms (S_{tot}) on the right; the source terms are composed of:

$$S_{tot} = S_{in} + S_{wc} + S_{nl4} + S_{fr} + S_{br} + S_{nl3} \qquad [3]$$

These individual source terms are wind generation (S_{in}), dissipation (white capping S_{wc}, bottom friction S_{fr}, and breaking S_{br}), and nonlinear interactions (quadruplets S_{nl4} and triads S_{nl3}).

Due to the predominance of relatively large, mature seas in the area and the small spatial scale of the local model, surface wind processes were not considered significant to the processes of interest, and S_{in} and S_{wc} were not included in the local model. In the larger-scale models, however, wind growth (S_{in}) and whitecapping (S_{wc})

were included. For more information on model formulations and validation of SWAN see Booij et al. [1999] and Ris et al. [1999]; Mulligan et al. [2008a] and Mulligan et al. [2008b] provide a succinct overview, including some new developments not included in Booij et al. [1999].

2.2.4.1 Local model simulations

Two 1-week periods were selected for model development and validations: August 2-9, 2006 and January 20–27, 2007; the first characterized by trade wind conditions and the second NW swell, as described in Section 2.2.2. To estimate the wave field within Hanalei Bay and immediately offshore during these two periods, a rectangular Cartesian coordinate grid was constructed (local grid); this grid extends 8 km on either side of the bay and 5 km offshore of the mouth of the bay (Figure 2.1a). Simulations were carried out on the grid at ($\Delta x = \Delta y =$) 200, 100, and 40 m spatial resolutions; a subdomain, extending 2.5 km either side of the bay and 3.0 km offshore, was nested within the 40-m spatial resolution grid and simulations carried out at 30-, 20-, and 10-m resolutions.

Frequency space was resolved with 25 logarithmic bins from 0.04 to 0.40 Hz ($\Delta\sigma/\sigma = 0.1$). Directional resolution was varied from $\Delta\theta = 5^{o}$ to $\Delta\theta = 1^{o}$; implementations of refraction were tested; and simulations with and without phase-decoupled estimated diffraction [Holthuijsen et al., 2003] were conducted.

Model bathymetry was interpolated from two different sources: LiDAR data in shallower areas (provided by the US Army Corps of Engineers, http://shoals.sam.usace.army.mil/) and multibeam acoustics (provided by University of Hawai'i Benthic Habitat Mapping Center, http://www.soest.hawaii.edu/pibhmc/) in deeper areas. In almost all cases, bathymetric data resolution was far higher (on the order of 1 m for the LiDAR and 5 m for the multibeam) than computation grid cell resolution; grid bathymetric errors due to interpolation in data poor areas are considered insignificant.

The formulation of Madsen et al. [1988] was used to estimate bottom friction; wave hydraulic roughness length (k_w) scales were varied from 0.01 m to 0.20 m, the higher range of values (0.10-0.20 m) suggested for coral reefs [Hearn, 1999; Lowe et al., 2005]. Simulations with both spatially fixed and varied roughness values were carried out, with higher values for reef substrate (~ 0.10–0.20 m) than for unconsolidated sediment (sand, ~ 0.01 m). Areas of reef and sand were differentiated through a combination of bathymetric slope analysis and visual inspection of aerial photography, IKONOS, and Quickbird satellite imagery. Values for empirical wave breaking criteria [breaker height coefficient (γ_b) = 0.8, rate of dissipation coefficient (α) =1] were calculated according to Massel and Gourlay's [2000] paper for similar reef slopes. An analysis of model sensitivity to these coefficients is presented in Chapter 3. Water elevations predicted from the tidal constituents were varied uniformly over the model grid for all simulations.

2.2.4.2 Generation of wave boundary conditions

Unfortunately, the nearest measurements of deepwater waves available to drive the local wave model grid was a University of Hawai'i maintained directional wave rider buoy approximately 170 km away off the north coast of the island of Oahu. This buoy was not considered for input, as it is largely sheltered from typical trade wind waves by Oahu and may be partially sheltered by Kauai during NW swell events. As significant evolution of the wave field may occur in the intervening 300 km between the local grid and the other nearest deepwater wave measuring device, Buoy 1, an alternate source of wave forcing of the local grid was required.

Generation of input wave forcing was initially attempted by applying bulk wave parameters (H_s, T_p, θ_p) provided by WW3, and an estimated directional spreading (s_p) at the local model's offshore grid boundary. This was quickly abandoned, as it neglected multiple peaks in the real spectrum (often present in the Hawaiian Archipelago) and likely was generally a poor representation of real directional-frequency energy spectra under most conditions. This led to the evaluation of two directional spectral input methods, one based on WW3 and the other based on Buoy 1 data, necessitating the construction of two coarse resolution SWAN grids (Figure 2.1a).

The first grid was a 1 km spatial resolution curvilinear grid nested within WW3 spectral output nodes surrounding the island of Kauai (WW3 input model, Figure 2.1a); the second, a 2-km resolution orthogonal grid with the northwest corner at the location of Buoy 1 and the southeast corner at the eastern midpoint of the island of Kauai (Buoy 1 input model, Figure 2.1a). Forcing for the WW3 input model came from the WW3 nodes and gridded wind fields; for the Buoy 1 input model, Buoy 1 directional spectra were applied at all boundaries, and Buoy 1 measured winds applied uniformly over the domain. Directional spectra from these two input models were saved at points along the offshore local grid domain. These spectra (from both input models) were separately interpolated along the local grid's offshore boundaries to provide two sources of (local grid boundary) input.

2.2.4.3 Validation of local model simulations

The effect of differing boundary conditions (from the two input models above) and local model parameterizations on the prediction quality of the nearshore wave field was evaluated through examination of root-mean-square errors (RMSE) and biases associated with each model run. These metrics were calculated from differences in the corresponding sets of (model) predictions and (in situ) observations of H_s, T_p, and θ_p at available grid points (θ_p values crossing 360º were unwound). Measurement error in observed H_s, T_p, and θ_p variables were assumed to be trivial in comparison to model prediction errors [Willmott et al., 1985]. Bias error was used in addition to RMSE as it retains its sign (at individual locations), providing useful additional information on variable error linkages (e.g., showing underestimation of H_s linked to θ_p bias through underestimation of refraction).

RMSE were also normalized with their mean observed values during each model run, making errors between different variables commensurable [Willmott et al., 1985]. This allowed an overall normalized RMSE skill score (RMSSS) to be calculated for each model run ($\langle\ \rangle$ denotes the average of the enclosed quantities):

$$RMSSS = 1 - \frac{\left\langle (predictions - observations)^2 \right\rangle^{1/2}}{\left\langle (observations)^2 \right\rangle^{1/2}} \qquad [4]$$

This quantity is defined by Sutherland et al. [2004]; and similar to the scatter index (used by Ris et al. [1999] and others) and relative errors (used by Mulligan et al. [2008a] and Willmott et al. [1985]). The model performance and operational performance indices [Ris et al., 1999] were not used because incident wave height at the local model offshore boundary was not measured.

2.3 Results

2.3.1 Wave climate

The monthly H_s climatology illustrates the highly seasonal nature of the region's wave climate (Figure 2.2). In the summer H_s generally averages 2 m ± 0.5m; while mean wintertime H_s is only about 1 m higher, the range of observed heights is far greater, with mean monthly maximum wave heights in the range of 6–7 m during December, January, and February. This begins to illustrate the episodic nature of the large winter month observations. The directional wave climatologies (Figure 2.3) better illustrate the ubiquitous dominance of trade wind waves (H_s ~ 1.5 m, T_p ~ 6–8 s, θ_p ~ 60–115°) during the summer months; conversely, the winter months are dominated by episodes of northwest swells, (H_s ~ 2.5–3.5 m, T_p ~ 12–16 s, θ_p ~ 300–330°). More extreme events (H_s > 4 m, T_p ~ 16–20 s, θ_p ~ 300–330°) also occur with measurable regularity (~ 10 times in an average season), although much less frequently than the smaller, slightly shorter period NW swells (Figure 2.3).

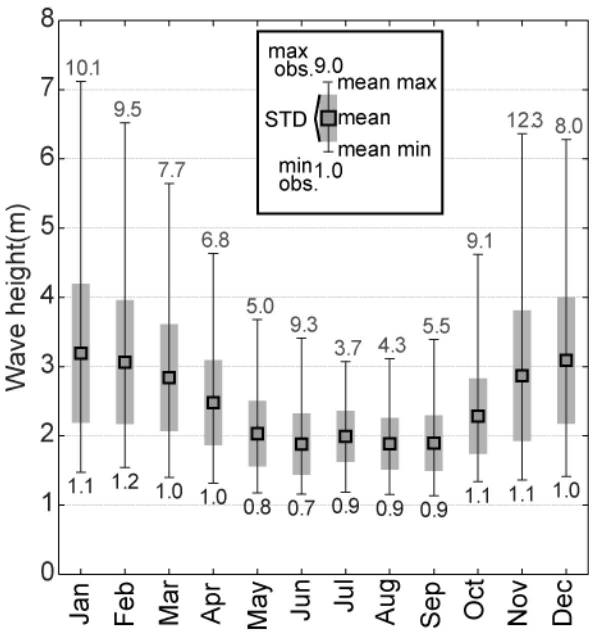

Figure 2.2: Climatological monthly mean, standard deviation, mean monthly min/max and total observed min/max significant wave height at Buoy 1 for years 1981 – 2009.

Recent Buoy 1 directional data are of much more limited temporal extent (3 years) than WW3 (11 years) and coincides roughly with the timing of this study. Although they are in good agreement, the Buoy 1 statistics show a greater occurrence of trade wind conditions in the winter and a slightly more northerly direction in most occurrences of NW swells. These subtle differences over the last few years from longer term means may be linked to inter- and intra- decadal climate oscillations [e.g., Rooney and Fletcher, 2005] or may be an expression of model bias, especially for the mature NW swell events [Hanson et al., 2006]. Further investigation of differences between short-term

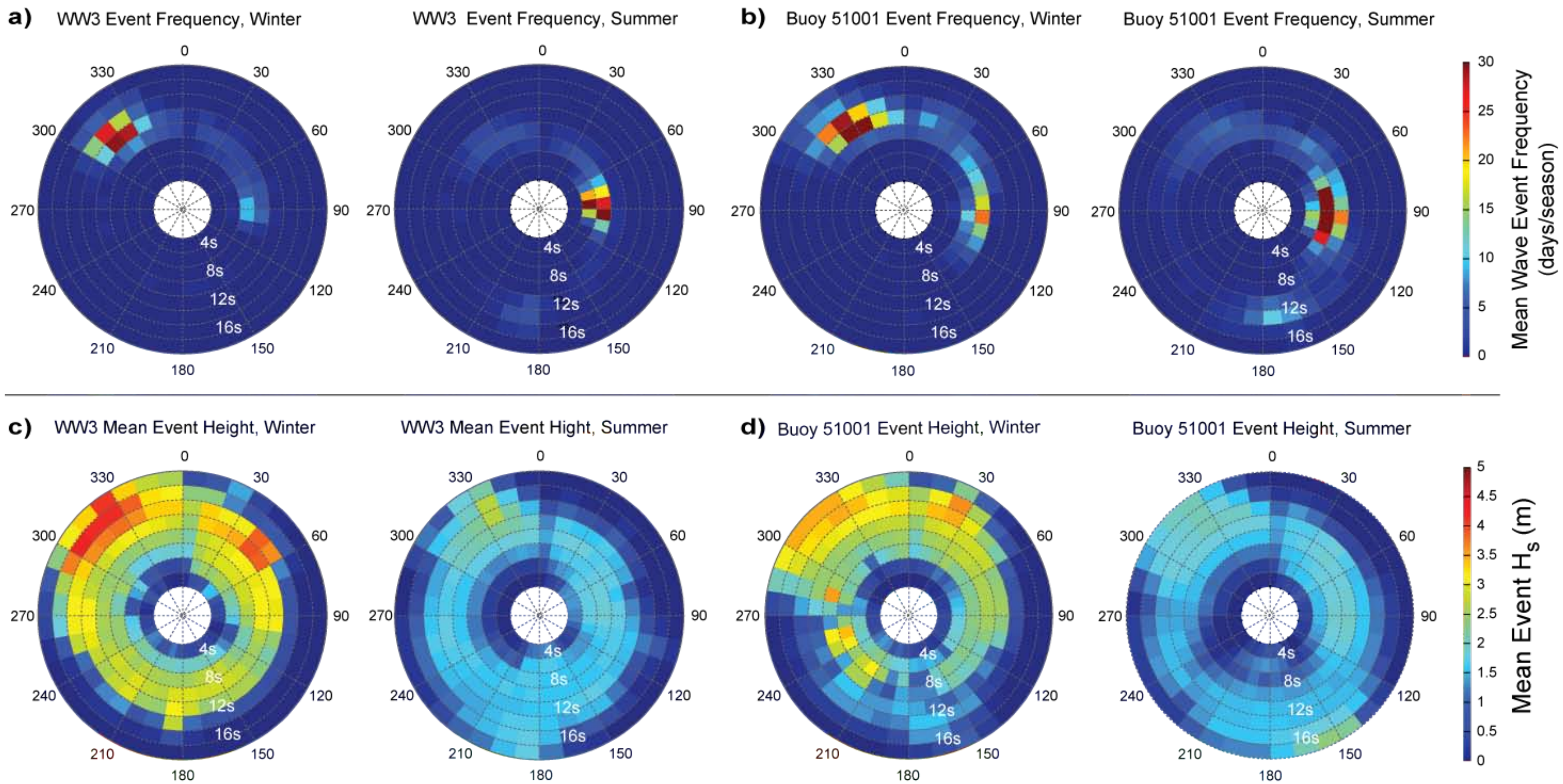

Figure 2.3: a–d. Seasonal directional wave climatologies generated from model hindcast data from 1996 to 2009 (WW3) and in situ buoy data, 2005 – 2009 (Buoy 1). (a) WW3 mean event frequency for November – March (winter) and May – September (summer). (b) Buoy 1 mean event frequency for winter and summer. Mean event frequency is defined as the occurrence of peak direction (θp) and peak period (Tp) in each directional/period bin in the historical data, normalized to represent mean number of days occurrence in each season; e.g., if the color indicates 30, then, on average, the condition occurs on 30 out of 150 days each season. Scaling for both (a) and (b) is given by the colorbar to the right. (c) WW3 mean significant wave height for all observations in each θp, Tp bin for summer and winter. (d) Buoy 1 mean significant wave height for summer and winter. Events occurring during the months of April and October, transition months, are omitted from the analysis for clarity.

(3 years) *in situ* derived and longer-term (11 year) model derived wave climatologies is beyond the scope of the work presented here.

The wave climatologies discussed above were used to classify conditions during the study period. Trade wind conditions were defined as E between 0.6 kJ/m^2 and 5.625 kJ/m^2 for $\sigma \geq 0.083$ Hz, θ between 45–135° sector (this corresponds to H_s ~ 1–3 m, T < 2 s), as measured in Buoy 1 spectra. NW swell conditions were defined as E > 2.5 kJ/m^2 in the $\sigma \leq 0.1$ Hz, θ between 295–360° sector (this corresponds to $H_s \geq$ 2 m, T > 10 s). These two classifications were not necessarily mutually independent, as simultaneous peaks in both areas of the directional spectrum often occurred, i.e., often both criteria were fulfilled during periods of when NW swells and trade wind conditions simultaneously occurred. Figure 2.4 shows *in situ* measurements during the study period and highlights times falling within one or both of the classifications: trade wind conditions were experienced 77% of the total time, while NW swells occurred 9% of the time. Both trade wind conditions and episodic NW swell conditions occurred 4% of the total time or 49% of the time during the swell events. Periods that fell outside of the two classifications were generally quiescent, both in terms of wave energy and winds.

2.3.2 Nearshore In-situ Observations

While trade wind waves reached height in excess of 3 m in height offshore several times during the study period, they never resulted in measured waves greater than 2 m, and were usually much less, inside the bay (Figure 2.4a). NW swell events, on the other hand, frequently resulted in measured wave heights in excess of 3 m, and at times in excess of 5 m, inside the bay (Figure 2.4a). Fundamental differences in both overall current magnitudes and circulation patterns within the bay under the two different conditions are also evident. With only two exceptions during the study period, currents measured at the Wall site remain below 0.20 m/s, usually on the order of 0.05 m/s, during trade wind conditions; during NW swell events, currents in excess of 0.50 m/s frequently occur (Figure 2.4d, Table 2.2).

Table 2.2 summarizes statistical differences between the two conditions as observed at the *in situ* monitoring sites. Significant correlations between wave heights and current magnitudes occur at all sites within the bay occur during NW swell events (r = 0.55 – 0.80), correlations with wind stress magnitude and (predicted) tidal elevations

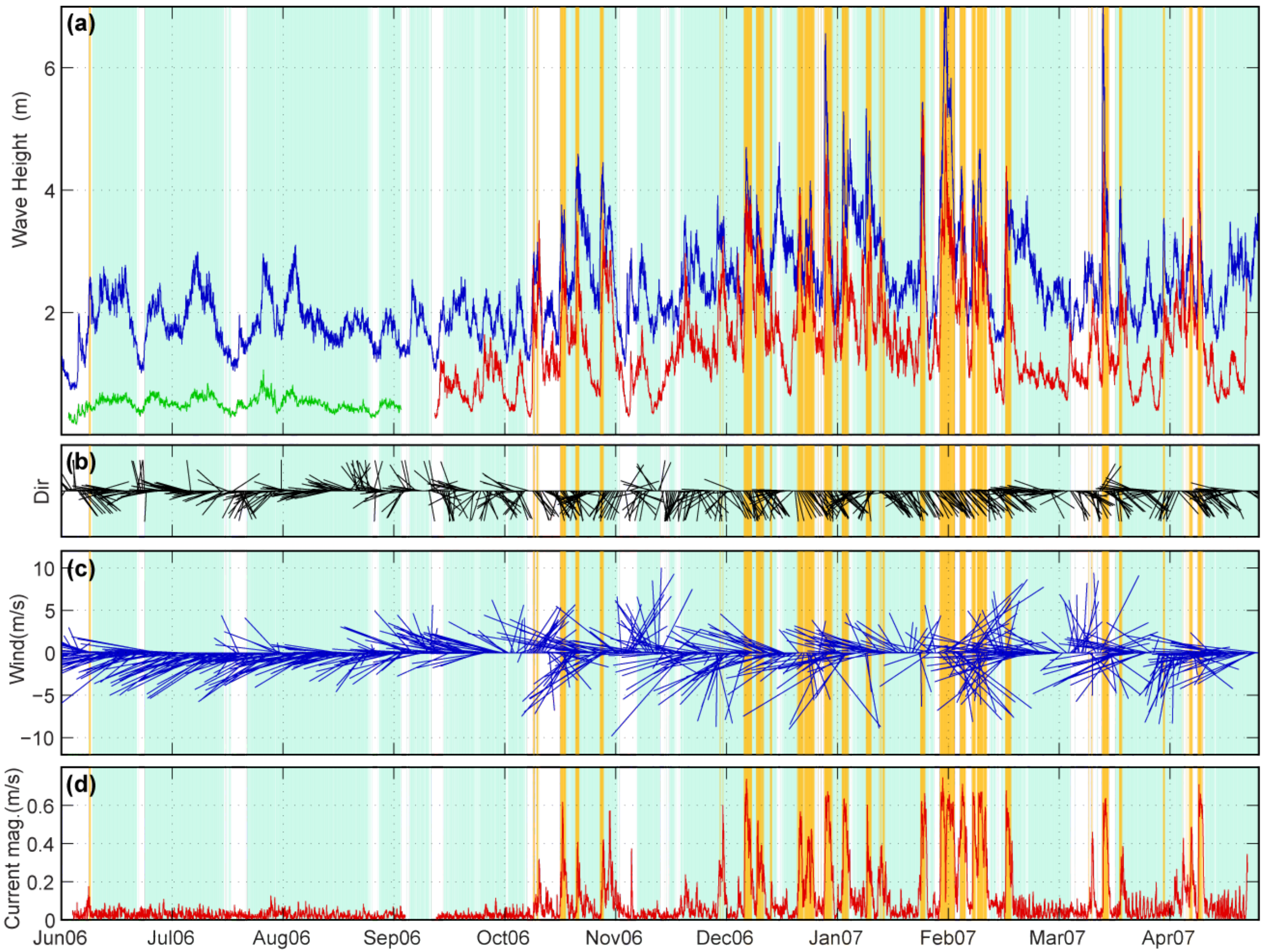

Figure 2.4: In situ waves, winds, and currents during observation period June 5, 2006 to April 10, 2007. (a) Significant wave heights at Buoy 1 (blue), CRAMP (green), and NW Reef (red) sites. (b) Daily mean wave direction at Buoy 1 CCW from true North; (c) daily mean wind vector at Buoy 1. (d) Current magnitude at Wall site. In all plots, trade wind conditions are identified with light blue bands, episodic NW swell conditions with yellow bands; note the two conditions are not mutually exclusive; conditions not classified as trade wind or NW swell (white areas) are generally quiescent. See the text for parameterization of the conditions.

are low (<0.15) or insignificant. Conversely, only the Wall site shows correlation between waves and currents throughout the water column during trade wind conditions (r = 0.43 – 0.53); other sites show higher correlation with tides and wind. Tide appears to contribute to the low currents magnitudes lower in the water column (r = 0.42 – 0. 54), while winds appear to contribute to forcing in the upper water column at the CRAMP and SC Reef sites (r = 0.42 – 0.46) and wind. Low modal river discharge (< 20 m^3/s over 95% from a stream gauge record of Hanalei River) and low vertical and horizontal density gradients (generally $\Delta\rho$ < 1kg/m^3) in observed conductivity, temperature and depth (CTD) profiles within the bay [Storlazzi et al., 2006; Storlazzi et al., 2008; National Marine Fisheries Service, 2006] suggest buoyancy forcing contributes little to overall flow regime during most conditions and thus is not included at a forcing variable in Table 2.2. While buoyancy forcing may become important during large freshwater discharges associated with occasional floods of the Hanalei River, due to their rarity [Draut et al., 2009] and the lack of observations of resulting salinity/density gradients, buoyancy forcing is not considered further in this paper.

Table 2.2: Mean and standard deviation (SD) of observed significant wave height (Hs) and current magnitude (|U|) at instrument sites during trade wind conditions and during NW swell episodes. Correlation between |U| and predicted tide (Rtide), squared wind speed (Rwind), and Hs at the most exposed ADCP site (Rwave) are given in following columns; significant correlation values (p<0.01) are indicated in bold. A grey background indicates values derived from near-bed ADCP bins (lowest approx. 1.5-m of the water column), white background indicates values derived from with the near-surface ADCP bins (upper most approx. 2 m of the water column). Blank values indicate insufficient data.

	Trade wind conditions					NW Swell				
	H_s (m) mean(SD)	$\lvert U\rvert$ (m s^{-1}) mean(SD)	R_{tide}	R_{wind}	R_{wave}	H_s (m) mean(SD)	$\lvert U\rvert$ (m s^{-1}) mean(SD)	R_{tide}	R_{wind}	R_{wave}
WALL	0.24(0.07)	0.05(0.07)	**0.21**	0.10	**0.53**	0.47(0.15)	0.37(0.21)	-0.01	-0.05	**0.64**
		0.03(0.04)	**0.54**	0.07	**0.43**		0.22(0.14)	-0.08	0.03	**0.71**
NW Reef	1.30(0.59)	0.09(0.05)	**0.29**	**0.41**	**0.46**	2.57(0.89)	0.21(0.13)	**0.12**	-0.08	**0.69**
		0.04(0.02)	**0.42**	0.05	**0.17**		0.09(0.07)	**0.15**	**0.13**	**0.63**
CRAMP	0.54(0.10)	0.14(0.10)	**0.39**	**0.46**	**0.24**		0.17(0.14)	0.68		**0.77**
		0.01(0.01)	**0.44**	**0.26**	**0.10**		0.02(0.01)	0.34		**0.28**
SC Reef		0.06(0.04)	**0.26**	**0.42**	**0.21**		0.06(0.03)	0.59		**0.80**
		0.02(0.01)	**0.46**	-0.06	**0.06**		0.02(0.01)	0.32		**0.55**

Differences in circulation patterns are further visualized though examination of the principle axes and Eularian mean currents under the two different wave conditions (Figure 2.5). During trade wind conditions, consistent with the weak but significant correlation of near-bottom currents with tidal elevations in Table 2.2, near bottom principal axes are poorly defined but roughly aligned with bottom contours and show little asymmetry at all locations; near surface means are roughly a factor of 2.2 stronger and tend to show significant net directions (asymmetry). On the western side of the bay, mean vectors are roughly aligned with the direction of the trade winds, suggesting onshore wind driven flow, while the mean vectors are oriented toward the shoreline on the eastern side of the bay (Wall site), suggesting wave driven flow, also supported the higher correlation of currents and waves at this site (Table 2.2). During NW swell events, currents at the Wall site are strongly oriented into the bay along the principle axis throughout the water column. Observations on the western side of the bay suggest that this flow tends to exit the western mouth of the bay, visible in the orientation of the principle axes at the NW Reef and CRAMP sites (Figure 2.5).

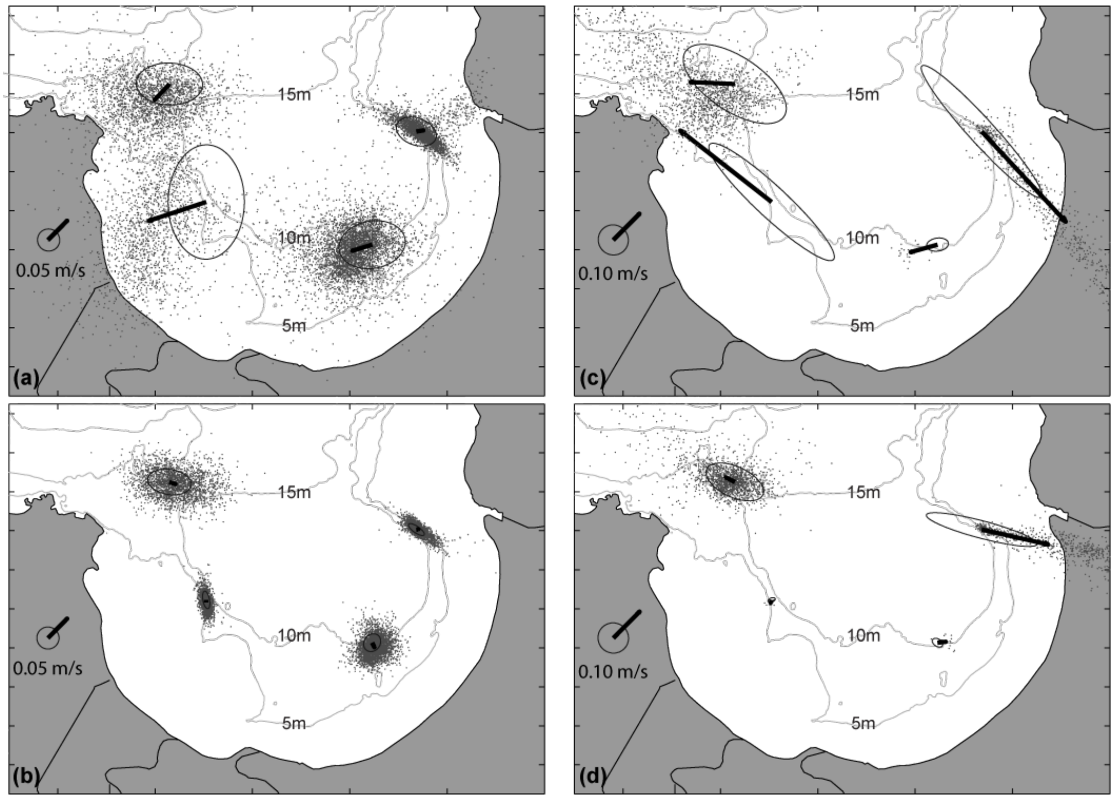

Figure 2.5: Variance ellipses and Eularian mean vectors of in situ ADCP data plotted at their respective locations in Hanalei Bay: (a) near-surface bin during trade wind conditions, (b) near-bottom bin during trade wind conditions, (c) near-surface bin during episodic NW swell events, and (d) near-bottom bin during NW swell events. In all plots, individual observations are indicated by scatter points; scaling is given by arrows and ellipses in the left area of each subplot. Note differences in scaling between subplots: (a) and (b) vector arrow and error ellipse scales corresponds to 0.05 m/s and u/v standard deviation of 0.02 m/s, respectively; (c) and (d) arrow and ellipse scales correspond to 0.1 m/s and 0.04 m/s.

The fact that the semi-major axis of flow is strongly oriented into the bay at the Wall site during NW swell events, and to a lesser extent during trade wind conditions, suggests that wave-driven flow over Hanalei reef is a significant circulation driver within the bay. Unfortunately, the bay's complex fringing reef topography and exceptionally high wave height at exposed locations during larger NW swell episodes (instrumentation typically will not survive) limit the availability of *in situ* observation locations. This has made the relationships between incident wave height (H_0), set-up (η) and resulting residual flows ($\overline{u}$) difficult to elucidate compared to similar studies where instrumentation has been deployed in transects perpendicular to relatively linear reef slopes, crests, and flats [e.g., Hearn, 1999; Gourlay and Colleter, 2005; Lowe et al., 2005; Lowe et al., 2009; Hench et al., 2008]. This difficulty is exacerbated by the nonlinear interaction of differing incident wave refraction patterns, tides, and wind.

To simplify this comparison and draw generalizations on the effect of waves on flow in the bay, we focused on the semi-major axis of current magnitude at the Wall site, which shows the greatest dependence on wave conditions and small variance in the semi-minor direction (Figure 2.5). It was hypothesized that a large part of the observed variance in current would be proportional to the available wave energy flux (power) in the vicinity of the offshore reef slope:

$$\overline{u} \propto EC_g \qquad [1]$$

Unit power can be estimated using the definitions of energy (E) and group velocity (C_g) from linear wave theory (Dean and Dalrymple 2009], where g is gravitational acceleration, ρ is density of seawater h is mean water depth, and k is the wave number:

$$EC_g = \frac{1}{8}\rho g H_s^{\,2} \cdot \frac{g}{\omega}\tanh(kh) \cdot \frac{1}{2}\left(1 + \frac{2kh}{\sinh kh}\right) \qquad [2]$$

When the depth-averaged velocities along the semi-major current axis (defined by NW swell conditions, Figures 2.5c,d) for all conditions at the Wall site ($\overline{u}_p$) are plotted against EC_g calculated from wave parameters measured at the NW Reef Site (assumed to be a representative H_0 immediately offshore of Hanalei Reef), a significant linear relationship is evident (Figure 2.6a, r^2 = 0.69). The variability in this observed relationship can be further reduced by finding the first empirical

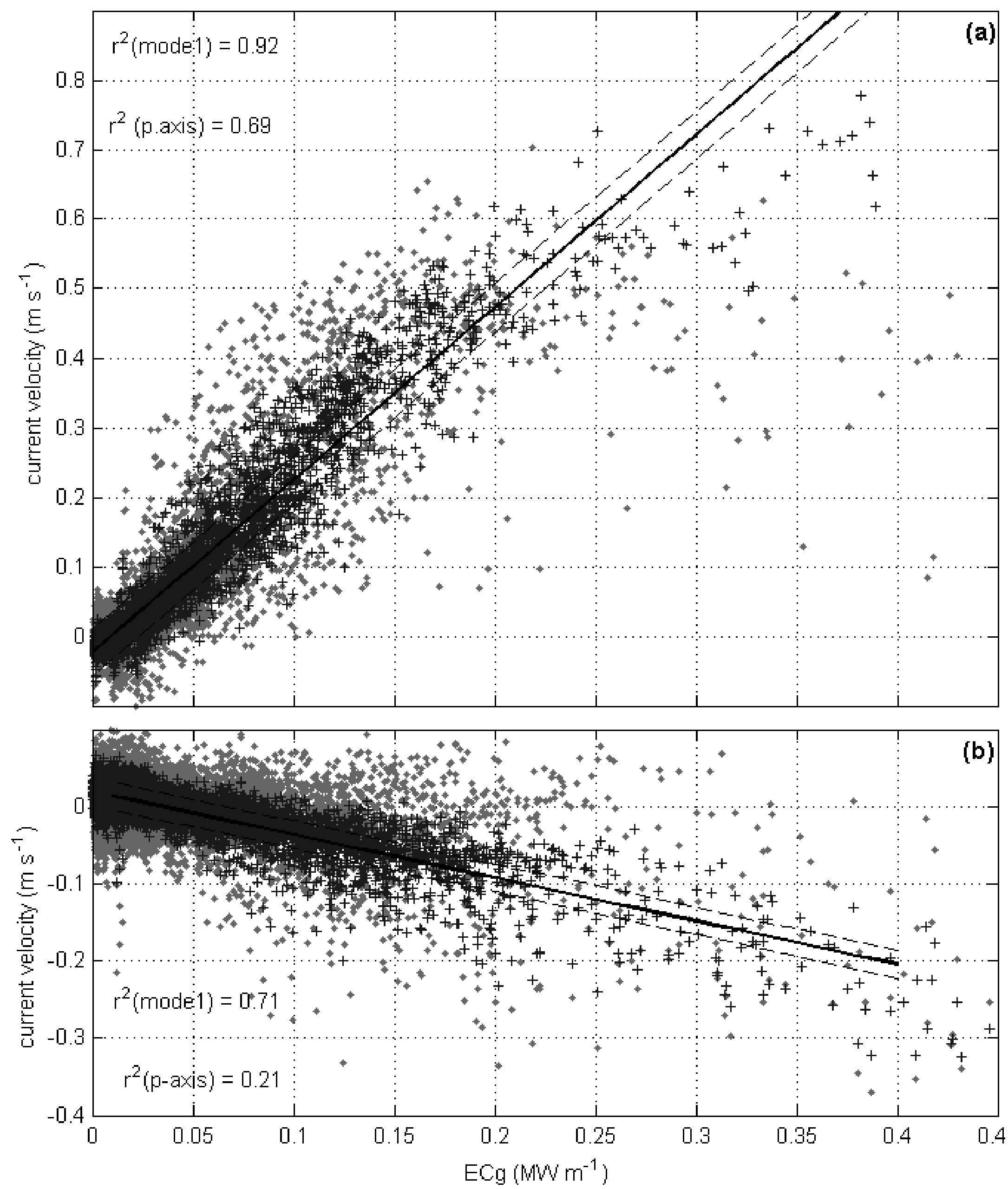

Figure 2.6 (a) Depth-averaged current magnitude along semi-major axes ($\overline{u}_p$) at the (a) Wall site and at the (b) NW Reef site, both compared to wave energy flux values at the NW Reef site (EC_g). In both (a) an (b), points correspond to unfiltered $\overline{u}_p / EC_g$ observations; crosses to the first EOF mode of the data. Semi-major axes are defined by NW Swell conditions at there respective sites, e.g. Figure 5c and 5d; positive values indicate flow along an axis oriented into the bay, negative values indicate flow out of the bay. The solid and dotted lines are the (linear) regression line and the 50% error bounds, respectively.

orthogonal function (EOF) of the $\overline{u}_p / EC_g$ covariance matrix [Emery and Thomson, 2001]. This effectively filters out tides (band-pass filtering for tides was confounded, since swell events typically had frequencies on the order of a day), as well as other unknown forcing mechanisms. The first EOF mode described 92% of the observed variance of the data (Figure 2.6a), indicating that wave-driven flow dominates overall flow at the Wall site, even when available EC_g in the bay is small, typically during trade wind conditions.

A similar, though less significant, relationship can be found for the (depth-averaged) current velocities ($\overline{u}_p$ oriented along the semi-major axis during NW swell conditions) and EC_g can be observed at the NW Reef site (1st mode EOF r^2 = 0.71, Figure 2.6b). This axis is primarily oriented out of the bay (Figure 2.5c, d). This further confirms that (wave energy dependent) flow over the bay's bordering reefs exits out the wide mouth of the bay, while the lower dependence suggest that this flow is less constrained by topography and more variable than that observed at the Wall site.

If $\overline{u}_p$ at the Wall site, linearly related to incident EC_g (Figure 2.6a), is assumed to be representative of water flow over the morphologic feature of the "Wall", then the integration of $\overline{u}_p$ along this ~450m long, ~2m deep feature suggests volume fluxes on the order of 150 m^3/s and 400 m^3/s for H_0 = 2 m and H_0 = 3, respectively. Calculating the volume of the bay inshore of the headlands as 1.90×10^7 m^3 below mean water level, flushing (residence) times for the bay are estimated to be on the order of 40 hours and 15 hours from the above respective fluxes. The actual flushing times are likely less, since wave-driven flows over other reefs in the bay likely also contribute to the overall flushing. The importance of the contribution of wave action on this one reef to mean flushing of the bay is highlighted when compared to a simple, classical tidal-prism flushing estimation [Luketina, 1998]. Defining the tidal prism as the volume difference between mean ebb and flood tidal levels suggests tidal flushing is on the order of 150 hours.

2.3.3 Wave Model Simulations

The conditions during the two one week periods selected for simulation of the nearshore wave field, August 2–9, 2006 and January 20-27, 2007, were respectively categorical of the trade wind and NW swell classifications. Wave conditions during the trade wind period gradually varying H_s of 1.5–3.0 m, T_p of 7.5-10.0 s, and θ_p of

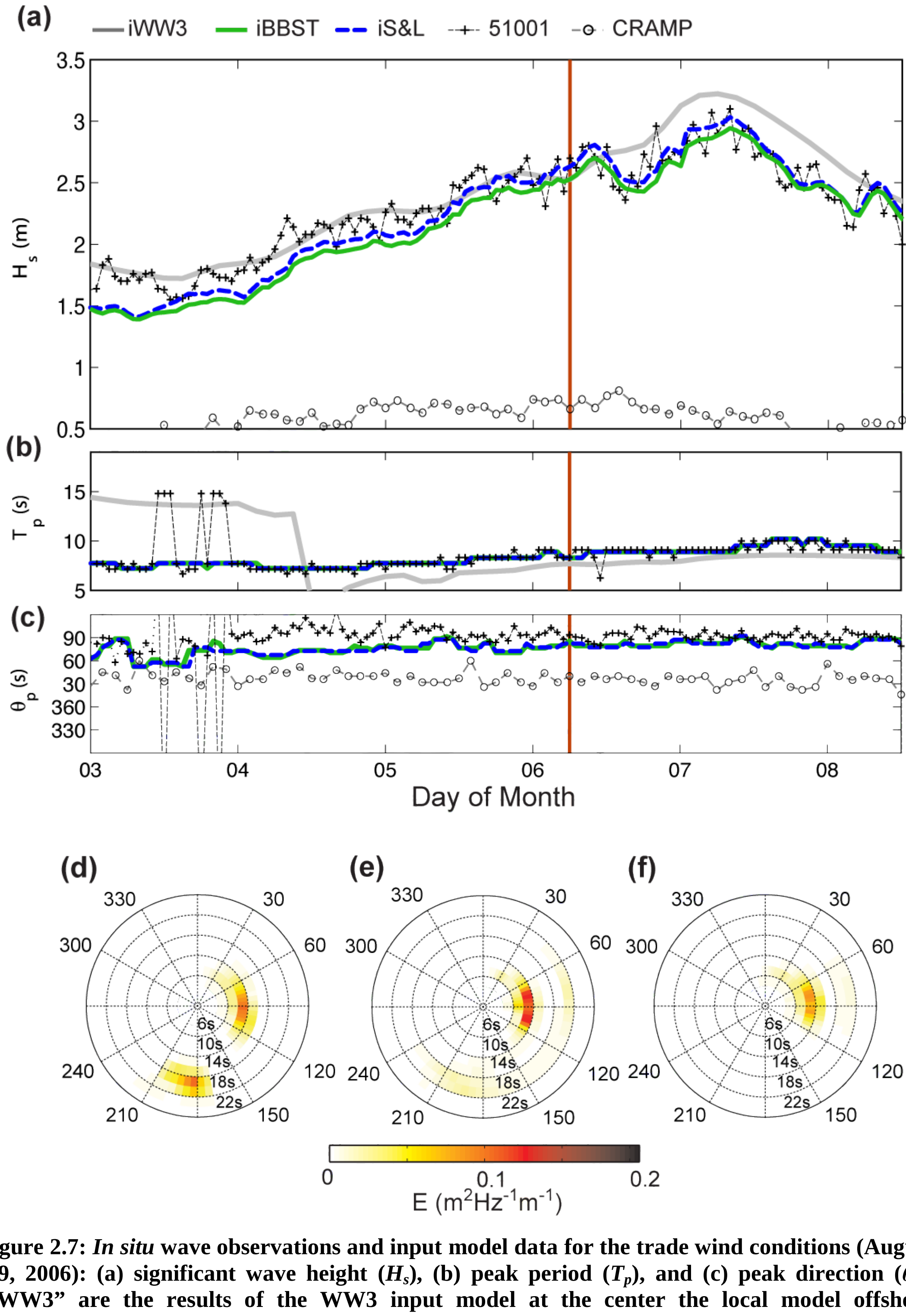

Figure 2.7: *In situ* wave observations and input model data for the trade wind conditions (August 2-9, 2006): (a) significant wave height (H_s), (b) peak period (T_p), and (c) peak direction (θ_p). "iWW3" are the results of the WW3 input model at the center the local model offshore boundary; "iBBST" are the results of the Buoy 1 input model using BSBT; and "iS&L" are the results of the Buoy 1 input model using S&L (see text for description of these terms). Buoy 1 and CRAMP *in situ* data are plotted for comparison; the vertical red line indicates time of accompanying spectra (d-f). (d) WW3 input spectra, NW corner; (e) Buoy 1 input spectra; (f) Local model input from Buoy 1 input model. The time series plot and the three spectra indicate the close correspondence of the WW3 and Buoy 1 input with each other as well as the resulting modeled conditions at the offshore boundary. A long period southern hemisphere swell is visible in (d) and (e); this is shadowed by the island of Kauai and thus nonexistent in (f).

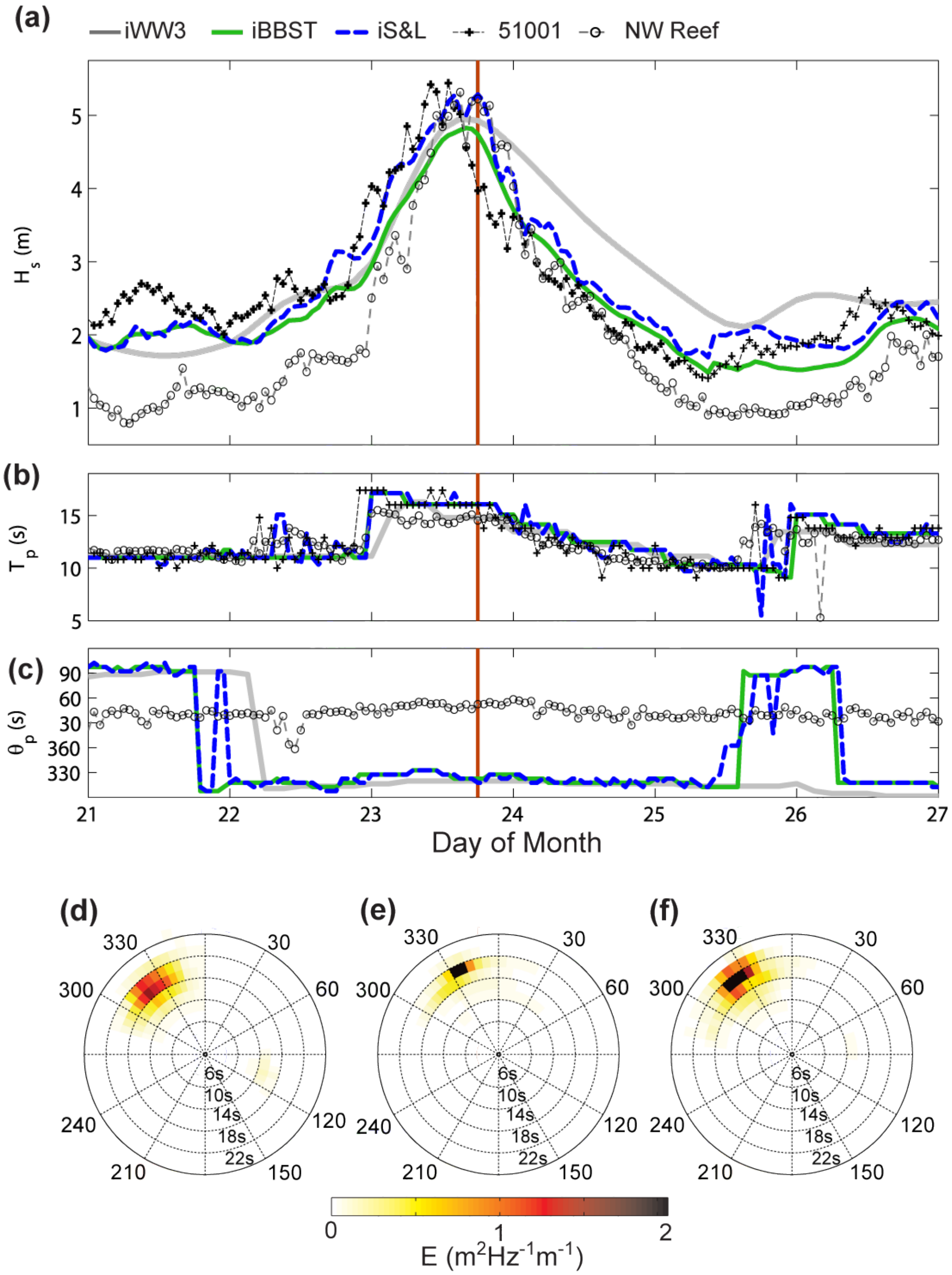

Figure 2.8: *In situ* wave observations and input model data for the NW swell event (January 20-27, 2007): (a) significant wave height (H_s), (b) peak period (T_p), and (c) peak direction (θ_p). "iWW3" are the results of the WW3 input model at the center the local model offshore boundary; "iBBST" are the results of the Buoy 1 input model using BSBT; and "iS&L" are the results of the Buoy 1 input model using S&L (see text for description of these terms). Buoy 1 and NW Reef *in situ* data are plotted for comparison; the vertical red line indicates time of accompanying spectra (d-f). (d) WW3 input spectra, NW corner; (e) Buoy 1 input spectra; (f) Local model input from Buoy 1 input model. The time series plot indicate differences between WW3 and Buoy 1 input and the resulting boundary conditions at the local model; use of either BSBT propagations or WW3 input tends to underestimate H_s relative to observed *in situ* H_s at the model boundary. The WW3 spectra is visibly more diffuse than that of Buoy 1 near the peak of the swell (d) vs. (e); Buoy 1 input spectra leads to focused spectral energy at the local model boundary (f).

80–100° at Buoy 1 (Figure 2.7). Some long-period south swell (T ~ 15.0 s) occurred during the week, but as the area immediately offshore of the study site is completely sheltered from this direction, it is not considered relevant to the study. Buoy 1 measured consistent trade winds during this period (~ 6–12 m/s from 60 to 90°). Maximum wave heights recorded in the bay during this period were H_s = 0.8 m and H_s = 0.4 m, at the CRAMP and Wall sites, respectively. By contrast, the NW swell period saw a large, but not unusual, NW swell event; starting on January 23, trade wind conditions rapidly gave way to increasing NW swell. At the swell's peak, Buoy 1 measured H_s = 5.5 m, T_p = 17.5 s, and θ_p = 330° before subsiding back to trade wind conditions by January 26 (Figure 2.8). Buoy 1 winds during the period were measured between 0 and 9 m/s, and winds rotated clockwise from the southwest to east, with northerly winds around 9 m/s preceding the peak of the swell by about 12 hours. Maximum wave heights recorded in the bay were H_s = 5.3 and 0.9 m at the NW Reef and Wall sites, respectively.

Efforts to minimize differences between observed (*in situ*) and modeled wave conditions in the bay resulted in a large number of input model simulations (~ 30) and local model simulations (~ 70). The WW3 input model generally showed excellent agreement with the Buoy 1 input model during the trade wind condition (Figure 2.7). During the January NW swell event, however, offshore WW3 input model energy was distributed over a broader range of frequencies and directions compared to the focused wave energy produced by Buoy 1 input model. This more diffuse WW3 input generally resulted in smaller H_s within the bay compared to the Buoy 1 input model (Figure 2.8) and poorer model skill scores. This implies that the Buoy 1 input model produced more realistic boundary conditions, especially during large mature swell events. As noted previously, inaccuracies in WW3 hindcasts during large mature North Pacific swells have been reported [Hanson et al., 2006].

Both the input models and the local model also proved sensitive to the numerical propagation formulation. First-order propagation schemes (e.g. backward space, backward time, "BSBT") proved far too diffusive in both the input models and the local model, leading to output that smoothed over stochastic patterns common between Buoy 1 data and *in situ* data within the bay during NW swell conditions. The third-order Stelling/Leendertse ("S&L", Rogers et al. [2002]) scheme proved far more satisfactory (Figures 2.7, 2.8) for the input models, while the second-order upwind

("SORDUP", Rogers et al. [2002]) scheme in quasi-stationary (stationary computations in nonstationary mode) provided best results for the local model, in most cases (Figures 2.9,2.10, and 2.11). All model results discussed in the remainder of this section were generated using quasi-stationary SORDUP propagation in the local model with input from the Buoy 1 model in nonstationary mode with S&L propagation.

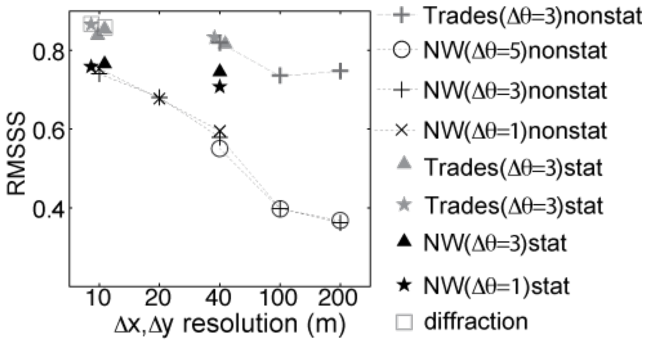

Figure 2.9: Comparison of overall composite root mean square skill scores (RMSSS) for selected local model runs utilizing 3rd-order (S&L) propagation Buoy 1 input; spatial (Δx, Δy) resolution of each run is given on the x-axis; the legend indicates modeled condition (Trades and NW for NW swell) and salient model parameterizations: directional spectral resolution in degrees (e.g. Δθ = 3) and propagation as 'nonstat' for nonstationary first-order and 'stat' for stationary second-order. The overall composite score is calculated by averaging all RMSSS for H_s and θ_p at all *in situ* instrument locations; T_p is not included in the composite score since low variability in wave periods diluted (increased) poorer skill values.

Local model predictions were sensitive to directional resolution and particularly spatial resolution of the computation grid (Figures 9, 10, 11). Considering the complex bathymetry of the bay, it is not surprising that 200- and 100-m spatial resolution grids did not adequately describe propagation patterns and led to poor estimates of H_s within the bay. This is particularly true during the NW swell event; the peak measured H_s at the NW Reef site was underestimated by 2.5 m or more and overestimated at the Wall site (Figure 2.10). Spatial resolution of 40 m or less performed far better, with successively finer spatial and directional resolutions generally improving comparisons with measurements; the highest resolution simulations (Δx, Δy = 10 m, Δθ = 1°) modeled refraction of up to 75° at both the NW Reef and Wall site. Still, even high-resolution simulations tended to underestimate θ_p, particularly at the NW Reef site during NW swell conditions (Figure 2.11). The model's poorer performance during the peak of the NW swell may also be partially due to not accounting for current-induced refraction (Mulligan et al., 2008b); this effect would be relatively greater during periods of high-wave-induced current. Model output was far less sensitive to spatial and directional resolution during trade wind conditions (Figures 9, 10).

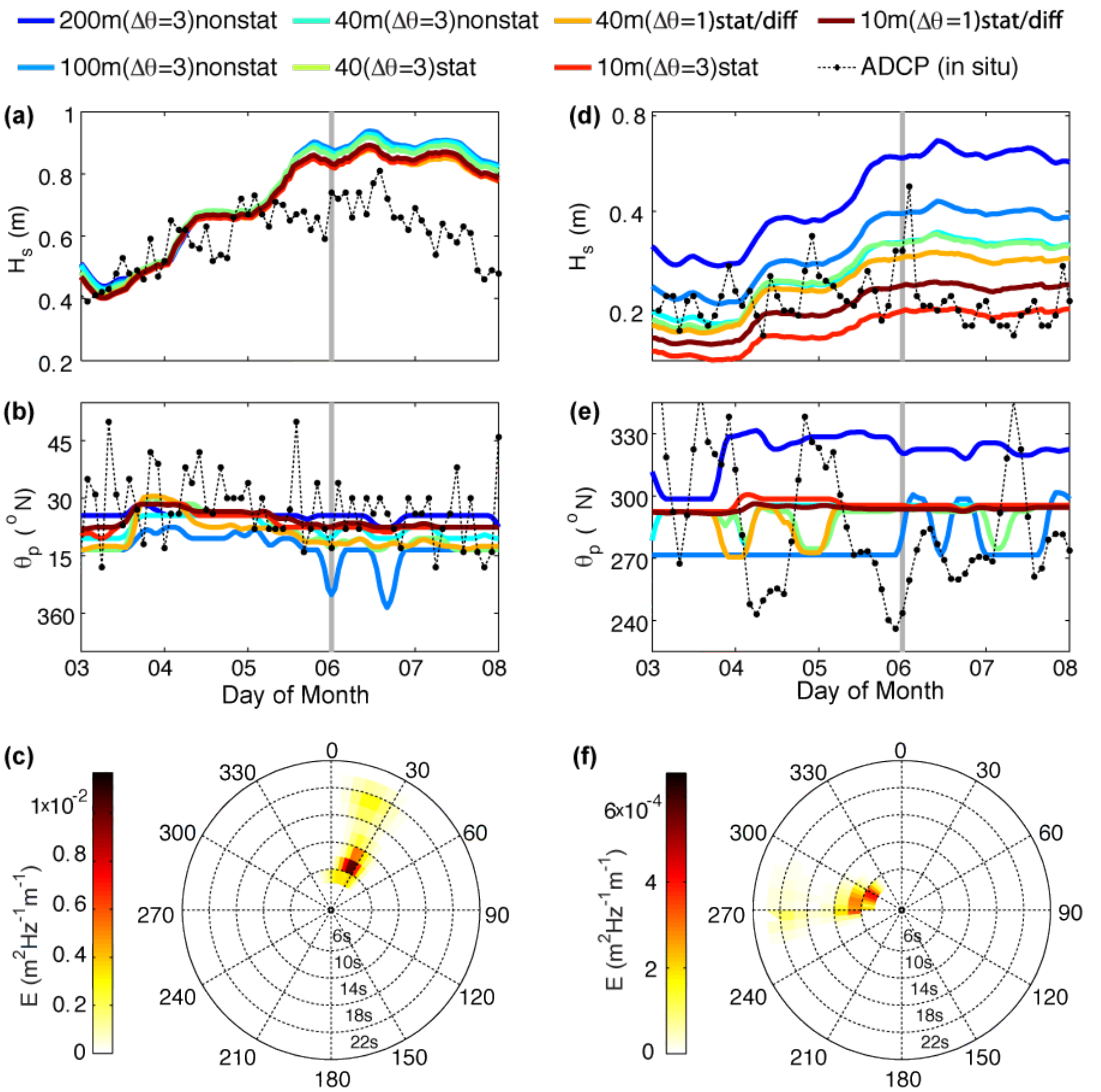

Figure 2.10: Comparison of varying model simulation resolution and propagation with *in situ* data during trade wind conditions, Aug 2-9, 2006. In the legend, the spatial resolution is given (e.g., 200 m), the directional resolution in degrees (e.g., Δθ = 3), and propagation as 'nonstat' for nonstationary first-order and 'stat' for stationary second-order are defined; if diffraction is included, 'diff' is added. (a) H_s at the CRAMP site. (b) Peak direction (θ_p) at the CRAMP site. (c) CRAMP model spectrum for the highest resolution run (10 m(Δθ = 3)stat/diff). (d) H_s at the Wall site. (e) Peak direction (θ_p) at the Wall site. (f) Wall model spectrum for the highest resolution simulation (10 m(Δθ = 1)stat/diff). The time of the spectra are indicated with a grey bar in the time series plots.

The inclusion of phase-decoupled estimated diffraction [Holthuijsen et al., 2003] improved results at the Wall site under trade wind conditions (Figures 2.9, 2.10), indicating diffraction is an important process along the neighboring near-vertical reef slope. Higher-resolution simulations of the NW swell that included diffraction failed to converge. Neglecting diffraction explains poorer model performance under NW swell conditions when the spatial resolution of the model is increased from 40 m to 10 m and directional resolution from Δθ = 3° to 1° for

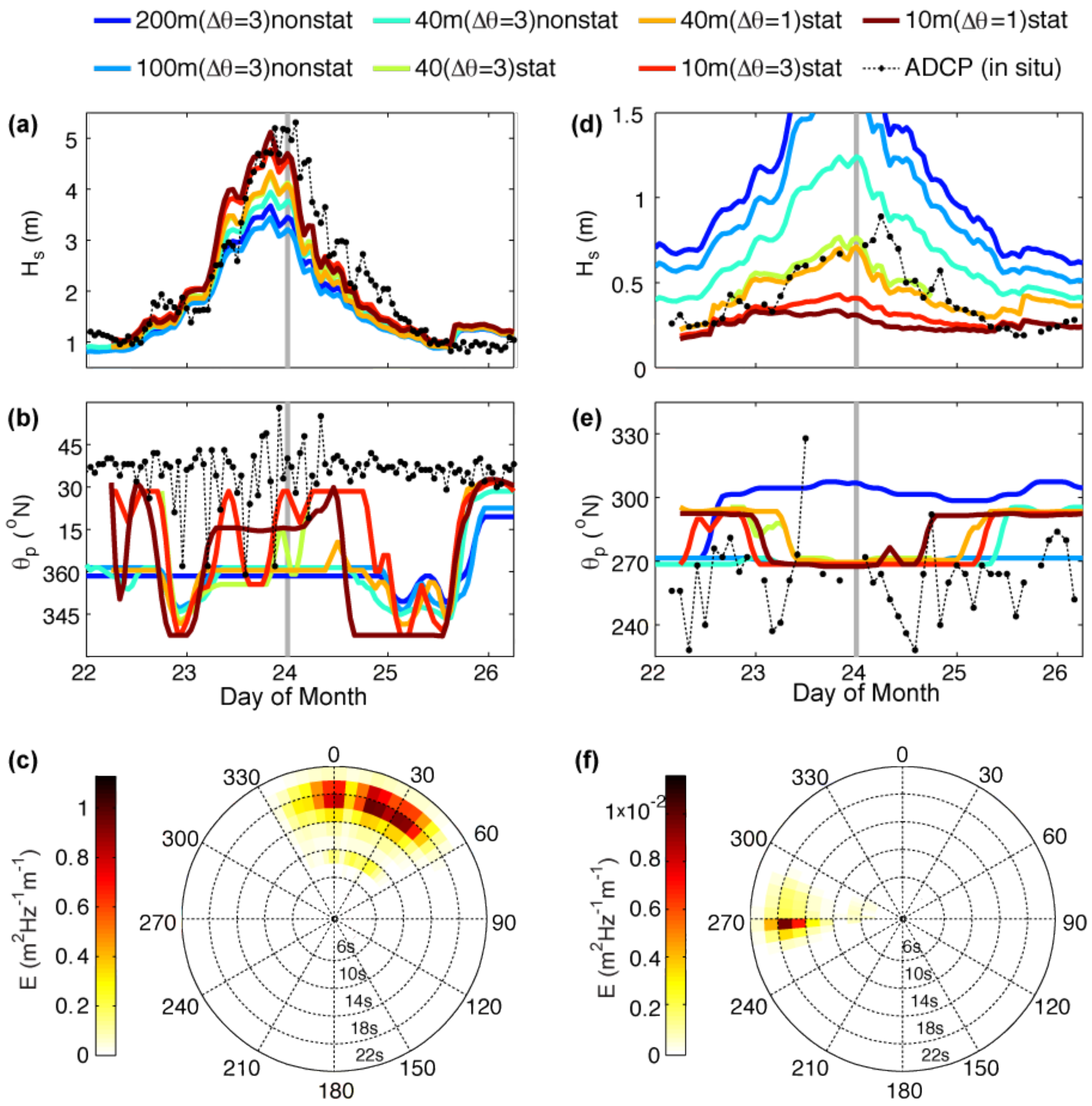

Figure 2.11: Comparison of varying model simulation resolution and propagation with *in situ* data during NW swell event, January 20-27, 2006. In the legend, the spatial resolution is given (e.g., 200 m), the directional resolution in degrees (e.g., Δθ = 3), and propagation as 'nonstat' for nonstationary first-order and 'stat' for stationary second-order are defined; if diffraction is included, 'diff' is added. (a) H_s at the NW Reef site. (b) Peak direction (θ_p) at the NW Reef site. (c) NW Reef model spectrum for the highest resolution run (10 m(Δθ = 3)stat/diff). (d) H_s at the Wall site. (e) Peak direction (θ_p) at the Wall site. (f) Wall model spectrum for the highest resolution simulation (10 m(Δθ = 1)stat/diff). The time of the spectra are indicated with a grey bars in the time series plots.

SORDUP propagation cases (in contrast to all other cases, Figure 2.9). This drop in skill scores is due solely to poorer H_s prediction at the Wall site (higher RMSE and bias). While the more spatially complex estimation of refraction at higher resolution is likely more realistic (H_s prediction is improved at higher resolutions at the NW Reef site), it leads to an underestimation of H_s at the Wall site (Figure 2.11), presumably because the lateral transfer of wave energy along the crest is neglected.

Varying bottom roughness in the different simulations did not lead to large differences in the results at the more exposed CRAMP and NW Reef site in either trade wind or NW swell conditions. Roughness lengths (k_w) of 0.01 m and 0.10 m for sand and reef areas, respectively, generally optimized results at the Wall site; these values for reef are in the range of that found in previous studies [Hearn et al., 2001; Lowe et al., 2005].

The high resolution simulations focus wave rays in complex patterns during the long wave lengths of the NW swell event: the deeper offshore reef at the mouth of the bay (King's Reef) can be seen focusing wave energy on fringing reefs on either side of the bay (Figure 2.12). The NW Reef site appears to be a zone where wave rays coming from directly offshore converge with wave rays refracted over King's Reef, resulting in a split spectrum (Figure 2.11). There is some evidence for this in the NW Reef observations and may explain why observed H_s at the site approaches or even exceeds offshore H_s, during periods of T_p greater than 15 s.

The large difference in wave fields within the bay during the two conditions (trade winds and NW swell) undoubtedly leads to large differences in the mobilization of sediment. Storlazzi et al. [2009] suggests a minimum bed shear stress of approximately 0.10 N/m^2 is required to mobilize the finer terrigenous and marine (calcareous) sediments in the bay; bed shear due to waves (τ_w) can be parameterized with the simple expression [Madsen et al. 1988; Lowe et al., 2005]:

$$\tau_w = \frac{1}{2}\rho f_w {u_b}^2 \qquad [5]$$

where u_b is the representative maximum near-bed horizontal orbital velocity calculated by the model and f_w is a semiempirical wave friction factor based on u_b, k_w, and σ. Under trade wind conditions, τ_w remains below 0.10 N/m^2 throughout the sandy floor of the bay and across much of the deeper (h > 5 m) forereef areas and in the backreef areas of the western side of the bay, between the mouths of Waikoko and Waipa streams (Figure 2.13). Under NW swell conditions, τ_w less than 0.10 generally is confined to a small area that coincides almost exactly with the observed 'Black Hole', the area of consistent fine-grained organic-rich sediments off the mouth of the Hanalei River (Figure 2.13). While still at minimum values within the bay, this area experienced (calculated) τ_w greater than 0.10 N/m^2 during the very peak of the NW swell. This suggests that the sediments are occasionally reworked by larger events; evidence for this is presented by Draut et al. [2009].

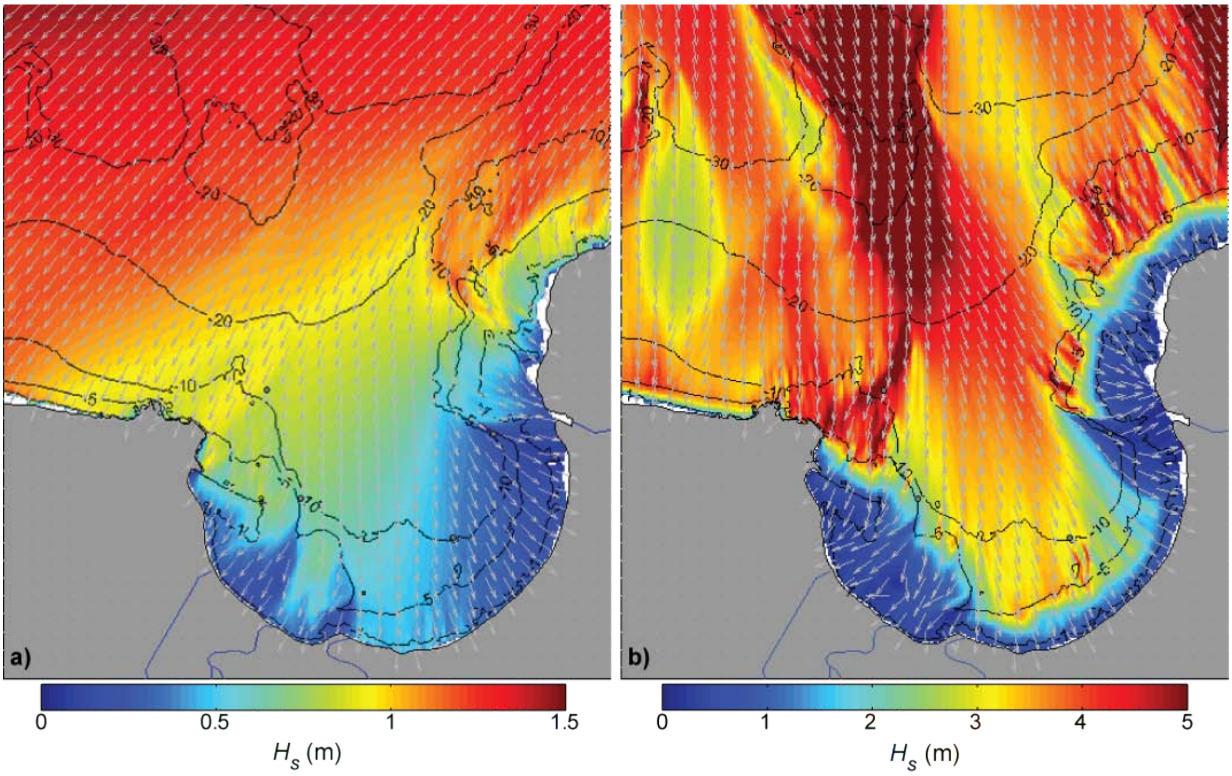

Figure: 2.12: Modeled significant wave height (H_s) with peak direction (θ_p) indicated by arrows. (a) Trade wind conditions (12:00 August 5, 2006); (b) NW swell event (06:00 January 24, 2007). Note the difference in color scaling between (a) and (b).

In other areas of the bay, τ_w is well into the range that may cause dislodgement of coral colonies [Dollar and Tribble, 1993; Storlazzi et al. 2005; Madin and Connolly, 2006] during the peak of the NW swell, reaching well over 20.0 N/m^2 on the more exposed outer fringing reefs. The overall estimations of τ_w corroborate extremely well with sedimentary evidence within the bay [Calhoun et al., 2002; Draut et al., 2009; Storlazzi et al., 2009] and with the low reported coral cover on the shallow, exposed forereefs (< 23%, Friedlander and Brown [2005]). Flow calculations were not included in this modeling effort; therefore bed shear estimates do not include contributions from residual currents, which are likely quite strong during the more energetic events, especially in the backreef areas. Overall flushing rates of water and sediment transport cannot be quantitatively estimated by the wave modeling data alone. Wave/current interaction, which may be important, is also not accounted for in this effort. The estimates of flushing times through coupled circulation modeling and implications sediment transport are addressed in Chapter 3.

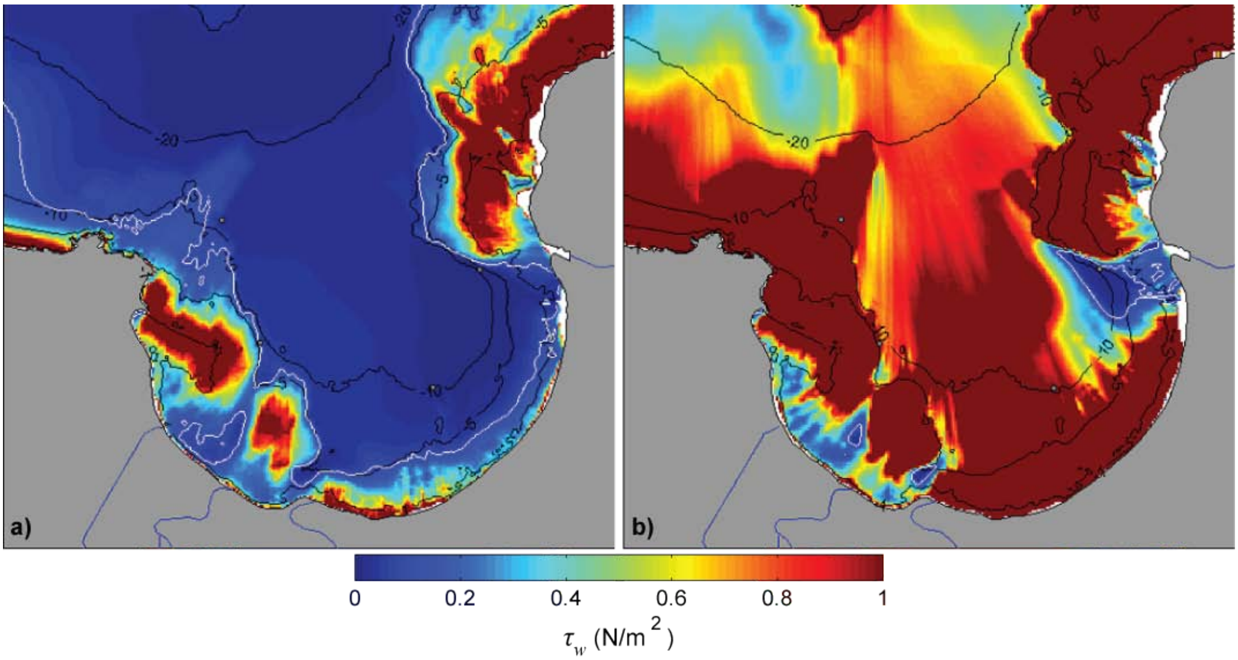

Figure 2.13: Calculated bed shear due to waves (τ_w) for (a) Trade wind conditions (12:00 August 5, 2006); (b) NW swell event (06:00 January 24, 2007). The same color scales are used in both subplots for comparison and areas of τ_w< 0.1N/m^2 are contoured in white.

2.4 Conclusions

Unlike more linear barrier type reefs, where the magnitude of flows may be related to incident wave height but overall circulation patterns are essentially similar under varying wave conditions [e.g. Hench et al., 2008; Lowe et al., 2009], the more complex and incised bathymetry of Hanalei Bay gives rise to fundamentally different circulation patterns under different wave conditions.

During trade winds, when little NW swell is present, flows within the bay show mixed influence of winds, tides, and waves. Circulation consists primarily of wind-and-wave (residual) flow around 0.10– 0.20 m/s near the surface, and weak, tidally dominated flows at depth (<< 0.05 m/s; Figures 2.4, 2.5, Table 2.2), possibly with an extremely weak onshore or counterclockwise residual component at depth [Storlazzi et al., 2009]. The (wind-driven) onshore surface component on the western side likely results in counterclockwise return flow along the shoreline (also suggested by Calhoun et al., [2002]). These trade wind conditions dominate throughout the year, but particularly in summer. Based on the observed relationship between nearshore wave energy and water flux into the bay, overall flushing times for the bay in these conditions are likely considerably greater than around 40 hours.

When NW swells (the most prevalent episodic condition) occur in the fall, winter and spring, wind and tidal forcing are increasingly overshadowed by depth-integrated flows, generally observed to be in the range 0.2 - 0.7 m/s (Figures 2.4, 2.5, Table 2.2). A strong asymmetry along the principal axis of flow is directed into the bay on its eastern side, the result of wave-driven flow across Hanalei Reef, with a return flow out the mouth of the bay, particularly during larger wave events (Figure 2.5, 2.6). This develops an overall picture of strong wave-dominated, clockwise residual flow throughout the water column during NW swell events, although the picture is likely complicated by small-scale, wave-driven circulation cells, unresolved with the limited ADCP data, particularly in the complex topography on the western side of the bay (Queen's Reef). The magnitudes of flows during these events are highly correlated to offshore incident wave energy flux (Figure 2.6) and flushing times are likely significantly less than about 14 hours, depending on the level of incident wave energy.

These fundamental differences in circulation between the two most commonly occurring wave conditions are due to the propagation of wave energy into the bay's interior during NW swell events. The complex refraction patterns and rapid dissipation of wave energy along the bay's fringing reefs in these conditions result in sharp gradients of radiation stress that drive the observed residual flows (Figure 2.12). By contrast, the shorter wave lengths associated with trade winds are not significantly refracted by King's Reef and other deeper reef structures; therefore, much less available wave energy, already propagating at a more oblique angle to the coast than NW swells, is refracted into the bay (Figure 2.12).

The greater vigor of circulation during NW swell events, particularly near the sea-bed, coupled with the large bed-shear stress generated by the near bed orbital velocities associated with the swell propagating into the bay (Figure 2.13), indicate that these episodic events are a primary driver of sedimentation/erosion, water quality, and benthic ecology. This is evidenced by sediment characteristics within the bay [Calhoun et al., 2002; Draut et al., 2009]; by observations of the re-suspension of sediment [Storlazzi et al., 2009]; and by the low reported coral cover on the shallow, exposed forereefs (2-15%) compared to elsewhere in the bay (24-47% of hardbottom substrates, Friedlander and Brown [2005]). Given the low annual number of these NW swell events (on the order of 10/year [Vitousek and Fletcher 2008], occurring

~9% of the time) compared to the frequency of modal trade wind conditions (~75% of the time), water quality and sediment and ecosystem dynamics may be sensitive to changes in the magnitude and annual recurrence of these events.

The incised, fringing reef embayment morphology of Hanalei Bay is common to tropical and subtropical high islands in the Pacific, Indian, and Atlantic Oceans. Numerous other examples may be found not only in the Hawaiian Islands, but in the also in the Mascarene Islands, Samoa, and the Caribbean. Similar to the Hawaiian Islands, many of these islands are in the trade wind belt but are exposed to long period swells generated by (often geographically distant) mid- and high- latitude cyclones, as well as occasional impacts from tropical cyclone waves, as shown by a number of studies of extreme wave events and wave climate [e.g. Caldwell 2005; Vitousek and Fletcher 2008; Bromirski, et al. 2005]. However, these studies either neglect wave direction or focus solely on the most extreme events. As evidenced by this study, the degree and frequency with which both these episodic swells and more moderate wind waves may affect circulation, and thus sediment processes and benthic ecosystem dynamics, depends heavily on the degree to which these waves propagate into a particular bay. This in turn depends heavily these waves' dominant direction, the orientation of the coast, and the morphology of the particular bay in question. Thus understanding coastal dynamics where wave-driven flows are important depends heavily on the directional aspect of both modal and episodic wave climate. The methods for producing seasonal directional wave climatologies presented in this Chapter (Figure 2.3) are an example interpreting the necessary wave climate information, and are a substantial improvement over the largely qualitative work commonly cited in coastal studies in the Hawaii region [Moberly and Chamberlain, 1964].

If wave climate information is to be used to better understand and predict circulation, sediment processes and benthic ecosystem dynamics, then evaluation of existing coastal (shallow water) wave models' ability to accurately predict the propagation of waves into the relatively steeper and more rugose fringing reef embayments from offshore conditions is a prerequisite. The evaluation of the wave model presented here indicates phase-averaged model used (SWAN) appears to be capable of performance similar to that considered acceptable (normalized skill of around 0.8) in more linear, lower-sloped continental margin environments [e.g. Ris et al. 1999;

Sutherland et al. 2004], provided model resolution is fine enough (Figure 2.9). In this study, minimum acceptable spatial resolution (Δx, Δy) was on the order of 40 m and minimum spectral directional resolution ($\Delta\theta$) was 3º. Further increasing spatial and directional resolution continues to improve performance, however refraction continues to be underestimated during events with larger incident wave heights and periods (H_s > 2 m, T_p > 13 s), at least to the limit of spatial resolution tested (Δx, Δy = 10m). The use of unstructured grids (supported by the newest version of SWAN, 40.72) with very high resolution over bathymetrically complex areas was not used in this study but may improve results while keeping computational costs down. Including phase decoupled diffraction [Holthuijsen et al., 2003] also generally improved performance. However, during events with larger incident wave heights and periods (H_s > 2 m, T_p > 13 s), diffraction was poorly estimated or failed to converge.

It is likely that the numerically efficient phase-averaged approach of SWAN does not adequately describe wave evolution over the steep and highly refractive (and potentially diffractive) environment of Hanalei Bay (and perhaps similar fringing reef embayments) under longer wave lengths. Given the relatively low contribution of local wind generation to the wave field within the bay and the importance of refraction and diffraction, a phase-resolving, Boussinesq model such as the one outlined by Madsen et al. [2006] would likely provide superior estimations of wave fields in the bay. However, to model the entire bay using this approach would come at exceptional computational cost due to the requisite space and time resolutions. Despite the shortcomings of the phase-averaged approach, the analysis presented here shows it is capable of estimating the wave field, under most conditions, of highly refractive fringing reef systems with slopes on the order of 0.1 to within the accuracy considered acceptable by other studies of lower sloped environments.

2.5 Acknowledgments

Many thanks to Kathy Presto (USGS) for help with both field work and analyzing/interpreting much of the *in situ* data; Josh Logan (USGS) and Molly Timmers (NOAA/UH) for assisting in field work. Russell Price (NOAA) kindly assisted with optimizing SWAN source code and assisting the computation effort; John Rooney (NOAA/UH) and Jonathon Weiss (NOAA/UH) for collecting multibeam bathymetry to supplement existing LiDAR and multibeam and aggregating the data. Many thanks also to Matt Rosener (Hanalei Watershed Hui) and Carl Berg (formerly Hanalei Watershed Hui) for field support and local knowledge. Thanks to Kevin Wong (NOAA) for support and discussion on content. The constructive comments of Edwin Elias (USGS) on early versions of this manuscript and guidance on numerical modeling issues are greatly appreciated. Mike Field (USGS), Li Erikson (USGS), Rusty Brainard (NOAA), and Peter Vroom (NOAA/UH) all provided reviews and constructive comments on this manuscript. Amanda Toperoff (NOAA/UH) provided excellent assistance in the preparation of figures.

This work was jointly supported by US Geological Survey's Coral Reef Project, NOAA's Coral Reef Conservation Program, and the Australia Institute of Marine Science AIMS@JCU program.

2.6 References

Andrews, J. C., and G. L. Pickard (1990), The physical oceanography of coral-reef systems, in *Coral reefs*, edited by Z. Dubinsky, pp. 11-48, Elsevier, Amsterdam.

Booij, N., R. C. Ris, and L. H. Holthuijsen (1999), A third-generation wave model for coastal regions, Part I, Model description and validation, *J. Geophys. Res.*, *104*(C4), 7649-7666.

Calhoun, R. S., and C. H. Fletcher (1999), Measured and predicted sediment yield from a subtropical, heavy rainfall, steep-sided river basin: Hanalei, Kauai, Hawaiian Islands, *Geomorphology, 30*, 213-226.

Calhoun, R. S., C. H. Fletcher, and J. N. Harney (2002), A budget of marine and terrigenous sediments, Hanalei Bay, Kauai, Hawaiian Islands, *Sedimentary Geology, 150*, 61-87.

Callaghan, D. P., P. Nielsen, N. Cartwright, M. R. Gourlay, and T. E. Baldock (2006), Atoll lagoon flushing forced by waves, *Coastal Engineering*, *53*(8), 691-704.

Coronado, C., J. Candela, R. Iglesias-Prieto, J. Sheinbaum, M. López, and F. J. Ocampo-Torres (2007), On the circulation in the Puerto Morelos fringing reef lagoon, *Coral Reefs*, *26*(1), 149-163.

Dean, R. G., and R. A. Dalrymple (1991), Water Wave Mechanics for Engineers and Scientists, World Scientific, Singapore.

Dollar, S. J. (1982), Wave stress and coral community structure in Hawaii, *Coral Reefs*, *1*(2), 71-81.

Dollar, S. J., and G. W. Tribble (1993), Recurrent storm disturbance and recovery: a long-term study of coral communities in Hawaii, *Coral Reefs*, *12*(3), 223-233.

Draut, A. E., M. H. Bothner, M. E. Field, R. L. Reynolds, S. A. Cochran, J. B. Logan, C. D. Storlazzi, and C. J. Berg (2009), Supply and dispersal of flood sediment from a steep, tropical watershed: Hanalei Bay, Kaua'i, Hawai'i, USA, *Geological Society of America Bulletin*, *121*(3-4), 574-585.

Emery, W., and R. Thomson (2001), *Data Analysis Methods in Physical Oceanography*, 2nd ed., 638 pp., Elsevier Sci, New York.

Fabricius, K. E. (2005), Effects of terrestrial runoff on the ecology of corals and coral reefs: review and synthesis, *Mar. Pollut. Bull.*, *50*(2), 125-146.

Field, M. E., C. S. Berg, and S. A. Cochran (Eds.) (2007), Science and management in the Hanalei watershed; a trans-disciplinary approach, *USGS Open File Rep. 2007-1219*, 92 pp., U.S. Geol. Surv.

Friedlander, A. M., and J. D. Parrish (1997), Fisheries harvest and standing stock in a Hawaiian Bay, *Fisheries Research*, *32*, 33-50.

Friedlander, A. M., and E. K. Brown (2005), Hanalei benthic communities since 1992: spatial and temporal trends in a dynamic Hawaiian coral reef ecosystem, *Technical Report HCSU-003*, 32 pp., Hawai‘i Cooperative Studies Unit, University of Hawaii at Hilo.

Fulton, C. J., and D. R. Bellwood (2005), Wave-induced water motion and the functional implications for coral reef fish assemblages, *Limnol. Oceanogr.*, *50*(1), 255-264.

Gourlay, M. R., and G. Colleter (2005), Wave-generated flow on coral reefs--an analysis for two-dimensional horizontal reef-tops with steep faces, *Coastal Engineering*, *52*(4), 353-387.

Grigg, R. W. (1998), Holocene coral reef accretion in Hawaii: a function of wave exposure and sea level history, *Coral Reefs*, *17*, 263-272.

Hamner, W. M., and E. Wolanski (1988), Hydrodynamic forcing functions and biological processes on coral reefs: a status review, *Proc 6th Int Coral Reef Symp*, *1*(103-113).

Hanson, J. L., B. A. Tracy, H. L. Tolman, and D. Scott (2006), Pacific hindcast performance evaluation of three numerical wave models, *Proceedings: 9th International workshop on Wave Hindcasting and Forecasting*. Victoria, Canada.

Hearn, C., M. Atkinson, and J. Falter (2001), A physical derivation of nutrient-uptake rates in coral reefs: effects of roughness and waves, *Coral Reefs*, *20*(4), 347-356.

Hearn, C. J. (1999), Wave-breaking hydrodynamics within coral reef systems and the effect of changing relative sea level, *J. Geophys. Res.*, *104*(C12), 30,007–030,019.

Hench, J. L., J. J. Leichter, and S. G. Monismith (2008), Episodic circulation and exchange in a wave-driven coral reef and lagoon system, *Limnol. Oceanogr*, *53*(6), 2681-2694.

Holthuijsen, L. H., A. Herman, and N. Booij (2003), Phase-decoupled refraction-diffraction for spectral wave models, *Coastal Engineering*, *49*(4), 291-305.

Jokiel, P. L., E. K. Brown, A. Friedlander, S. K. Rodgers, and W. R. Smith (2004), Hawai‘i Coral Reef Assessment and Monitoring Program: spatial patterns and temporal dynamics in reef coral communities, *Pacific Science*, *58*, 159-174.

Komen, G. J., S. Hasselmann, and K. Hasselmann (1984), On the existence of a fully developed wind-sea spectrum, *J. Phys. Oceanogr.*, *14*, 1271-1285.

Longuet-Higgins, M. S., and R. W. Stewart (1964), Radiation stresses in water waves; a physical discussion, with applications, *Deep Sea Research*, *11,* 529-562.

Lowe, R. J., J. L. Falter, M. D. Bandet, G. Pawlak, M. J. Atkinson, S. G. Monismith, and J. R. Koseff (2005), Spectral wave dissipation over a barrier reef, *J. Geophys. Res.*, *110*, C04001.

Luketina, D. (1998), Simple tidal prism models revisited, *Estuarine, Coastal Shelf Sci.*, *46*(1), 77-84.

Lygre, A., and H. E. Krogstad (1986), Maximum entropy estimation of the directional distribution in ocean wave spectra, *Journal of Physical* Oceanography, 16(12), 2052-2060.

Madin, J. S., and S. R. Connolly (2006), Ecological consequences of major hydrodynamic disturbances on coral reefs, *Nature*, *444*, 477-480.

Madsen, O. S., Y.-K. Poon, and H. C. Graber (1988), Spectral wave attenuation by bottom friction: Theory, *Proceedings of 21th International Conference on Coastal Engineering*, Am. Soc. of Civ. Eng., New York.

Madsen, P. A., D. R. Fuhrman, and B. Wang (2006), A Boussinesq-type method for fully nonlinear waves interacting with a rapidly varying bathymetry, *Coastal Engineering*, 53(5-6), 487-504.

Massel, S. R., and M. R. Gourlay (2000), On the modelling of wave breaking and set-up on coral reefs, *Coastal Engineering*, *39*(1), 1-27.

Moberly, R., and T. Chamberlain (Eds.) (1964), Hawaiian Beach Systems, *Hawai'i Institute of Geophysics Report 64-2*, 42 pp. University of Hawai'i, Honolulu**.**

Monismith, S. G. (2007), Hydrodynamics of coral reefs, *Annu. Rev. Fluid Mech.*, *39*(1), 37-55.

Mulligan, R. P., A. J. Bowen, A. E. Hay, A. J. v. d. Westhuysen, and J. A. Battjes (2008a), Whitecapping and wave field evolution in a coastal bay, *J. Geophys. Res.*, *113*, C03008.

Mulligan, R. P., A. E. Hay, and A. J. Bowen (2008b), Wave-driven circulation in a coastal bay during the landfall of a hurricane, *J. Geophys. Res.*, *113*, C05026.

Munk, W., and M. Sargent (1948), Adjustment of Bikini Atoll to waves, *Transactions, Am. Geo. Union*, *29*(6), 855-860.

National Marine Fisheries Service. (2006). NOAA Ship Hi`ialakai. *Cruise Report No. CR-07-004.* 142pp. Pacific Islands Fisheries Science Center, Honolulu, Hawai`i.

Pawlowicz, R., B. Beardsley, and S. Lentz (2002), Classical tidal harmonic analysis including error estimates in MATLAB using T_TIDE, *Computers & Geosciences*, *28*(8), 929-937.

Polyakov, V., A. Fares, D. Kubo, J. Jacobi, and C. Smith (2007), Evaluation of a non-point source pollution model, AnnAGNPS, in a tropical watershed, *Environmental Modelling & Software*, *22*, 1617-1627.

Ris, R., L. Holthuijsen, and N. Booij (1999), A third-generation wave model for coastal regions: 2. Verification, *J. Geophys. Res.*, *104*, 7667- 7681.

Roger, C. S. (1993), Hurricanes and coral reefs: the intermediate disturbance hypothesis revisited., *Coral Reefs*, *12*(2), 127-138.

Rogers, W. E., J. M. Kaihatu, H. A. H. Petit, N. Booij, and L. H. Holthuijsen (2002), Diffusion reduction in an arbitrary scale third generation wind wave model, *Ocean Engineering*, *29*(11), 1357-1390.

Rooney, J. J. B., and C. H. Fletcher (2005), Shoreline Change and Pacific Climatic Oscillations in Kihei, Maui, Hawaii, *J. Coastal Res.*, *21*(3), 535-547.

Storlazzi, C. D., E. K. Brown, M. E. Field, K. Rodgers, and P. L. Jokiel (2005), A model for wave control on coral breakage and species distribution in the Hawaiian Islands, *Coral Reefs*, *24*(1), 43-55.

Storlazzi, C. D., M. K. Presto, J. B. Logan, and M. E. Field (2006), Coastal Circulation and Sediment Dynamics in Hanalei Bay, Kauai. Part I: Measurements of waves, currents, temperature, salinity and turbidity: June - August, 2005, *USGS Open-File Report 2006-1085*, 35 pp., U.S. Geol. Surv.

Storlazzi, C. D., M. K. Presto, J. B. Logan, and M. E. Field (2008), Coastal circulation and sediment dynamics in Hanalei Bay, Kaua'i, Part IV: Measurements of waves, currents, temperature, salinity, and turbidity, June-September 2006, *USGS Open-File Report 2006-1085*, 29 pp., U.S. Geol. Surv.

Storlazzi, C. D., M. E. Field, M. H. Bothner, M. K. Presto, and A. E. Draut (2009), Sedimentation processes in a coral reef embayment: Hanalei Bay, Kauai, *Marine Geology*, *264* (3-4), 140–151.

Sutherland, J., A. H. Peet, and R. L. Soulsby (2004), Evaluating the performance of morphological models, *Coastal Engineering*, *51*(8-9), 917-939.

Tait, R. J. (1972), Wave set-up on coral reefs, *J. Geophys. Res.*, *77*(12), 2207-2211.

Tolman, H. L. (2002), *User manual and system documentation of WAVEWATCH-III version 2.22*, 133 pp, NOAA/NCEP, Washington, DC.

von Arx, W. S. (1948), The circulation systems of Bikini and Rongelap lagoons, *Eos Trans. AGU*, *29*, 861-870.

Willmott, C. J., R. E. Davis, J. J. Feddema, K. M. Klink, D. R. Legates, C. M. Rowe, S. G. Ackleson, and J. O'Donnell (1985), Statistics for the evaluation and comparison of models, *J. Geophys. Res.*, *90*(C12), 8995-9005.

Wolanski, E., R. H. Richmond, G. Davis, and V. Bonito (2003), Water and fine sediment dynamics in transient river plumes in a small, reef-fringed bay, Guam, *Estuarine, Coastal Shelf Sci.*, *56*(5-6), 1029-1040.

3. Hydrodynamics of a fringing coral reef embayment: circulation, flushing times, and implications for water quality and sediment transport

Ron Hoeke[1,2], Curt Storlazzi[3], and Peter Ridd[2]

1. Joint Institute for Marine and Atmospheric Research (JIMAR)
   University of Hawaii and NOAA Pacific Islands Fisheries Science Center
   Honolulu, Hawaii, USA

2. School of Engineering and Physics
   James Cook University
   Townsville, Queensland, Australia

3. Coastal and Marine Geology Program
   US Geological Survey
   Santa Cruz, California, USA

Abstract

A coupled wave-flow numerical model of Hanalei Bay, Hawaii, was constructed to investigate controls on circulation and flushing times of a bathymetrically-complex embayment lined with coral reefs. The bay is exposed to large waves and river floods several times per annum. The model was calibrated using two periods of available *in situ* data highly representative of the two conditions which dominate the area's wave climate: one associated with local trade winds and trade-wind waves, and the other with distant-source episodic large swells. Model comparison with the *in situ* data was greatly improved by the use of spatially-varying hydraulic roughness and by making the value of the semi-empirical wave-breaking parameter dependent on incident wave steepness and reef slope. During trade-wind conditions, overall circulation was primarily wind-driven; the volume flux-based flushing of the bay was calculated to be on the order of 35 hours. Under the episodic large-swell condition, circulation was strongly dominated by wave-driven flows and flushing times dropped to as little as 2 hours. The vigorous hydrodynamics, particularly the development of an offshore-directed jet in the central part of the bay, occurring during the upper 10% most energetic swell conditions, indicate that only a few (0-10) of events each year are likely capable of significant sediment export from the bay. Like many fringing reef areas backed by steep-sided watersheds, Hanalei Bay receives high episodic fluvial sediment load during a similarly low number of flood

events. The low frequency, but decoupled nature of episodic sediment delivery and the subsequent removal processes identified here suggest that the water quality and sedimentary environment of Hanalei Bay is sensitive to changes in storm tracks, which are predicted to occur under most climate change scenarios, and may lead to large changes on timescales of years to decades. This sensitivity likely extends to many other fringing reefs systems neighboring steep-sided watersheds, a common morphology on tropical and sub-tropical high islands world-wide.

3.1. Introduction

Hydrodynamics control many ecological aspects of reef systems, such as the fate of pollutants, the distribution of organisms, nutrient uptake, overall productivity, dispersal and recruitment of larvae, patterns of coral bleaching, and degree of disturbance due to episodic storms [*Andrews and Pickard*, 1990; *Dollar*, 1982; *Grigg*, 1998; *Hamner and Wolanski*, 1988; *Hearn et al.*, 2001; *Kraines et al.*, 1998; *Madin and Connolly*, 2006; *Roger*, 1993]. The importance of surface gravity waves to reef hydrodynamics was identified in early work [*Munk and Sargent*, 1948; *von Arx*, 1948], and more recent studies have highlighted their dominant contribution for many different reef morphologies (e.g. see *Callaghan et al.*, 2006; *Coronado et al.*, 2007; *Hench et al.*, 2008). Additionally, the distribution of wave-generated bed shear stresses is a pivotal factor in determining benthic community composition (e.g. see *Dollar*, 1982; *Fulton and Bellwood*, 2005; *Roger*, 1993; *Storlazzi et al.*, 2005). While the mean increase in water elevation (setup) and associated barotropic mean flows resulting from the dissipation of wave energy (radiation stress gradient, *Longuet-Higgins and Stewart*, 1964; *Tait*, 1972) is conceptually easy to understand, its parameterization and prediction over steep and morphologically complex coral reefs has proven problematic [*Gourlay and Colleter*, 2005; *Hearn*, 1999]. This study examines the circulation of a semi-enclosed bay with fringing coral reefs exposed to a broad range of incident surface gravity wave energy, with special attention to currents driven by gradients in radiation stress. The relative contribution of the incident wave field to overall flushing rates and near-bed shear stresses are compared to contributions of from winds, tides, and buoyancy forcing.

The study site, Hanalei Bay on the Hawaiian Island of Kauai (Figure 3.1), receives a high episodic sediment load from adjoining (steep-sided) watersheds

[*Calhoun and Fletcher*, 1999; *Polyakov et al.*, 2007]. Such sedimentation has the potential to significantly impact reef ecosystems and has been implicated in the major ecological degradation of a number of them [*Fabricius*, 2005; *Wolanski et al.*, 2003]. Past studies show evidence that complex bed shear stresses due waves and wave driven flows frequently (re)suspend and transport sediment locally within the bay [*Calhoun et al.*, 2002; *Storlazzi et al.*, 2009], but that infrequent episodic wave events are likely the only effective means of removing fluvial sediments from the bay [*Calhoun et al.*, 2002; *Draut et al.*, 2009; *Storlazzi et al.*, 2009]. The wave climatology presented in Chapter 2 has shown that two classifications, one characterized as modal and the other as episodic, describe conditions within the bay more than 80% of the time. The modal classification is associated with local trade winds, and is typified by nearshore wave heights of approximately 0.5m, and occurs approximately 80% of the time. The episodic classification occurs less than 10% of the time, and is associated with long period (12 – 25 s) swells generated by relatively distant storms to the northwest. During these episodes 1-5 m nearshore wave heights are the norm. Conditions falling outside of these two classifications are generally much more quiescent.

In this study, two one-week periods, one characteristic of trade-wind wave (TWW) conditions and the other encompassing a typical north-west swell (NWS) episode, were selected to for more detailed investigation. This more detailed investigation's goal is to better elucidate the dominant hydrodynamic processes in the bay under the two different conditions. *In situ* observations and a coupled wave/flow model are utilized in an effort to gain insight on (1) the relative contributions of winds, tides, buoyancy flows, and waves to overall circulation; (2) the residence time (flushing) under these two conditions (3) how well existing physical parameterizations predict circulation; and (4) the distributions of bed shear stresses under these two conditions. Qualitative estimates of the distribution and flushing of terrigenous materials and water quality under different conditions suggest that fluvial materials are only effectively removed from the bay by the episodic large wave events.

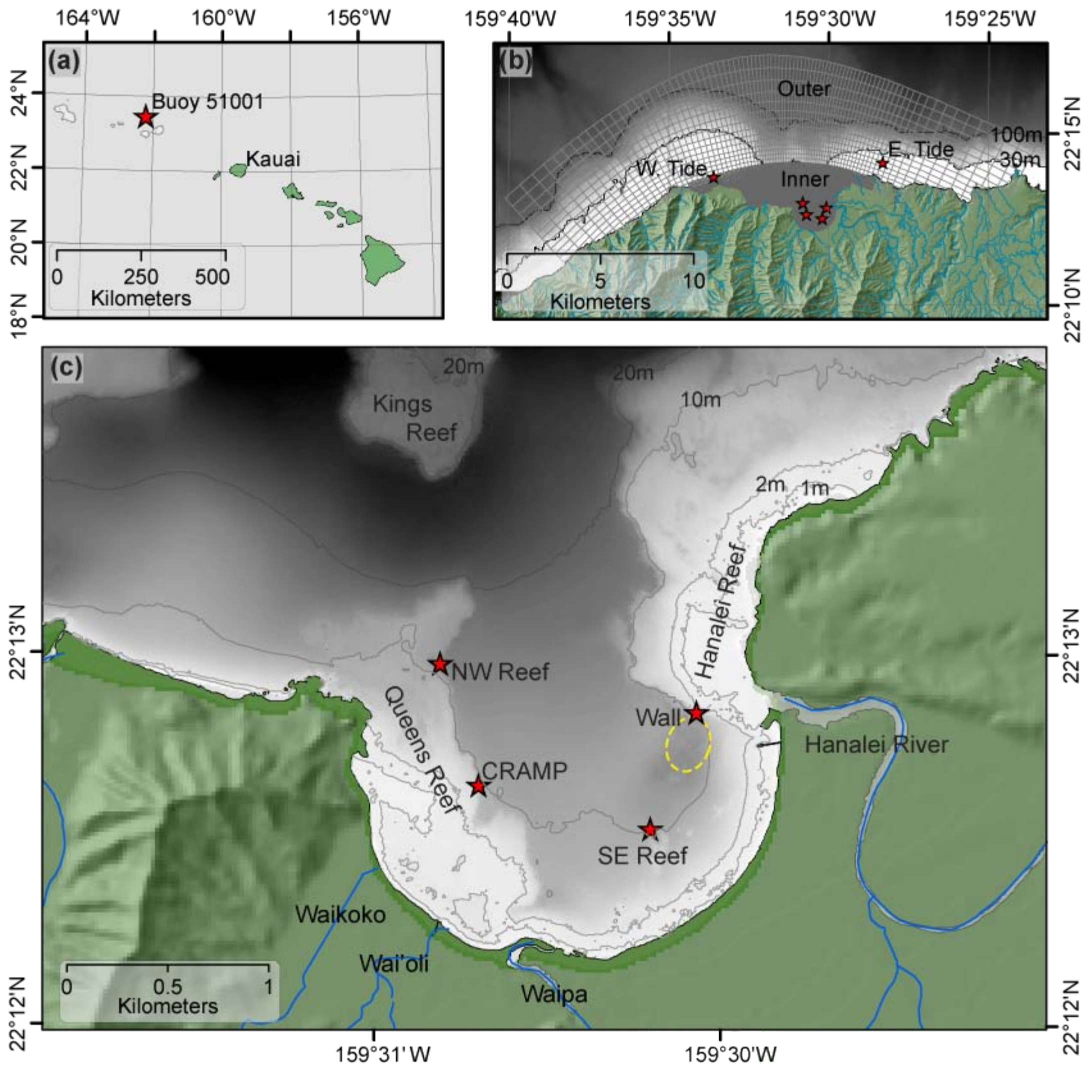

Figure 3.1: Study site: (a) Hawaiian Archipelago with the position of NOAA NDBC Buoy 1 indicated the island of Kauai indicated. (b) North Coast of Kauai, with Hanalei Bay at the center; the inner and outer modeling domain grids are indicated, as are the 30 m and 100 m contours. E. Tide and W. Tide indicate the location of pressure (tidal elevation) observations. (c) Hanalei Bay; the Wall, SE Reef, CRAMP, and NW Reef mooring site positions and bathymetric contours indicated; the mouth of Hanalei River is on the east side of the bay and the Waipa, Wai'ole, and Waikoko streams are indicated. The 'Black Hole', outlined with a dotted yellow line, is just south of the Wall Site.

3.2. Study Area

Kauai (22.2°N, 159.5°W) is a subtropical high island of volcanic origin lying in the North Pacific trade wind belt. Tides in the area are of a mixed microtidal regime, with neap ranges of around 0.4 m and spring ranges around 0.9 m [*Storlazzi et al.*, 2009]. Trade winds associated with the North Pacific subtropical anticyclone prevail; these winds are typically around 5-12 m·s^{-1} and generate wind waves (TWW) generally 1-3 m in height with 6-10 s periods from the east to northeast [*Chapter 2*; *Moberly and Chamberlain*, 1964]. Trade winds occur throughout the year, but are most prevalent during the spring and summer months. Hanalei Bay, approximately 2 km wide, is located on the island's north side and faces roughly north-northwest (Figure 3.1b). This makes it partially sheltered from TWW conditions, but exposed to seasonally high episodic swell events between October and May. These swells are usually generated from remote sources to the north and west, with 1-5 m waves and 12-20 s periods common during these months; wave heights in excess of 6 m may occur several times a year. During these swell events, winds typically slacken or become westerly and rotate clockwise back to the northeast, as cyclonic low pressure systems producing the swell pass to the north, although this is not always the case. Tropical and extra-tropical cyclones (the latter known as 'Kona' storms) also occasionally impact the island; these, however, usually most effect the south and west sides of the island.

Fringing reef platforms are found on the east and west sides of the bay; the western ('Queen's Reef') generally has a more gradual reef slope (~6-12°) and deeper reef flat (~1-4 m), while the eastern side ('Hanalei Reef') is somewhat steeper (reef slope of 10° to 30° or more) and has an extensive area of reef flat less then 1 m deep. A detached deeper reef ('King's Reef') lies approximately 1 km offshore, coming up to depths of 16 m. This offshore reef affects incident gravity wave refraction patterns and has been known to break when waves exceed 5 m. These reefs are composed primarily of coralline alga, with live coral cover ranging between 2 and 47%, with an average of about 18%; *Montipora* sp. dominates this coverage [*Friedlander and Brown*, 2005]. Most other areas in the bay tend to be flat or gently sloping sand or gravel, and mostly carbonate in composition, especially at shallower depths [*Calhoun et al.*, 2002]. A notable exception is the 'Black Hole', a 2-5 m deep depression at a depth of 12-15 m west and south of the mouth of the Hanalei River, where terrestrial material (siliciclastic and organic) forms a large fraction [*Calhoun et al.*, 2002; *Draut et al.*, 2009; *Storlazzi et al.*, 2009]; it appears terrestrial materials are also often deposited in other areas of the bay during river floods and subsequently re-suspended and advected during later wave events [*Draut et al.*, 2009].

Hanalei and the surrounding coasts are backed by Mount Wai'ale'ale (elevation 1570 m), often identified as the 'wettest place on earth' with yearly rainfall totals at a rain gauge on the slopes averaging between 9-10 m [*Calhoun and Fletcher*, 1999; *Polyakov et al.*, 2007]. The largest of the associated watersheds' many streams is the aforementioned Hanalei River, which empties on the northeast side of the bay, has an average outflow of 5.7 m^3/s, but has reached 1274 m^3/s during periods of heavy rainfall. The river delivers an estimated annual fluvial sediment load of 1.76×10^4 Mg [*Calhoun and Fletcher*, 1999]. Other (as yet un-quantified) fluvial inputs to the bay include the Waipa, Wai'oli, and Waikoko streams (Figure 3.1).

Agriculture and the spread of invasive plant and animal species appear to be increasing sediment loads [*Draut et al.*, 2009; *Polyakov et al.*, 2007]; it is one of the three priority watersheds in Hawaii identified for focused action to address land-based pollution threats to coral reefs by the U.S. Coral Reef Task Force. These issues have prompted a number of studies in the area (e.g. *Calhoun et al.*, 2002; *Friedlander and Parrish*, 1997; *Friedlander and Brown*, 2005; more recent studies are summarized by *Field et al.*, 2007).

3.3. *In situ* Observations

Acoustic Doppler current profilers (ADCP) with pressure sensors were deployed at four different locations within the bay; additional pressure sensors were deployed approximately 4 km on either side of the bay to assess tidal wave propagation along the coast. The details of these instrument platforms are given in Table 3.1; their locations are plotted in Figure 3.1b and 1c.

Table 3.1 Instruments deployed in or near Hanalei Bay for this study. Deployments depths (*h*) and dates are given; for deployment locations, refer to Figure 3.1b and 3.1c.

Site	Instrument	h(m)	dates
Wall	RD Instruments ADCP (600 kHz) Seabird SBE-37SM (conductivity and temp.)	10.0	July 7, 2006 – April 24, 2007
NW Reef	Sontek ADCP (1 MHz) SBE-37SM (conductivity and temp.)	14.5	Sep14, 2006 – April 24, 2007
CRAMP	Nortek ADCP (1 MHz)	9.7	June 7, 2006 – Sept. 7, 2006
SC Reef	Nortek ADCP (1 MHz)	10.5	June 7, 2006 – Sept. 7, 2006
E Tide	Seabird SBE26+ (pressure sensor)	8.0	April 22, 2007 – Sept. 22, 2007
W Tide	Seabird SBE26+(pressure sensor)	3.5	April 22, 2007 – Sept. 22, 2007

While the ADCP deployments provided measurements of water column velocity profiles, waves, and water levels (at hourly intervals) during their entire period of deployment (Table 3.1), this study will primarily focus on detailed observations at the Wall and CRAMP site during the week of August 2-7, 2006 (the TWW period) and observations at the Wall and NW Reef site during the week of Jan 20-27, 2007 (the NWS period). These two periods are highly representative of the two characteristic conditions (TWW and NWS), based on the analysis of the entire dataset [*Chapter 2*; *Storlazzi et al.*, 2009].

A number of agencies provide monitoring of environmental variables in the area; those utilized in this study are discussed below. The National Oceanographic and Atmospheric Administration's (NOAA) National Data Buoy Center (NDBC) Buoy 1, 314 km northwest of Kauai in 3430 m of water (Figure 3.1a), provides hourly estimates of directional wave spectra and associated bulk wave parameters as well as measurements of wind speed and wind direction (http://www.ndbc.noaa.gov). This buoy is henceforth referred to as Buoy 1. While some distance from the study site, the buoy measurements can be considered representative of wave climate immediately offshore from the study site [*Chapter 2*]. The US Geological Survey (USGS) Pacific Islands Water Science Center Gauging Station 16103000, 8.2 km up the Hanalei River from the bay, provided hourly measurements of water discharge rate and suspended sediment load (http://hi.water.usgs.gov).

3.4. Numerical Modeling

The Delft3D modeling system, a coupled flow/wave numerical solution designed for coastal applications, was selected for use in this study [*Lesser et al.*, 2004; *Roelvink and Banning*, 1994]. The flow module utilizes a finite-difference solution to the Navier-Stokes equations for unsteady flow on a three-dimensional (sigma coordinate system) curvilinear grid; the wave module is the SWAN model, a phase-averaged solution of the discrete spectral balance of wave action density [*Booij et al*., 1999; *Ris et al*., 1999]. The forces resulting from total wave dissipation, as described by *Dingemans et al.* [1987], are incorporated as additional surface stresses in the flow module. The two modules are iteratively coupled so wave information from the wave module is passed to the flow module to compute mass transport by wave forces and Stokes drift, the subsequent water levels and currents are passed back to the wave module for use in calculating an updated wave field, and so on.

Although this modeling system was developed for use on low-slope sedimentary coastlines, it has been applied with some success to steeper erosional coasts (e.g. *Mulligan et al.*, 2008; *Vitousek et al.*, 2007), although generally not coral reef areas with slopes approaching 30%, such as Hanalei Bay. Application of this modeling system to Hanalei Bay was an iterative process, with grid design, forcing input, and parameterization evolving as model output comparisons with *in situ* observations and geological evidence [*Calhoun et al.*, 2002; *Draut et al.*, 2009; *Storlazzi et al.*, 2009] improved. A summary of model development is presented below.

3.4.1 Computational grid, boundary design, and model application

Comparison of early model runs with *in situ* and qualitative observations demonstrated the importance of (1) longshore processes and (2) edge boundary effects such as unrealistic locally strong wave driven flows near the edge of the boundary due to dissipation of wave boundary conditions over shallow bathymetry in the model. This forced the extension of the lateral boundaries of the flow computational grid out to approximately 12km either side of Hanalei Bay, resulting in a lateral (~east/west) extent of over 26 km. To correctly account for wave refraction effects, it was necessary to extend the offshore boundary out to the maximum offshore excursion of the 100 m depth contour, approximately 8 km north of the mouth of the bay (Figure 3.1b). To minimize interpolation errors and edge effects, wave computations were performed on the same grid, except offshore and lateral boundaries were extended a further two grid cells to reduce the aforementioned wave edge boundary effects. To keep computational costs down, the grid was divided into an outer domain, with grid cell resolution on the order of 800 m at the edges and 200 m near the center, and an inner domain, around the area of interest, with a grid cell resolution of approximately 50 m along the inner/outer boundary and 25 m near the shoreward edge of the bay (Figure 3.1b); spatial resolution of this scale is necessary to resolve hydrodynamic features of interest [*Chapter 2*]. The model runs were performed using domain decomposition (two-way communication between inner and outer grids). All model runs defined the outer grid as depth integrated (2D); the inner domain was run in both 2D mode and with multiple depth layers (3D). For 3D model runs, 13 sigma layers were used; layer thickness, from surface to bottom, were defined by the following percentages of water depth: 2%, 3%, 5%, 7%, 10%, 15%, 20%, 14%, 9%, 6%, 4%, 3%, and 2%. The model application appeared to be insensitive to different values of horizontal eddy viscosity between 0.1 and 1 $m^2 s^{-1}$; a value of 0.5 $m^2 s^{-1}$ was used for all run discussed here. [*Lowe et al.*, 2009b] found a similar lack of sensitivity and used similar values. Bottom boundary roughness was computed using the White-Colebrook formulation for the outer (2D) domain and the z_0 formulation for the inner (3D) domain.

For the offshore and lateral boundaries, harmonic analysis [*Pawlowicz et al.*, 2002] was performed on the two pressure sensors deployed on either side of the bay (Table 3.1, Figure 3.1b); the resulting (astronomic) tidal constituents (frequency, amplitude, and phase) with SNR greater than 10 were selected; resulted in the six constituents: M2, S2, O1, K1, N2, and SK3 (Table 3.2). Water levels at the east and west corners of the outer grid were assumed to be a linear function of the difference between each constituent's amplitude and phase at the two pressure sensors: the values were linearly adjusted by the ratio of the distance between the lateral (east/west) boundaries and the sensor locations distance apart. Water levels at both corners of the offshore boundary were then forced with the resulting astronomic amplitudes, frequencies, and phases. The lateral boundaries were calculated as water-level gradients (Neumann boundary conditions). This forces the component tidal waves to propagate along the offshore boundary while allowing water levels and current fields to adjust to both the offshore boundary water levels and other (wind and wave) forcing input at the lateral boundaries [*Roelvink and Wasltra*, 2004].

Table 3.2: Tidal constituent amplitudes and phases calculated from water elevations measured at the deployed on either side of the bay (Table1, Figure 3.1b).

	E Tide		W Tide	
Astronomic constituent	**Amplitude (m)**	**Phase (degrees)**	**Amplitude (m)**	**Phase (degrees)**
*K1	0.1751	234.37	0.1855	231.45
*M2	0.1394	4.77	0.1341	3.63
*O1	0.0902	218.30	0.0909	215.88
*S2	0.0503	6.05	0.0502	11.55
*N2	0.0253	355.52	0.0241	351.14
*SK3	0.0029	196.47	0.0032	205.35

Model bathymetry was interpolated from two different sources: LiDAR data provided by the US Army Corps of Engineers (http://shoals.sam.usace.army.mil/) in shallower areas and multi-beam acoustics provided by University of Hawaii Benthic

Habitat Mapping Center (http://www.soest.hawaii.edu/pibhmc/) in deeper areas. In almost all cases, bathymetric data resolution was higher than computation grid cell resolution; grid bathymetric errors due to interpolation in data poor areas are considered insignificant. Over the course of model testing, hydraulic roughness proved important to both overall magnitude and structure of flow patterns. To address this, areas of reef/hardbottom and unconsolidated sediment (sand) were identified and digitized through a combination of bathymetric slope analysis and visual inspection of aerial photography and IKONOS and Quickbird satellite imagery. The resulting 'reef' or 'sand' areas were assigned different hydraulic roughness values depending on (bottom) boundary layer formulation and calibration with ADCP data. This resulted in spatially varying roughness grids for both flow and wave module computations in addition to bathymetry grids. Values in the reef and other (sand) areas were varied for model validation (see section 3.5.2.1).

3.4.2 Wind and Wave Input

Wave forcing was provided by a coarse-resolution, non-stationary third-order Stelling/Leendertse propagation SWAN model driven by directional spectra and winds measured at Buoy 1. This input model, including validation, is discussed in more detail in Chapter 2. Wave spectra from this course resolution input model were linearly interpolated along the Hanalei offshore wave (outer) grid boundary.

The 10 m height wind fields from an experimental high-resolution (horizontal resolution ~0.8 km) atmospheric model were provided at 3 hour time steps by the University of Hawai'i Asia Pacific Data Research Center (http://apdrc.soest.hawaii.edu, *Yang and Chen*, 2008). These gridded fields were spatially interpolated to the (inner and outer) flow and wave computational grids, and temporally interpolated to the flow module's time steps. The model then appeared (at least qualitatively) to capture flow structures observed during strong trade-wind, low wave conditions.

3.4.3 Wave dissipation

Wave energy dissipation not only produces momentum flux (radiation stress) driving currents, waves and current motions also together modify vertical mixing and near-bed boundary layers in a non-linear fashion [*Grant and Madsen*, 1979]. Thus, optimized estimation of wave dissipation and bed shear stress enhancement by the combined effects of waves and currents is requisite for realistic modeling of wave-dominated Hanalei Bay.

On most coral reefs, it can be assumed that wave energy dissipation is dominated by two processes: bottom friction and wave breaking [*Lowe et al.*, 2005; *Massel and Gourlay*, 2000], so that the change in energy flux (EC_g), the product of wave energy (E) and group celerity (C_g), i.e. wave power [*Dean and Dalrymple*, 1984], can be described (in one dimension) as:

$$\frac{\partial(EC_g)}{\partial x} = -\varepsilon_b - \varepsilon_f \qquad [1]$$

where ε_b and ε_f are rates of dissipation due to breaking and friction, respectively.

The formulation of [*Madsen et al.*, 1988] was used to provide an estimate of ε_f:

$$\varepsilon_f = \frac{1}{4}\rho f_w u_{b,r} u_b{}^2 \qquad [2]$$

Where u_b is the near-bed maximum horizontal orbital velocity and $u_{b,r}$ is a 'representative' maximum near-bed orbital velocity (taken to be the root-mean-square of the u_b of each spectral component of the wave field); the 'friction wave factor' (f_w) is defined by the hydraulic roughness length (k_w); for definitions of these terms and extension to spectral formulation, see [*Lowe et al.*, 2005; *Madsen et al.*, 1988]. The analysis presented in Chapter 2 showed that values of k_w on the order of 0.01 m and 0.10 m for sand and reef areas, respectively, optimize SWAN estimates of frictional dissipation in Hanalei Bay; these values of k_w for the reef areas are comparable to those found in other coral reef studies (e.g. *Hearn*, 1999; *Lowe et al.*, 2005).

Energy dissipation due to breaking (ε_b) is estimated using the periodic bore model of [*Battjes and Janssen*, 1978]:

$$\varepsilon_b = \frac{1}{4}\alpha Q \frac{\omega}{2\pi}\rho g H_m{}^2 \qquad [3]$$

where α is a proportionality constant of dissipation and Q_b is the fraction of waves breaking (determined from a cut-off Raleigh distribution, see [*Thornton and Guza*, 1983] for a discussion; see [*Booij et al.*, 1999] for application in SWAN). The maximum allowable wave height in shallow water, defining wave breaking, is given by:

$$H_m = \gamma_b h \quad [4]$$

where γ_b is an empirical "breaker height coefficient" that defines the maximum allowable wave height (H_m), and thus the initiation (or cessation) of breaking. These two empirical coefficients, α and γ_b, have been fairly well studied in low slope, sandy environments (|dh/dx|<<0.1) and are generally taken to have values of α =1 and γ_b = 0.6 -0.8 (e.g. [*Battjes and Stive*, 1985; *Kaminsky and Kraus*, 1993]). *Lowe et al.* [2009b] found an optimal value of γ_b = 0.64 for a coral reef area (Kaneohe Bay, Hawaii), but seaward reef slope in that study area is low (average: 0.016), similar to many sandy shorelines. *Massel and Gourlay* [2000] suggest that such values may not be applicable to the steeper slopes ($|dh/dx| \approx 0.2$) typical of coral reefs such as those found in Hanalei Bay, where reef slopes are between 0.02-0.5, generally averaging about 0.1 in wave exposed areas.

It was thus necessary to evaluate values of α and γ_b for optimal estimation of ε_b in the model. Unfortunately, the bay's complex fringing reef topography and exceptionally high wave episodic wave heights precluded direct observations of ε_b. Instead, an observed (empirical) relationship between incident EC_g and the principle axis current magnitude at the Wall site, based on the full 10 month *in situ* timeseries (r^2 = 0.92, described in Chapter 2), was used to optimize the parameterization of ε_b. This made it necessary to simultaneously consider different parameterizations of the wave-current boundary layer interaction [Soulsby et al., 1993], as this too affected wave-induced current velocities.

A model sub-domain, encompassing most of the bay out to the offshore limit of Kings Reef, was constructed and run in 2D-mode with no wind forcing or river input. Bulk deepwater wave parameters (H_s, T_p, and θ_p) were varied (between 1 - 5 m, 7 – 18 s, and 315 - 30°, respectively) along the offshore boundary while water levels were varied ±0.4 m at the M2 tidal frequency for 40 cycles. Consecutive runs with these same boundary conditions were used to evaluate different values of α, γ_b, and methods of calculating wave-current bed shear stress enhancement. Normalized residuals were calculated from the difference between the principle axis current magnitudes at the Wall site; i.e. ($|U_{p,m}|-|U_{p,o}|)/|U_{p,o}|$, where $|U_{p,m}|$ is the (principle axis) current magnitude calculated by the model and $|U_{p,o}|$ is the current magnitude predicted by the observed relationship with incident EC_g. The parameters γ_b, α, and

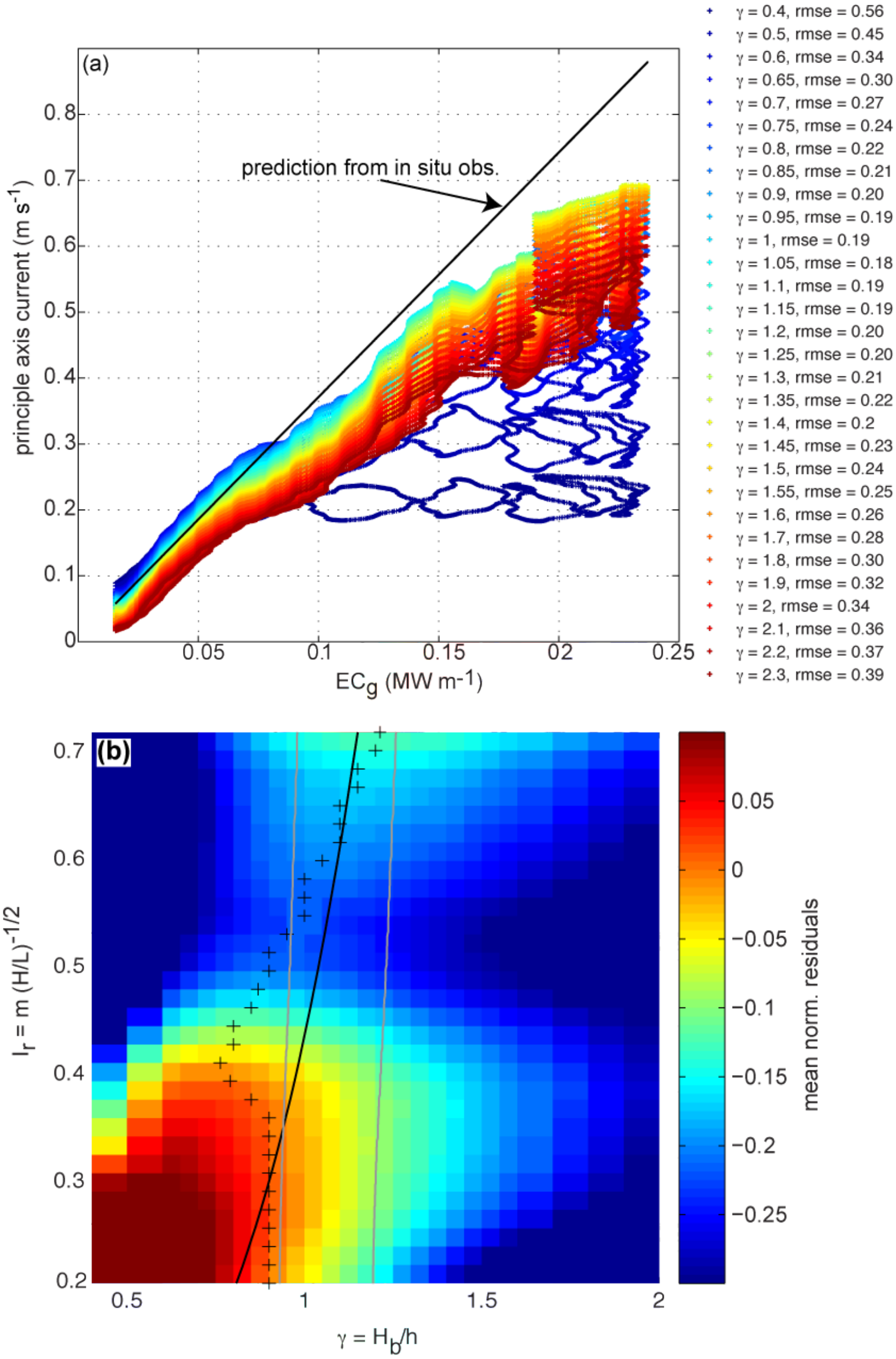

Figure 3.2: (a) Principle axis current magnitude at the Wall Site ($|U_{p,o}|$), predicted from incident unit energy flux (EC_g), based on 10 months of *in situ* observations (black line, $r^2 = 0.92$, Chapter 2) and modeled Wall Site principle axis current magnitudes ($|U_{p,m}|$) using different values of the breaker height coefficient (γ_b), calculated while varying offshore wave conditions; RMSE associated with each γ_b value are the root mean square of the normalized residuals [i.e. ($|U_{p,m}|$-$|U_{p,o}|$)/$|U_{p,o}|$]. (b) Mean normalized residuals for binned values of the "surf similarity" or Iribarren (I_r) parameter [*Battjes*, 1974]. Minimum residuals associated with values of γ_b are represented with black crosses in the best fit for Equation 5 (see text) is given with a solid black line; minimum and maximum values for γ_b suggested by [*Massel and Gourlay*, 2000] for corresponding (offshore) wave conditions and reef slopes are plotted in with grey lines. Note modeled currents begin to be consistently under-estimated at I_r>0.4, considered near the transition between spilling and plunging breakers [*Battjes*, 1974].

the combined wave-current bed shear stress method were considered optimized when the residual values were minimized.

Model sensitivity was low for the range of α values considered physically meaningful (0.8 – 1.5) and the different wave-current bed shear calculation methods. An α value of 1 and the wave-current bed shear enhancement method of [*O'Connor and Yoo*, 1988] were considered optimized and are used in all further discussions.

Model sensitivity was much higher to changes in γ_b; model performance was generally far poorer for the more accepted range of γ_b (0.6 – 0.8) than for the higher values (~1) suggested by [*Massel and Gourlay*, 2000] (Figure 3.2). However, no single value of γ_b was optimal; best performing values of γ_b varied with incident EC_g and deepwater wave steepness (H_0/L_0) (Figure 3.2a,b). The model consistently under predicted $|U_{p,m}|$ when EC_g was greater than 0.12 $MW \cdot m^{-1}$; reducing bed roughness values lead to far greater over-prediction of $|U_{p,m}|$ in low wave conditions and thus worse overall model performance. The dependence of γ_b on H_0/L_0 and bottom slope has noted before ([*Massel and Gourlay*, 2000], [*Kaminsky and Kraus*, 1993], [*Battjes*, 1974], and others), and generally given the form of:

$$\gamma_b = a(I_r)^b \qquad [5]$$

where a and b are empirical coefficients and I_r is the "surf similarity" or Iribarren (I_r) number [*Battjes*, 1974]:

$$I_r = \left|\frac{dh}{dx}\right|\left(\frac{H_0}{L_0}\right)^{-\frac{1}{2}} \qquad [6]$$

Using wave conditions at the offshore boundary for values of H_0 and L_0 and the average slope of the Hanalei forereef for $|dh/dx|$, a best fit of minimum normalized residual values was found when a=0.975 and b = -0.121, leading to values of 0.9 – 1.2 for γ_b. It is not supposed that these coefficients are necessarily physically meaningful, more likely they happen to compensate for the inherent assumptions of the periodic bore model and estimation of wave forces, which are likely unrealistic for plunging breakers and relatively steep slopes that typify the study area. Utilizing the empirical relationship to estimate γ_b with changing wave conditions improves model performance. Subsequent model runs calculate values of γ_b based on changing values of I_r, as described above, over the course of each model run.

3.5 Results

3.5.1 In situ observations

During the TWW period, offshore H_s, as measured by Buoy 1, gradually varied between approximately 2 – 3m, with T_p between 6 – 10 s, and θ_p centered closely on 90°; winds were dominated by northeasterly trades of ~10 m·s^{-1} (Figure 3.3a – c). Measured H_s the exposed CRAMP site (Figure 3.3a) remained below 0.6 m for the entire period. Conversely, during the NWS period, Buoy 1 measured an

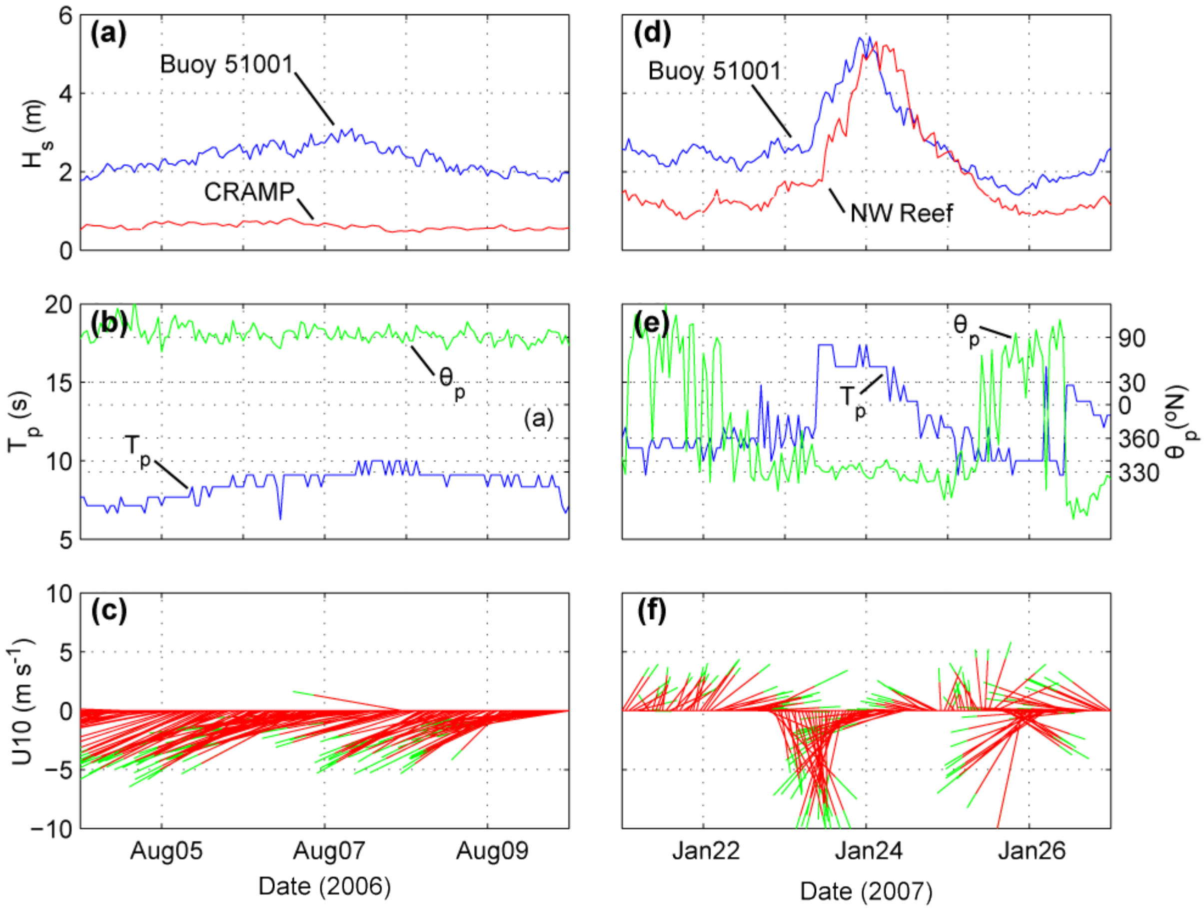

Figure 3.3: Comparison of bulk wave parameters and winds measured by Buoy 1 during two one-week periods, one defined as the trade wind period [Aug. 4 - 11, 2006, (a-c)] and the other as the NW swell period [Jan. 21-28, 2007, (d-f)]. Trade wind period (a) significant wave height (Hs), (b) peak period (Tp) and peak direction (θp), and (c) wind vectors; NW swell period (d) Hs, (e) Tp and θp, and (f) wind vectors.

abrupt increase in H_s from approximately 2 m on January 23 to a peak of 5.5 m on January 24. This increase in wave height was accompanied by an increase in T_p from 11 s to 17 s and a change in θ_p from 90° to 330° (Figure 3.3d – f). H_s and T_p then declined until around Jan 26, when a second less energetic NWS episode occurred.Winds rotated clockwise from the southwest to the east, following the west-to-east passage of the temperate cyclone, associated with the NWS, to the north. The exposure of the bay to this swell is apparent, as H_s measured at the NW Reef site approached 5.5 m, closely following offshore H_s when θ_p was approximately 330°.

Water levels, currents, and wave heights at the Wall site during the TWW and NWS periods are compared in Figure 3.4. During the TWW period, currents were relatively weak (<0.07 m·s-1), oscillating roughly on and off the neighboring reef platform (Figure 3.4a – b); during the NWS period, a strong surface flow (up to 0.6 m·s^{-1}),

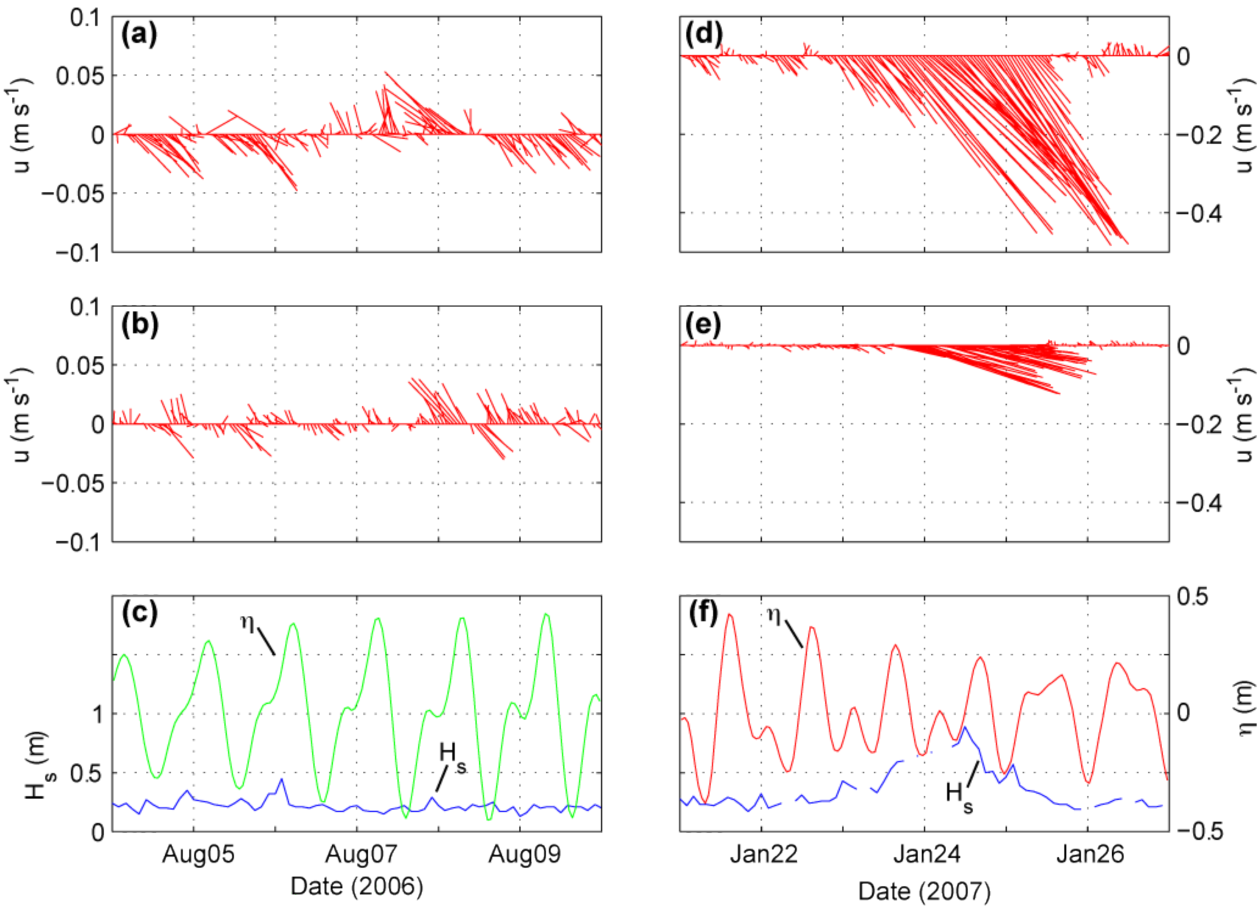

Figure 3.4: Comparison of conditions at the Wall site during the trade wind and NW swell periods: trade wind period (a) near surface and (b) near-bottom current vectors and (c) water levels (η) and H_s ; NW swell period (d) near surface and (e) near bottom current vectors and (f) η and H_s. Note the different scaling of current vectors in (a, b) vs. (d, e).

directed off the reef platform, developed (Figure 3.4d). This flow extended to near the bottom, although it decreased with depth and appeared to be steered more parallel with the near-vertical neighboring fore-reef (Figure 3.4e). The current magnitude at the Wall site is closely linked to incident wave energy flux within the bay [*Chapter 2*]. The Wall site itself is highly sheltered from this incident energy: wave heights remained below 0.4 m during the TWW period (Figure 3.4c) and well below 1.0 m during the NWS period (Figure 3.4f), despite measured wave heights of up to

5.5 m on the western side of the bay during the NWS period (Figure 3.3d, 3.5f).

Water levels and currents at the more exposed CRAMP and NW Reef sites during the TWW and NWS periods, respectively, are compared in Figure 3.5. During the TWW period, currents were stratified; near-surface flows appeared to be dominated by trade winds, with magnitudes of 0.1 – 0.2 m·s^{-1}, while weak near-

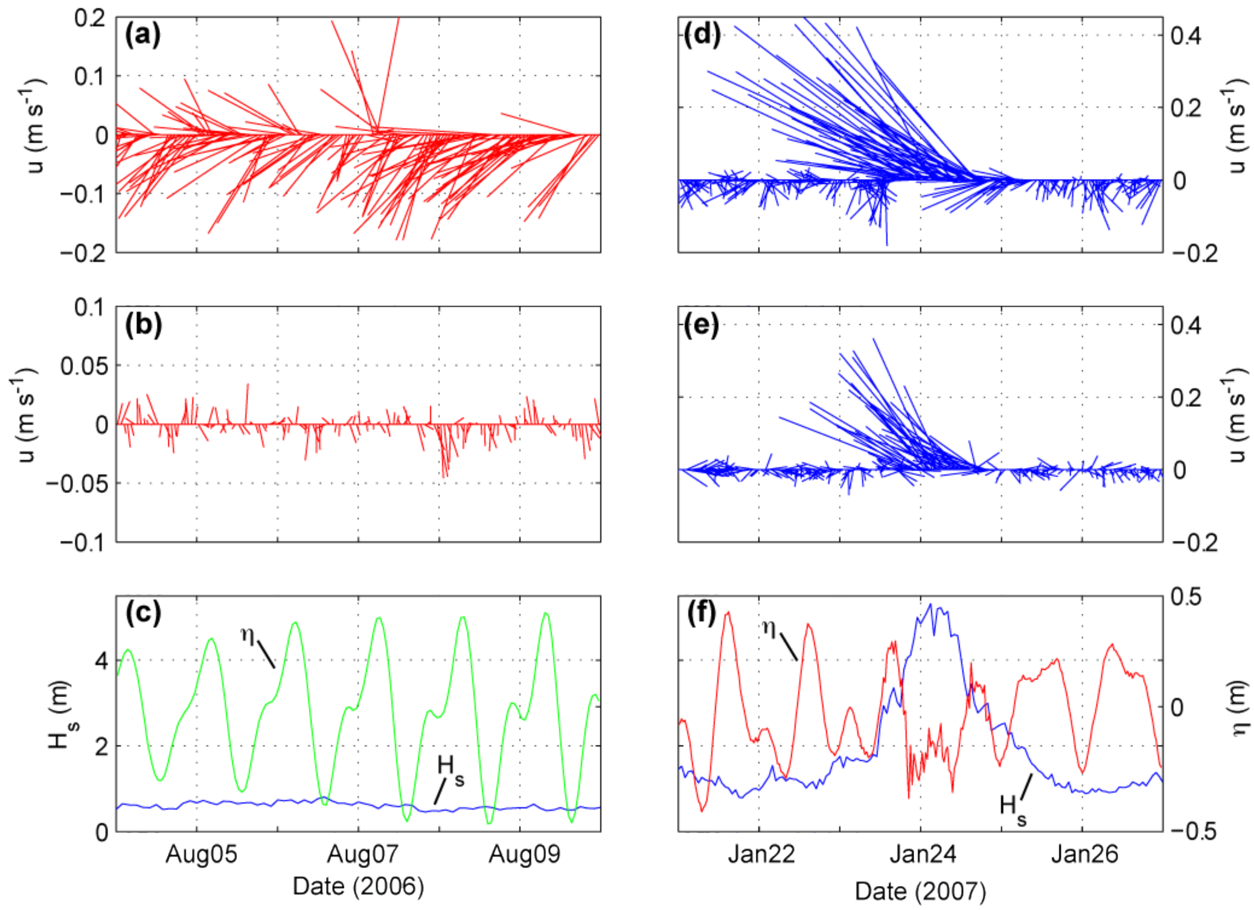

Figure 3.5: Comparison of CRAMP site (a-c) and NW Reef site (d-f) current vectors, water levels, and wave heights. (a) near surface and (b) near-bottom current vectors and (c) water levels and wave height during the week of Aug. 4, 2006 at the CRAMP site. (d) near surface and (e) near bottom current vectors and (f) water levels and wave height during the week of Jan. 21, 2007 at the NW Reef site. Note the large difference in scaling of current vectors (sublplots a and b vs. d and e).

bottom flows (<0.05 m·s^{-1}) appear to be dominated by topographically steered tidal oscillations (Figure 3.5a – b). During the NWS period, a strong depth-integrated jet developed, that was oriented out of the mouth of the bay to the northwest (Figure 3.5d-e). This jet, with current magnitudes up to 0.7 m·s^{-1}, was synchronous with both high incident H_s measured at the NW Reef Site (Figure 3.5f) and with the stronger flows at the Wall site (Figure 3.4d – e).

The wave and current patterns from these two one week time periods matched closely with representations of average conditions for each of the respective classifications (TWW and NWS) during the of the entire one-year time series (e.g. Figure 2.5, *Chapter 2*). This suggests that the two one-week periods are stereotypical, and lend themselves well to the validation of the numerical modeling effort.

3.5.2 Modeling

3.5.2.1 Model Validation

Two measures, comparing scalar model predictions to in situ observations, were used to evaluate model performance: root mean square error (RMSE) and a related normalized skill score termed the "index of agreement" by [*Willmott et al.*, 1985] (IAS). This index of agreement skill (IAS) is defined as

$$IAS = 1 - \frac{\sum (predictions - observations)^2}{\sum \left(\left| predictions - \overline{observations} \right| + \left| observations - \overline{observations} \right| \right)^2}$$

A skill value of one corresponds to a 100% agreement between model prediction and observations, while decreasing values indicate decreasing agreement, or poorer model performance. RMSE was used to evaluate the overall accuracy of the model to predict a particular variable. See [*Lowe et al.*, 2009b; *Sutherland et al.*, 2004; *Warner et al.*, 2008; *Willmott et al.*, 1985] for further discussion of RMSE and "index of agreement" skill and examples of their use in evaluating numerical models.

Best model performance for both the TWW and NWS periods resulted when the optimized wave dissipation parameters (e.g. varying γ_b based on incident H_0/L_0, equation 5) were used in a 3D solution with freshwater discharge at the Hanalei river based on the upstream gauge measurements. The contribution of freshwater input at the Hanalei River to buoyancy forcing was modeled, with salinities at the offshore

Table 3.3 RMSE (a) and model skill (IAS) (b) for current magnitudes (|*U*|), water level (η) and significant wave height (H_s) for mooring sites during the trade wind and NW swell model validation periods. Units for RMSE are as follows: |*U*|: m·s^{-1}, η: m, and H_s: m. IAS is dimensionless.

(a)

	Site	|*U*|	η	H_s
Trade Wind	CRAMP	0.04	0.06	0.07
	Wall	0.03	0.06	0.05
	Mean	0.03	0.06	0.06
NW Swell	NW Reef	0.07	0.09	0.24
	Wall	0.14	0.06	0.41
	Mean	0.11	0.07	0.33

(b)

					Overall Skill
Trade Wind	CRAMP	0.36	0.98	0.88	0.74
	Wall	0.31	0.98	0.42	0.57
	Mean	0.33	0.98	0.65	0.65
NW Swell	NW Reef	0.89	0.90	0.97	0.92
	Wall	0.81	0.96	0.53	0.77
	Mean	0.85	0.93	0.75	0.84

boundary held constant at 35ppt and constant temperature throughout the model. RMSE and IAS, between the *in situ* observations and the model data at selected instrument locations, for the best model runs, are listed in Table 3.3. In general, values of water level (η) and H_s RMSE are within 5-10 % of observed values during both modeled periods; RMSE for current magnitudes (|*U*|) are slightly higher, between 15-20%. This largely results in good IAS (>0.8), although IAS is somewhat smaller (0.4-0.5) for Hs at the Wall site; apparently due to the neglect of wave diffraction by the model, which was identified as an important process at this location [Chapter 2]. IAS values for currents during the TWW period are noticeably poorer (~0.3), despite low RMSE (~0.03 m·s^{-1}); this is most likely due to the fact that small scale temporal and spatial variations in the real surface wind and atmospheric pressure fields are poorly represented by the model input data. These variations likely introduce small-scale variability in the local current patterns that are not well represented in the model, leading to the lower IAS values. If IAS associated with currents during the TWW period are removed, then overall model skill (average for all variables and all locations) is greater than 0.8 during both the TWW and NWS swell periods. This skill level is in the range of other numerical modeling studies of similar scope [Lowe et al., 2009b; Malhadas et al., 2009; Warner et al., 2005].

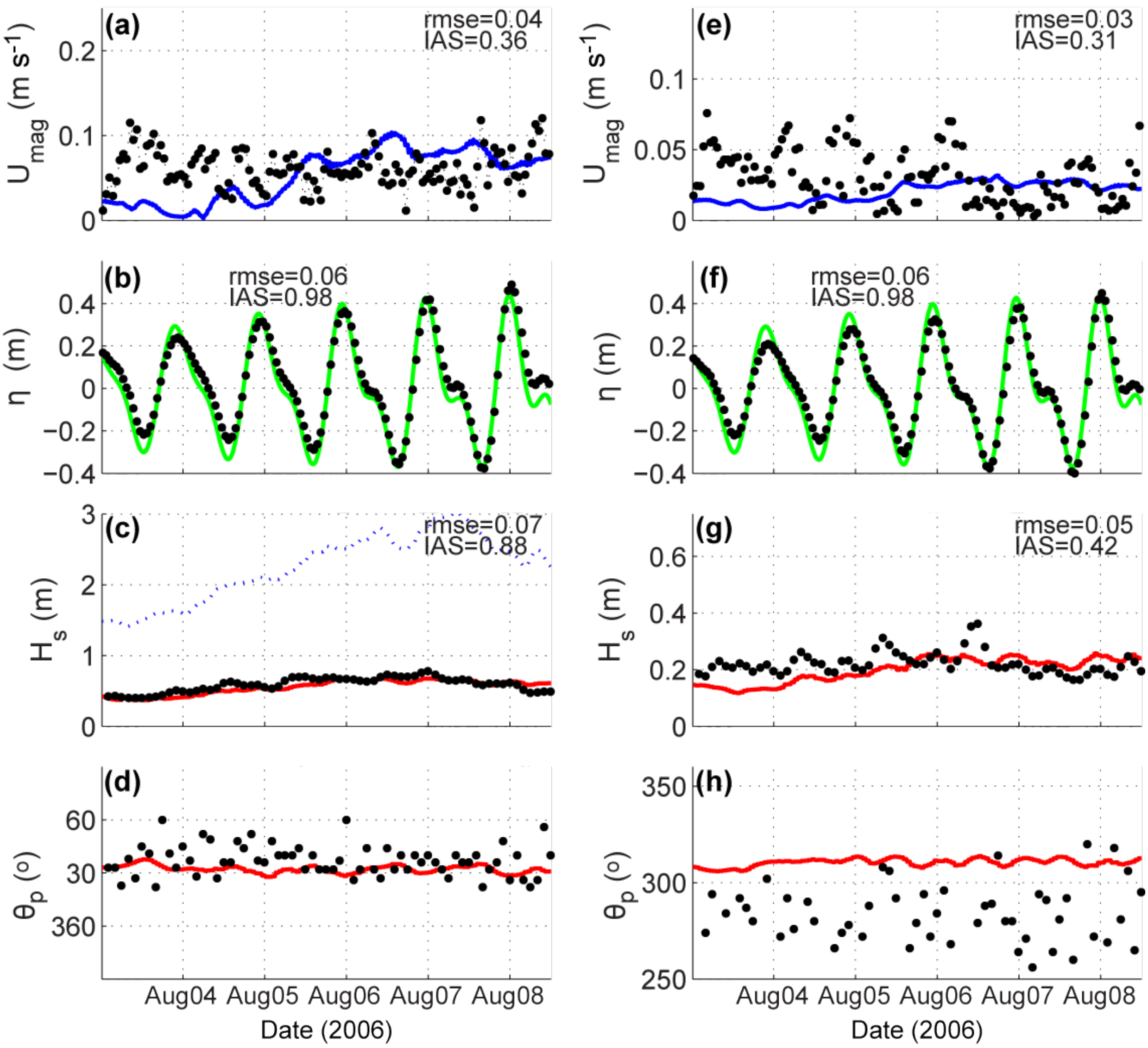

Figure 3.6: Comparison of modeled values (colored solid lines) and observed values (black circles) of U_{mag}, η, H_s, and θ_p during the trade wind period: (a) U_{mag}, (b) η, (c) H_s, and (d) θ_p at the CRAMP Site; (e) U_{max}, (f) η, (g) H_s, and (h) θ_p at the Wall Site. RMSE and skill (IAS) for U_{mag}, η, and H_s are given on the respective sub-plots. The dotted blue line in (c) is H_s at the offshore model boundary, plotted for reference.

Modeled flow fields (circulation patterns) and overall current magnitudes differ markedly between the TWW period and the NWS period. During the TWW period the upper water column was dominated by wind driven flows of less than 0.2 m·s^{-1} over most of the model domain and alongshore transport from east to west outside the mouth of the bay (Figure 3.8a); these flows were stratified, with current magnitudes dropping with depth. During the NWS period, flow fields were dominated by complex, depth-integrated wave driven circulation cells (rip currents) of a variety of scales, with current velocities on the order of 0.6 m·s^{-1} (Figure 3.7b).

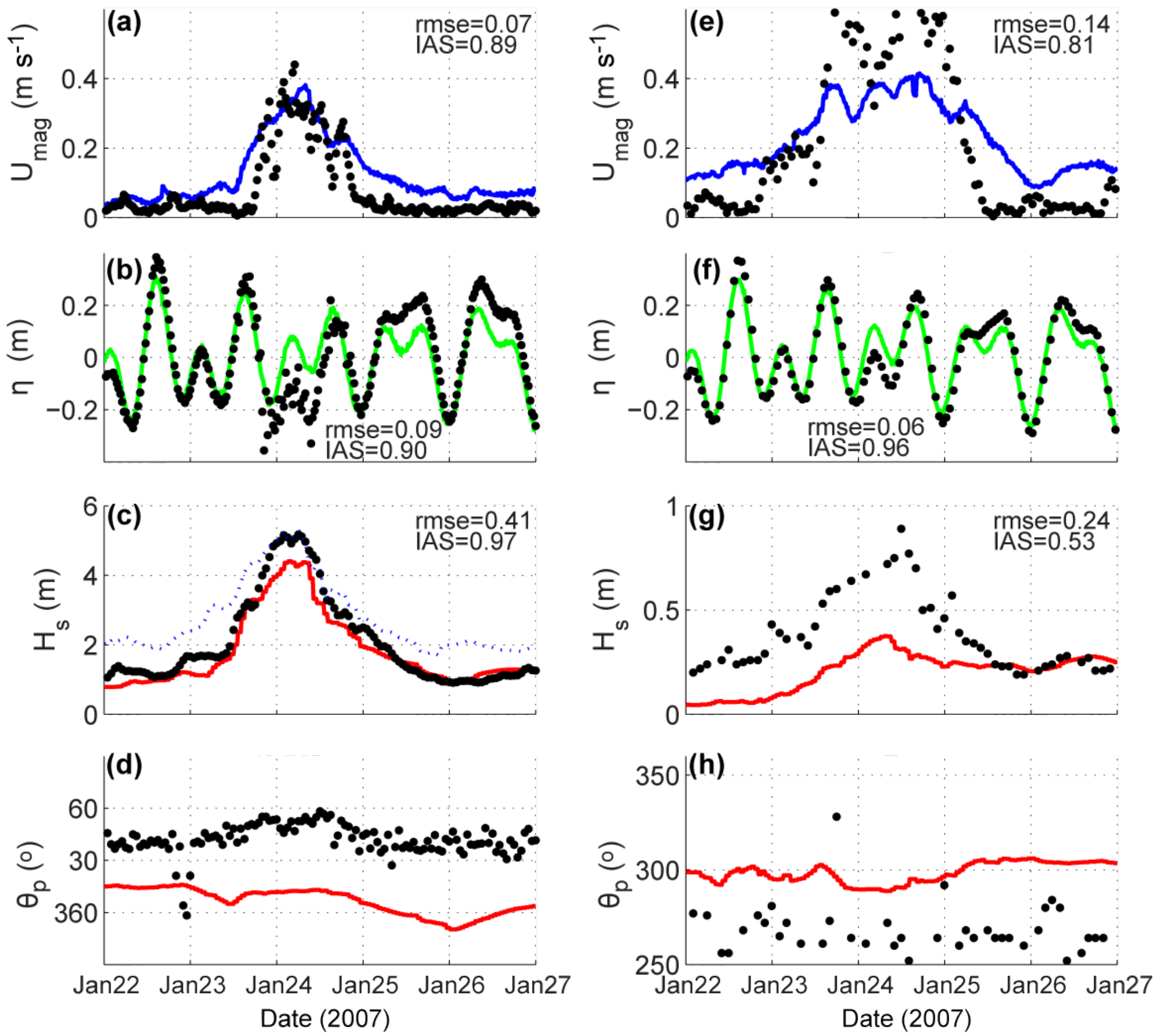

Figure 3.7: Comparison of modeled values (colored solid lines) and observed values (black circles) of U_{max}, η, H_s, and θ_p during the NW swell period: (a) U_{max}, (b) η, (c) H_s, and (d) θ_p at the NW Reef Site; (e) U_{max}, (f) η, (g) H_s, and (h) θ_p at the Wall Site. RMSE and skill (IAS) for U_{max}, η, and H_s are given on the respective sub-plots. The dotted blue line in (c) is H_s at the offshore model boundary, plotted for reference.

The modeled circulation of both respective periods was broadly similar to that suggested by the in situ Eularian mean currents from times classified as either TWW and NWS for the entire in situ observation period (Chapter 2, Figure 2.5). Additionally, modeled TWW circulation was similar to the qualitative observations of circulation under such conditions in Calhoun et al. [2002]'s sedimentary study of the bay. The shoreward location of modeled rip currents within the bay during the NWS period also agrees well with the positions indicated by Figure 6 of Calhoun et al. [2002], as well as with the observations of lifeguards and fishermen (pers. comm.).

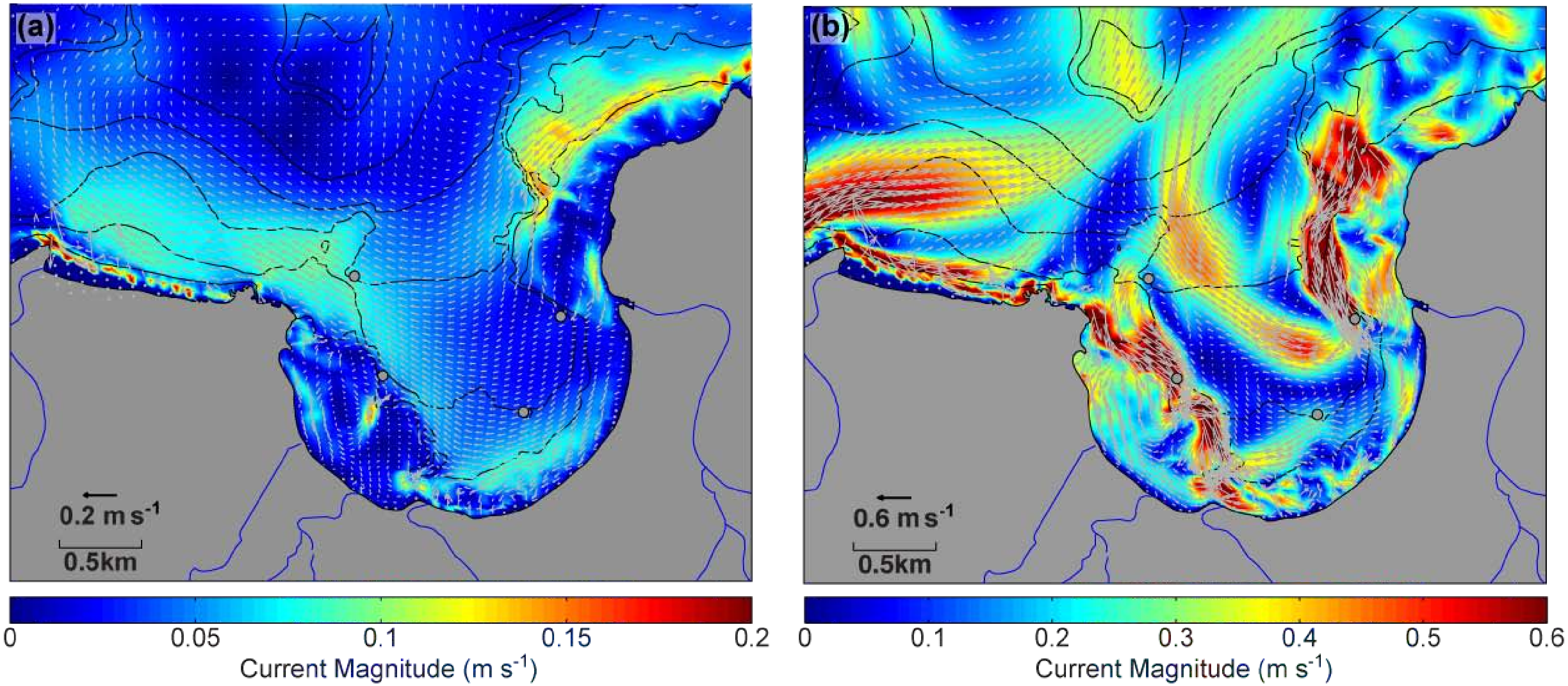

Figure 3.8: Upper water column mean current (sigma layers 3-6) vectors (arrows) and magnitudes (colors) for a single timestep during (a) the trade wind period (August 8, 2100 GMT), and (b) near the peak of the NW swell event (January 24, 05:00 GMT).

This suggests that (1) the model is in good qualitative agreement with observations and that (2) the two periods selected for modeling are respectively largely representative of TWW and NWS conditions during other periods.

Modeled wave setup during the TWW period was generally < 0.05 m (with the exception of a few grid points on the shoreward boundary of the model, likely to do numerical instabilities in the wetting/drying algorithm). This is slightly less than that predicted by Lowe et al [2009b] under similar (trade wind) conditions. Significant wave setup (up to 0.5 m) was predicted over the shallow areas (depth < 2 m) of the exposed nearshore fringing reefs during the peak of the NWS episode, especially over Hanalei Reef and to a lesser extent over Queen's Reef. There was some evidence for wave setdown (<0.1 m) just seaward of these reefs in the model, qualitatively similar to that visible in the observed NW Reef η (Figure 3.5f and 3.7b), however the location and magnitude of this was highly variable in the model and no quantitative comparison is made. Also no direct measurements of water levels over the top of the shallow fringing reefs could be made, so the accuracy of the model's wave setup is impossible to verify.

The large modeled rip current exiting the deep central mouth of the bay and oriented roughly to the northwest (Figure 3.8b), only formed during periods when offshore incident EC_g was greater than 0.15 MW m^{-1}, e.g. H_s greater then 3 m. This agrees very well with observations of the jet apparent in the ADCP data (Figure 3.5d,e). The formation of this jet has implications for both flushing and sediment transport, as discussed in the following sections.

3.5.2.2 Model Flushing Experiment

To assess the contribution of winds, tides, waves, and river flow to the overall flushing of the bay, a series of 10 idealized model runs were performed, using the validated model. The modeling period for all of the run was 36.8 hours; the first 12 hours were discarded to remove model "spin-up" effects and the remaing 24.8 hours (~one full lunar day) were retained for analysis. Forcing for these runs ranged from only tides to three different wave forcing regimes, all with and without a simulated river flood and wind input. Tidal forcing, when included, was varied over a typical mixed, spring tidal cycle (maximum range 0.7 m). All other forcing was held constant over the modeling period.

The three different wave forcing regimes were definied as follows:

1. Modal trade wind: H_s = 1.8 m, T_p = 7.5 s, θ_p =84º
2. Modal NW swell: H_s = 2.4 m, T_p = 12.0 s, θ_p =315º
3. Episodic NW swell: H_s = 5.2 m, T_p = 14.8 s, θ_p =314º

The modal values for both the TWW and NWS condition were found by selecting the peak event frequency of binned values from years 1997-2009 from the NOAA/NCEP Wave Watch III model (WW3, http://polar.ncep.noaa.gov/waves) for the Buoy 1 location for each condition (e.g. Figure 2.3 *Chapter 2*). The value of the episodic NWS was defined by averaging NWS conditions with EC_g greater than 0.25 MW m^{-1}, which was roughly the threshold of offshore EC_g above which both the model and the *in situ* observations suggested the large central jet exiting the bay under NWS extends throughout the water column.

The temporal mean of the input atmospheric model winds used for the TWW model validation were used as wind forcing. River discharge (Q_r) was held constant 100 m^3·s^{-1}, a level consistent with episodic floods of the Hanalei River (Draut, pers. comm, also *Draut et al.*, [2009]). The input used for the 10 model runs is summarized in Table 3.4.

Table 3.4 Mean, minimum and maximum modeled net volume flux (Q_{out}) across the mouth of the bay (see Figure 3.9) and associated residence times of the bay (T_f) of 10 model runs with idealized tidal, wind, wave, and riverine input forcing over a ~24-hour period (1 full tidal cycle). These idealized conditions range from (boundary) tidal forcing only (v1, v3) to modal trade wind and wave fields (v5, v6) to episodic NW swell (v9, v10) with and without a simulated flood of the Hanalei River (freshwater discharge of 100 m^3·s^{-1}); the same tidal cycle (mixed, mean spring tide, see Figure 3.9b) was used for as input for all model runs below except v2, which is forced only with trade winds.

	input							modeled					
	winds		waves			river	tides	Q_{out} (m^3·s^{-1})			T_f (hours)		
run	m·s^{-1}	ºN	H_s m	T_p s	θ_p ºN	Q_r m^3·s^{-1}	range m	Mean	Min	Max	Mean	Max	Min
v1	-	-	-	-	-	-	0.6	30.9	0.3	76.3	171.	1.5·10^4	69.3
v2	7.9	80	-	-	-	-	-	123.5	118.4	136.0	42.8	44.6	38.9
v3	-	-	-	-	-	100	0.6	360.0	312.6	453.1	14.7	16.9	11.7
v4	7.9	80	-	-	-	100	0.6	224.4	137.1	331.0	23.6	38.6	16.0
v5	7.9	80	1.8	7.5	84	-	0.6	162.9	128.7	189.7	32.5	41.1	27.9
v6	7.9	80	1.8	7.5	84	100	0.6	200.2	117.6	276.1	26.4	44.9	19.2
v7	7.9	80	2.4	12.0	315	-	0.6	822.6	773.4	866.2	6.4	6.8	6.1
v8	7.9	80	2.4	12.0	315	100	0.6	602.8	511.8	686.1	8.8	10.3	7.7
v9	7.9	80	5.2	14.8	314	-	0.6	2298.	2232.	2395.	2.3	2.4	2.2
v10	7.9	80	5.2	14.8	314	100	0.6	2171.	2091.	2230.	2.4	2.5	2.4

Depth-integrated volume flux of water across the mouth of the bay during the 10 idealized model runs is presented in Figure 3.8 and Table 3.4. An instanteous flushing time (T_f), defined simply as the volume of water within the bay inside the cross section (V) divided by the mean volume flux out of the bay (Q_{out}, e.g. $T_f = V/Q$, for explicit discription of this method and limitations, see *Monsen et al.*, [2002]) and is also presented in Table 3.4.

Tidal flushing is not a significant flushing mechnism in comparison to winds, waves, and river floods; modeled flushing times using tidal forcing alone are on the order of 6-7 days, a factor of 4 longer than wind forcing. When typical TWW conditions (both wind and wave forcing) are applied, wind forcing is the significant driver of the two, contributing ~75% of overall flushing (although there may be nonlinear interaction between the two forcings). This is consistent with the *in situ* observations and the validation model: circulation in the bay is dominated by wind driven surface flow during TWW conditions.

In all runs with NWS conditions, the bay's flushing is dominated by wave driven flow. Particularly in the most energetic NWS condition, strong wave diven fluxes across the fore-reefs on either side of the bay are evident, as is the signature of the return jet out of the central, deeper part of the bay (Figure 3.9). Flushing times under these most extreme conditions are on the order of 2 hours, approximately one-tenth that of flushing times under TWW conditions (Table 3.4).

The flood river input was also a significant driver of flushing. In the model run forced only with river input and tides, the volume flux is on the order of 350 $m^3 \cdot s^{-1}$, much greater than the riverine input of 100 $m^3 \cdot s^{-1}$. Also, the river input greatly modify flow fields, especially in the vicinity of Hanalei Reef. In the case of combined NWS and flood conditions, the flood input decreased wave driven flow across the reef, apparently a result of wave-current interaction, decreasing overall flushing times relative to runs with no riverine input (Table 3.4). This indicates that momentum flux and freshwater (baroclinic gradients) introduced to by the river have a large impact on the bay's circulation during river flood conditions, although few *in situ* observations support or refute this, and thus the processes is extremely poorly validated in the model.

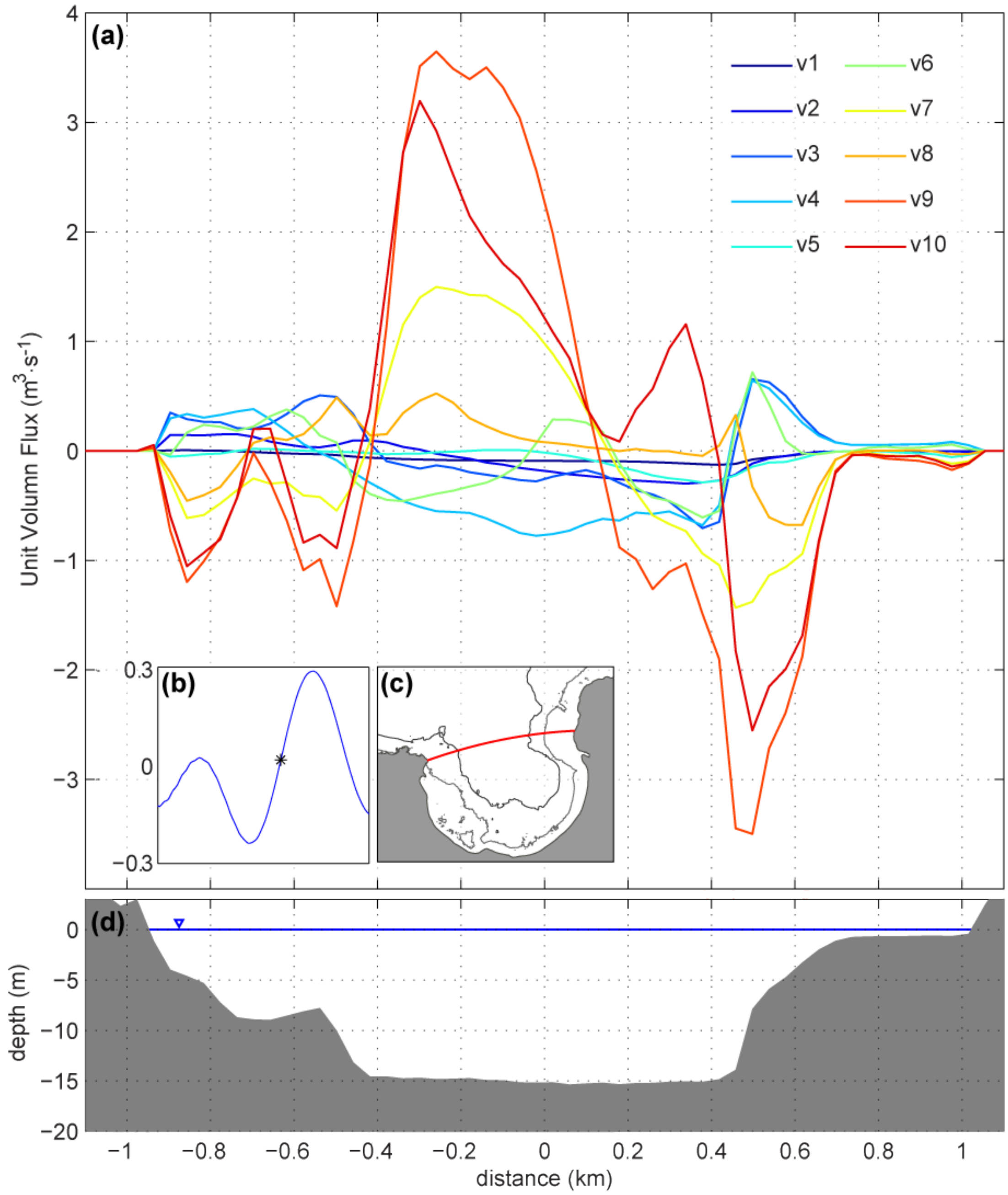

Figure 3.9: (a) Unit volume flux over a cross section at the mouth of Hanalei Bay for 10 different idealized conditions at a selected stage of the tidal cycle shown in inset (b); negative values indicate flux into the bay. Definitions of the idealized conditions are given in Table 3.4. The location of the cross section in relation to the shoreline and the bathymetry of the cross section are given by (c) and (d), respectively.

3.5.2.3 Bed shear and near-bed transport

Both time averaged mean near-bed shear stress (τ_m) and combined shear stress (τ_{max}) resulting from combined wave-current boundary layers [Soulsby et al., 1993] differ markedly across the model domain during TWW conditions and NWS periods. Almost all areas deeper than 10 m, including the entire floor of the bay and the neighboring fore-reefs experience τ_{max} less than 0.2 N·m^{-2}, an estimated threshold for

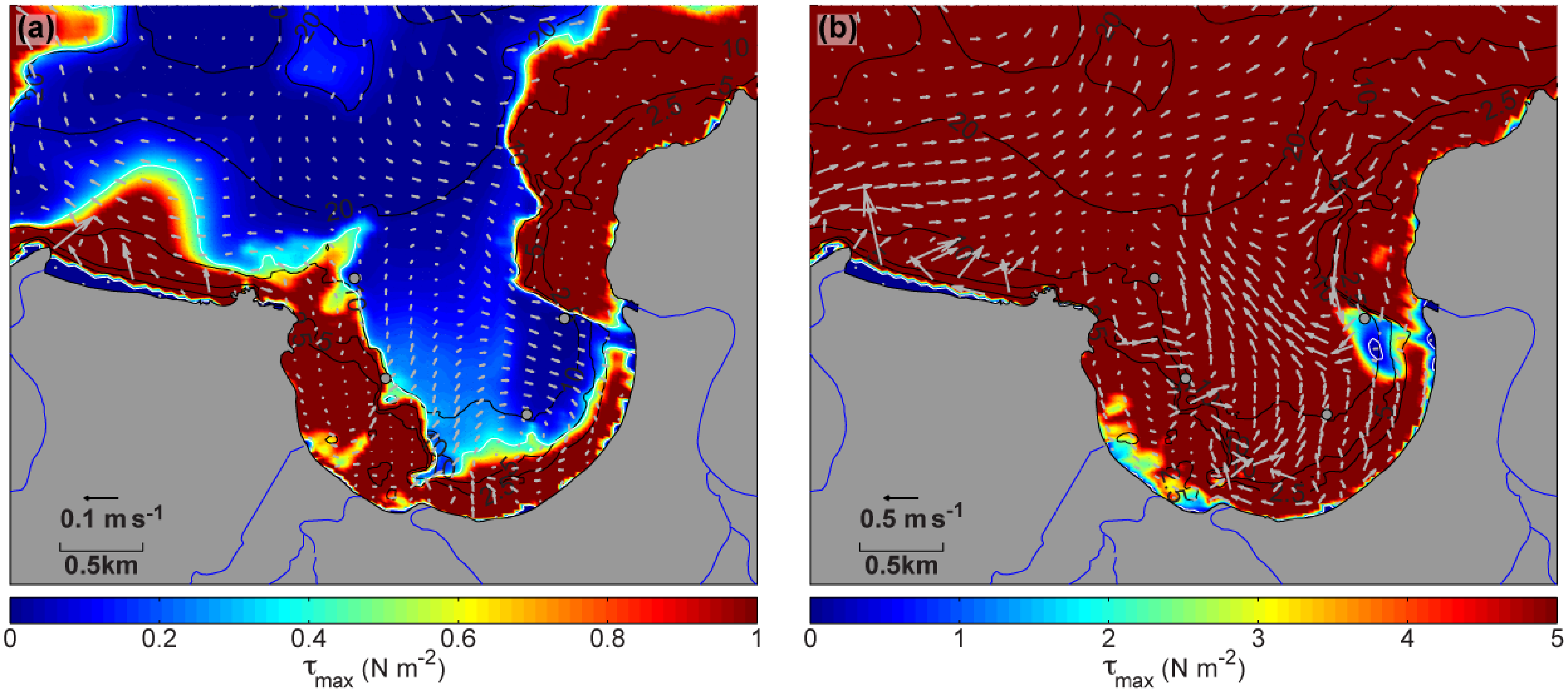

Figure 3.10: Near-bottom mean current vectors (layers 9-12) and maximum (combined wave-current) bed shear stress (τ_{max}) for a single timestep during (a) the trade wind period (August 8, 2100 GMT), and (b) near the peak of the NW swell event (January 24, 0500 GMT). The white contour line indicates τ_{max}=0.2 N/m^2, considered the threshold for sediment mobilization. Note the correspondence between the location of the minima of τ_{max} in (b) and the location of the "Black Hole" in Figure 3.1.

sediment mobilization [*Storlazzi et al.*, 2009], during typical TWW conditions (Figure 3.10a). This area of τ_{max} less than 0.2 N·m^{-2} was reduced to a small area just offshore of the Wall Site, coinciding spatially almost exactly with the area of fine high terrestrial sediment area know as the "Black Hole" during larger NWS conditions (Figure 3.10b).

Near-bed current and associated τ_m vectors were very weak, and generally directed inward, towards the interior of the bay in all modeled conditions except for episodic NWS when offshore EC_g exceeded 0.25 MW m^{-1}. Under these most energetic conditions, representing the top ~10% of NWS events, the seaward flowing jet in the central part of the bay becomes integrated across the full depth of the bay, allowing for strong seaward transport within the bottom boundary layer. This suggests that while more energetic TWW conditions and most NWS events may resuspend sediment within the bay, neither is effective at significantly exporting of sediment from the bay; this only occurs during the most energetic top 10% of NWS events.

3.6. Discussion and Conclusions

3.6.1 Model Performance

This study presents one of the first published applications of coupled numerical wave-circulation models to a fringing coral reef system with slopes greater than 0.1. Some shortcomings of the numerical model were evident: currents velocities tended to be underestimated during larger NWS, even when bed roughness values were optimized for all other conditions. This may be due to inherent limitations of the periodic bore model used to estimated dissipation due to wave breaking when real breakers are typically of the plunging type; simplifying assumptions in the estimation of wave dissipation forces; or the lack of inclusion of wave diffraction; most likely some combination of all three. Despite these shortcomings, overall model skill was not significantly poorer than other modeling studies with less steep slopes and less extreme wave conditions (e.g. [*Lowe et al.*, 2009b; *Malhadas et al.*, 2009; *Warner et al.*, 2005].

The wave model performed best when sand and reef where assigned spatially varying hydraulic bed roughness (k_w) values of 0.01 and 0.10 m respectively. This value for coral reefs is in the range found by other researchers [*Hearn et al.*, 2001;

Lowe et al., 2005]; and while the model was not particularly sensitive to values of k_w in this range (~0.08-0.15 m), it was important to assign sandy areas a value of k_w an order of magnitude lower than reef areas to avoid under estimation of wave heights within the bay. The flow model also required spatially varying values of bed roughness (z_0) similar to k_w to reproduce circulation patterns inferred from ADCP observations. This contrasts with the findings of *Lowe et al.*, [2009b], who successfully modeled circulation in another Hawaiian bay using spatially uniform bed roughness values. This is likely due to morphological differences in the two bays: Hanalei has is an open bay with a (mostly) uniform sandy floor and shallow fringing reef platforms on either side, while Kaneohe bay, studied by *Lowe et al.*, [2009b], is a relatively linear barrier reef system.

The model was highly sensitive to the breaker height coefficient (γ_b), with optimal γ_b values depending on incident deepwater wave steepness (H_0/L_0). Best overall model skill occurred when γ_b was varied between 0.9 and 1.2 according to a relationship with H_0/L_0 and fore-reef slope (equation 5); i.e. the "surf similarity" parameter [*Battjes*, 1974]. These values of γ_b are significantly higher than those commonly used in other wave modeling studies (e.g. *Lowe et al.*, 2009b; *Mulligan et al.*, 2008; *Ris et al.*, 1999), although *Massel and Gourlay* (2000) suggest this range of values for reef slopes such as those found in Hanalei Bay.

3.6.2 Circulation and hydrodynamic forcing

Historically, two different circulation regimes dominate Hanalei Bay; the regime associated with trade wind wave (TWW) conditions, which occurs ~80% of the time and the regime associated with episodic long-period north-west swells (NWS) occurs ~10% of the time; conditions not categorically one or the other tend to be relatively quiescent [*Chapter 2*]. Observations and model results both show that the near-surface waters of the bay under TWW forcing are dominated by an east-to-west wind driven flow, typically with a minor contribution from wave forcing primarily on the eastern side of the bay (Figure 3.8a, Figure 3.11). Flows in the deeper part of the bay tend to be weak oscillatory (tidal) currents, with speeds less than 0.05 $m\cdot s^{-1}$. Flushing times during TWW, based on water volume flux calculated by the model, range between 25 and 50 hours.

NWS episodes are dominated by wave driven flows, which become increasingly vigorous and uniform with depth with increasing incident wave energy flux (EC_g). A large dual-circulation cell begins to develop in the model at around the mean value for NWS events (~0.08 MW m^{-1} incident EC_g, or H_s ~ 2.4 m, T_p ~ 12 s), with wave driven residual flows across the fringing reefs on both sides, into the bay and a return flow out the center of the bay. During more extreme NWS events (around incident EC_g >0.25 MW m^{-1} or H_s >~4 m, T_p >~14 s), this circulation structure becomes well defined, with the return flow out the center of the bay exhibiting characteristics of a jet; the entire bay essentially becomes a single large scale rip current cell with smaller cells embedded along the shoreline (Figure 3.8b). In these conditions, both the model and *in situ* observations indicate flows up to 1 m·s^{-1} or more across the fringing reefs and a return flow of up to 0.5 m·s^{-1} throughout the water column in the deeper central part of the bay. Flushing times for average NWS conditions are on the other of 7 hours, and as small as 2 hours, during the more extreme episodes.

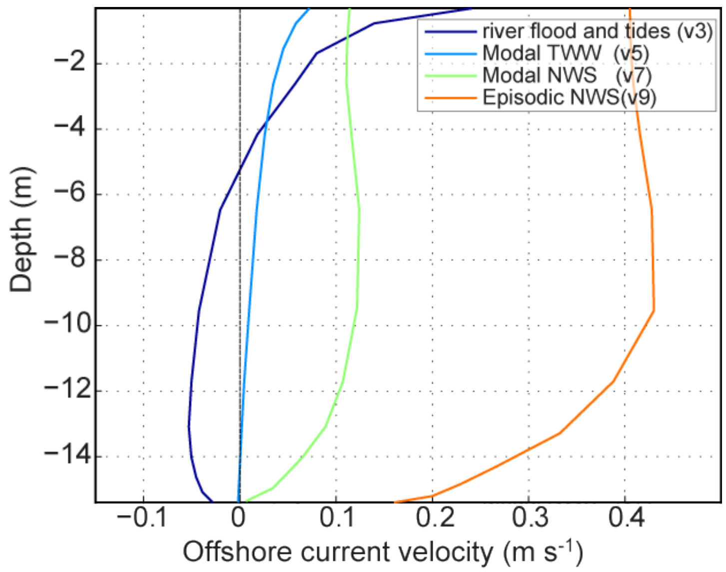

Figure 3.11: Current/depth profiles near the center of the mouth of the bay from selected flushing experiment model runs. Model run numbers in the legend correspond to those in Table 3.4: "v3" is river flood discharge and tidal only forcing; "v5" is modal trade wind (TWW) forcing; "v7" is modal northwest swell (NWS); "v9" is episodic NWS. Current velocity values indicate flow along an axis (350°N) perpendicular to the cross section in Figure 3.9; positive values indicate offshore flow; negative values indicate flow into the interior of the bay.

During modeled floods of the Hanalei River, the high freshwater discharge introduced both buoyancy forcing to the bay and significant momentum flux at the surface near the mouth of the river. In the absence of wind and wave forcing, the modeled density structure and circulation was that of partially mixed estuary, with momentum and buoyancy-driven offshore flow in the upper layers and a return flow of more saline water along the bottom (Figure 3.11). When combined with TWW or NWS forcing, the effect of the freshwater discharge was often complex; however, the overall effect in the central part of the bay was generally some degree of stratification, with a tendency to enhance offshore flow in the surface layers and diminish it (or enhance shoreward flow) in the bottom layers.

Despite the fundamental differences in circulation patterns under the two conditions, model output shows that sufficient wave energy is present to resuspend seabed sediment throughout most of the bay during both more the energetic TWW conditions and all NWS events; only the area of fine-grained terrestrial sediment know as the “Black Hole” remains uniquely sheltered in all but the ~10% most energetic NWS events. This is consistent with [*Draut et al.*, 2009; *Storlazzi et al.*, 2009], who observed severe increases in turbidity and some reworking of flood deposites on the floor of the bay, even during TWW conditions, when flood deposits were present. Water quality may be severly impacted during these resuspension events, not only due to the increase in turbidity, but also by mobilization of organic contaminants and metals found in the terrestrial sediments [*Draut et al.*, 2009].

The modeled maximum bed shear stress during the ~10% most energetic NWS events is on the order of 25 N m^{-2} on the bay’s exposed fore-reefs. This is well over the threshold to cause breakage and colony failure of most reef building corals [e.g. *Madin and Connolly*, 2006; *Storlazzi et al.*, 2005]. This helps explain why the exposed fore-reefs are algal-dominated with relatively low coral cover (<15%), most of which is encrusting or colonial forms. More protected areas have higher overall coral cover and a greater dominance of larger (non-encrusting) colonies [*Friedlander and Brown*, 2005; *Jokiel et al.*, 2004].

3.6.3 Implications

The vast majority of the estimated annual 1.76×10^4 Mg fluvial sediment load of the Hanalei River is delivered to Hanalei Bay during 1-10 episodic flood events each year [*Calhoun and Fletcher*, 1999; *Draut et al.*, 2009]. Geological evidence suggests that this flood sediment accumulates on the floor of the bay until the time that wave energy and circulation become vigorous enough to transport them out of the bay; [*Draut et al.*, 2009] documented an approximately 20% increase in flood sediment retained in the bay over the course of a year due to the timing of flood events relative to NWS events.

The model presented here indicates that incident (NWS) wave energy flux (EC_g) of around 0.25 MW m^{-1} (coinciding with waves on the order of H_s>4 m, T_p>14 s) is a minimum threshold for wave-driven near-bed residual sediment transport out of the bay to occur (Figure 3.11); thus only events above this approximate threshold appear to be capable of removing large quantities of flood deposits from the bay. NWS events of this magnitude occurred only 7 times during the approximately one year of *in situ* observations within the bay, and account for less than 1% of the time in the much longer Buoy 1 (1981-2009) and NOAA Wave Watch III (http://polar.ncep.noaa.gov/waves/, 1997-2010) records.

The roughly similar return time of the floods and episodic NWS, combined with the fact that flood deposits do not appear to have significantly increased in the last 5000 years relative to the total amount of sediment delivered *Calhoun et al.*, [2002], suggests that these two processes of sediment delivery and removal are roughly in balance on decadal or centennial timescales. Interannual variability in the number of episodic floods (i.e. heavy rainfall events) that deliver sediment to the bay and the generation of remotely-generated, long-period swell events that remove sediment from the bay, however, is high and, unlike many temperate continental locations, the two phenomena are strongly decoupled [*Draut et al.*, 2009]. The number of episodic NWS are positively correlated with the warm or El Niño phase of the El Niño/Southern Oscillation (ENSO) index (Figure 3.12, *Bromirski et al.*, 2005; *Wang and Swail*, 2006); conversely some researchers have found a weak negative correlation between ENSO and rainfall in the Hawaiian islands [*Chu and Chen*, 2005; *Kolivras and Comrie*, 2007], although on cursory examination there appears to be no correlation between ENSO and Hanalei River floods (Figure 3.12).

The episodic nature of sediment (and often associated nutrient and toxicant) delivery to and removal from many such an embayment means sedimentation patterns and water quality are very sensitive to changes in either process. It is not yet clear how global climate change will affect storm tracks, their intensity, and/or frequency [e.g. *Collins et al.*, 2010; *IPCC*, 2007]. A shift in any one of these, however, will likely result in (decoupled) changes in the frequency, intensity, and timing of local floods and remotely-generated long-period, large waves, which in turn will cause changes in the timing and magnitude of sediment delivery, residence time, and advection out of the bay. A small decrease in the number and/or intensity of episodic NWS events could lead to an increasing accumulation of flood deposits in the bay (i.e., an expansion of the "Black Hole") and subsequently increased in the mean turbidity throughout much of the bay during the frequent TWW resuspension events [e.g. *Storlazzi et al.*, 2009]. The ecosystem response to such a scenario would likely be complicated. While coral communities in the interior of the bay that are currently sheltered from high wave energy may suffer from higher turbidity, the reduced episodic high shear stress could encourage an increase in coral cover on the bays exposed fore-reefs.

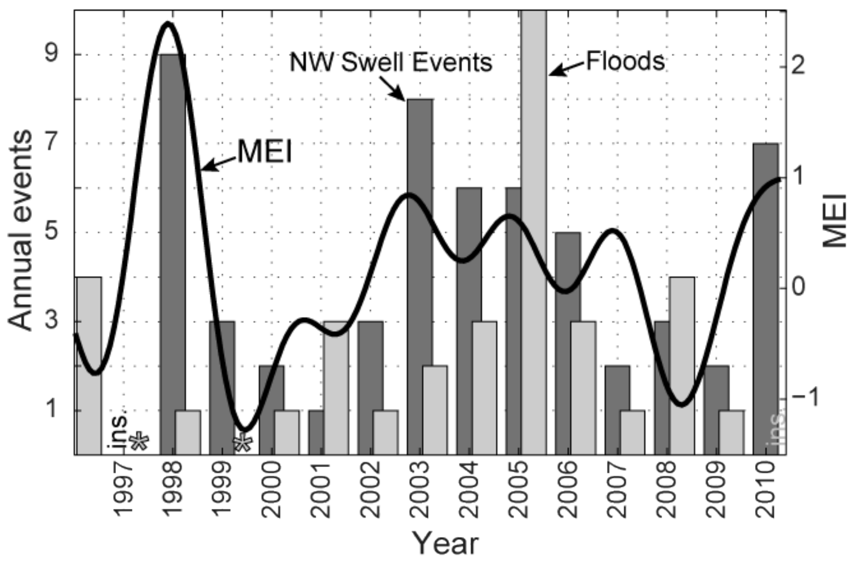

Figure 3.12: Comparison of the annual number of episodic floods or the Hanalei River (defined as mean daily discharge >50m^3·s^{-1}) and episodic NWS events (defined as EC_g > 0.4 MW m^{-1}) for years 1997 – 2010. The multivariate ENSO Index (MEI), smoothed with an 18-month low-pass filter, is included for comparison. Episodic NWS events and MEI are correlated (r = 0.76, p<0.01), floods and MEI are not (r = -0.13, p=0.46); NWS events and floods also show no signs of correlation with each other (r = -0.04, p=0.93). Years with no annual floods are indicated with an asterisk. Years with insufficient data to accurately estimate annual events are marked with "ins". Annual counts of floods and NW swell events are shifted 6 months such that the years center on boreal winter, i.e. "1997" refers to a year centered on the boreal winter of 1996/1997. MEI data provided by http://www.esrl.noaa.gov/psd/people/klaus.wolter/MEI/; wave data by http://polar.ncep.noaa.gov/waves/.

While Hanalei, with its high fluvial sediment loading relative to the bay's size and exposure to episodically high wave events, may represent something of an extreme, these physical processes are common to embayments and fringing reefs

[*Angwenyi and Rydberg*, 2005; *Coronado et al.*, 2007; *Hench et al.*, 2008; *Kraines et al.*, 1998; *Lowe et al.*, 2009a; *Storlazzi et al.*, 2004; *Wolanski et al.*, 2003]. Embayments with fringing reefs are common to tropical and sub-tropical high islands throughout the Pacific, Caribbean, and Indian Oceans and tend to be centers of human population and infrastructure.

Many studies suggest anthropocene climate change will be manifested as departures from historical weather patterns e.g., [*IPCC*, 2007]. This, coupled with increases in terrestrial erosion rates due to anthropogenically-driven changes in land use and land cover, suggests that the sedimentary characteristics, water quality, and benthic ecosystems of many of these fringing reef embayments will likely undergo changes on the timescale of years to decades as the balance between sediment delivery to and removal from are altered. It appears that such changes may already be underway in many places [*Syvitski et al.*, 2005; *Zalasiewicz et al.*, 2010]. While there have been a number of excellent programs investigating land-sea coupling of large systems (e.g., *EUROSTRATAFORM*, [2010]; *MARGINS*, [2010]; *Nittrouer and Kravitz*, [1996]), there have been limited studies of smaller, high-relief tropical and subtropical systems such as addressed here that have been shown to be important contributors to the global flux of material to the ocean [*Milliman and Syvitski*, 1992]. Further coupled land-sea studies of smaller, but more common, coastal watersheds are necessary to not only better understand their contribution to global fluxes of material to the coastal ocean, but also predict how global climate change may impact these important coastal ecosystems and their human inhabitants [*Hoegh-Guldberg and Bruno*, 2010].

3.7 Acknowledgments

Many thanks are due to Edwin Elias (USGS) and Sean Vitousek (formerly with University of Hawaii, now with Stanford University) for their invaluable help in understanding and initially setting up the Delft3D. Many thanks also to Kathy Presto (USGS) for help with both field work and analyzing/interpreting much of the *in situ* data; Josh Logan (USGS) and Molly Timmers (NOAA/UH) for assisting in field work. John Rooney (NOAA/UH) and Jonathon Weiss (NOAA/UH) for collecting multibeam bathymetry to supplement existing LiDAR and multibeam and aggregating the data. Many thanks also to Matt Rosener (Hanalei Watershed Hui) and Carl Berg (formerly Hanalei Watershed Hui) for field support and local knowledge. Thanks to Kevin Wong (NOAA) for support and discussion on content. Amanda Toperoff (NOAA/UH) provided excellent assistance in the preparation of figures.

This work was jointly supported by US Geological Survey's Coral Reef Project, NOAA's Coral Reef Conservation Program, and the Australia Institute of Marine Science AIMS@JCU program.

3.8 References

Andrews, J. C., and G. L. Pickard (1990), The physical oceanography of coral-reef systems, in *Coral reefs*, edited by Z. Dubinsky, pp. 11-48, Elsevier, Amsterdam.

Angwenyi, C. M., and L. Rydberg (2005), Wave-driven circulation across the coral reef at Bamburi Lagoon, Kenya, *Estuarine, Coastal Shelf Sci.*, *63*(3), 447-454.

Battjes, J. A. (1974), Surf Similarity, *Proceedings of the 14th Coastal Engineering Conference, American Society of Civil Engineers*, 466-480.

Battjes, J. A., and J. P. F. M. Janssen (1978), Energy loss and set-up due to breaking of random waves, paper presented at 16th International Conference Coastal Engineering, New York, NY: ASCE, Hamburg, Germany.

Battjes, J. A., and M. J. F. Stive (1985), Calibration and Verification of a Dissipation Model for Random Breaking Waves, *J. Geophys. Res.*, *90*(C5), 9159-9167.

Booij, N., R. C. Ris, and L. H. Holthuijsen (1999), A third-generation wave model for coastal regions, Part I, Model description and validation, *J. Geophys. Res.*, *104*(C4), 7649-7666.

Bromirski, P. D., D. R. Cayan, and R. E. Flick (2005), Wave spectral energy variability in the northeast Pacific, *J. Geophys. Res.*, *110*.

Calhoun, R. S., and C. H. Fletcher (1999), Measured and predicted sediment yield from a subtropical, heavy rainfall, steep-sided river basin: Hanalei, Kauai, Hawaiian Islands, *Geomorphology*, *30*, 213-226.

Calhoun, R. S., C. H. Fletcher, and J. N. Harney (2002), A budget of marine and terrigenous sediments, Hanalei Bay, Kauai, Hawaiian Islands, *Sedimentary Geology*, *150*, 61-87.

Callaghan, D. P., P. Nielsen, N. Cartwright, M. R. Gourlay, and T. E. Baldock (2006), Atoll lagoon flushing forced by waves, *Coastal Engineering*, *53*(8), 691-704.

Chu, P.-S., and H. Chen (2005), Interannual and Interdecadal Rainfall Variations in the Hawaiian Islands*, *J. Clim.*, *18*(22), 4796-4813.

Collins, M., S.-I. An, W. Cai, A. Ganachaud, E. Guilyardi, F.-F. Jin, M. Jochum, M. Lengaigne, S. Power, A. Timmermann, G. Vecchi, and A. Wittenberg (2010), The impact of global warming on the tropical Pacific Ocean and El Niño, *Nature Geoscience*, *3*(6), 391-397.

Coronado, C., J. Candela, R. Iglesias-Prieto, J. Sheinbaum, M. López, and F. J. Ocampo-Torres (2007), On the circulation in the Puerto Morelos fringing reef lagoon, *Coral Reefs*, *26*(1), 149-163.

Dean, R. G., and R. A. Dalrymple (1984), *Water wave mechanics for engineers and scientists / Robert G. Dean, Robert A. Dalrymple*, Prentice-Hall, Englewood Cliffs, N.J. :.

Dingemans, M. W., A. C. Radder, and H. J. De Vriend (1987), Computation of the driving forces of wave-induced currents. *Coastal Engineering*, 11: 539-563.

Dollar, S. J. (1982), Wave stress and coral community structure in Hawaii, *Coral Reefs*, *1*(2), 71-81.

Draut, A. E., M. H. Bothner, M. E. Field, R. L. Reynolds, S. A. Cochran, J. B. Logan, C. D. Storlazzi, and C. J. Berg (2009), Supply and dispersal of flood sediment from a steep, tropical watershed: Hanalei Bay, Kaua'i, Hawai'i, USA, *Geological Society of America Bulletin*, *121*(3-4), 574-585.

EUROSTRATAFORM (2010), EUROSTRATAFORM Program description., *http://www.noc.soton.ac.uk/gg/EUROSTRATAFORM/project_description.html*

Fabricius, K. E. (2005), Effects of terrestrial runoff on the ecology of corals and coral reefs: review and synthesis, *Mar. Pollut. Bull.*, *50*(2), 125-146.

Field, M. E., C. S. Berg, and S. A. Cochran (2007), Science and management in the Hanalei watershed; a trans-disciplinary approach 92 pp, U.S. Geological Survey

Friedlander, A. M., and J. D. Parrish (1997), Fisheries harvest and standing stock in a Hawaiian Bay, *Fisheries Research*, *32*, 33-50.

Friedlander, A. M., and E. K. Brown (2005), Hanalei benthic communities since 1992: spatial and temporal trends in a dynamic Hawaiian coral reef ecosystem, 32 pp, Hawai‘i Cooperative Studies Unit

Fulton, C. J., and D. R. Bellwood (2005), Wave-induced water motion and the functional implications for coral reef fish assemblages, *Limnol. Oceanogr.*, *50*(1), 255-264.

Gourlay, M. R., and G. Colleter (2005), Wave-generated flow on coral reefs--an analysis for two-dimensional horizontal reef-tops with steep faces, *Coastal Engineering*, *52*(4), 353-387.

Grant, W., and O. S. Madsen (1979), Combined Wave and Current Interaction With a Rough Bottom, J. Geophys. Res., . *J. Geophys. Res.*, *84*(C4), 1797-1808.

Grigg, R. W. (1998), Holocene coral reef accretion in Hawaii: a function of wave exposure and sea level history, *Coral Reefs*, *17*, 263-272.

Hamner, W. M., and E. Wolanski (1988), Hydrodynamic forcing functions and biological processes on coral reefs: a status review, *Proc 6th Int Coral Reef Symp*, *1*(103-113).

Hearn, C., M. Atkinson, and J. Falter (2001), A physical derivation of nutrient-uptake rates in coral reefs: effects of roughness and waves, *Coral Reefs*, *20*(4), 347-356.

Hearn, C. J. (1999), Wave-breaking hydrodynamics within coral reef systems and the effect of changing relative sea level, *J. Geophys. Res.*, *104*(C12), 30,007–030,019.

Hench, J. L., J. J. Leichter, and S. G. Monismith (2008), Episodic circulation and exchange in a wave-driven coral reef and lagoon system, *Limnol. Oceanogr*, *53*(6), 2681-2694.

Hoegh-Guldberg, O., and J. F. Bruno (2010), The Impact of Climate Change on the World's Marine Ecosystems, *Science*, *328*(5985), 1523-1528.

IPCC (2007), *Climate change 2007: The physical science basis. Contribution of Working Group I to the Fourth Assessment Report of the Intergovernmental Panel on Climate Change*, 996 pp., Cambridge University Press, Cambridge and New York, pp.

Jokiel, P. L., E. K. Brown, A. Friedlander, S. K. Rodgers, and W. R. Smith (2004), Hawai‘i Coral Reef Assessment and Monitoring Program: Spatial Patterns and Temporal Dynamics in Reef Coral Communities, *Pac. Sci.*, *58*, 159-174.

Kaminsky, G. M., and N. C. Kraus (1993), Evaluation of depth-limited wave breaking criteria, *Proceedings of International Symposium on Ocean Wave Measurement and Analysis Waves 93*(ASCE, New York), 180-193.

Kolivras, K., and A. Comrie (2007), Regionalization and variability of precipitation in Hawaii, *Physical Geography*, *28*(1), 76-96.

Kraines, S., T. Yanagi, M. Isobe, and H. Komiyama (1998), Wind-wave driven circulation on the coral reef at Bora Bay, Miyako Island, *Coral Reefs 17*(2), 133-143.

Lesser, G. R., J. A. Roelvink, J. A. T. M. van Kester, and G. S. Stelling (2004), Development and validation of a three-dimensional morphological model, *Coastal Engineering*, *51*(8-9), 883-915.

Longuet-Higgins, M. S., and R. W. Stewart (1964), Radiation stresses in water waves; a physical discussion, with applications, *Deep Sea Research*, *11*, 529-562.

Lowe, R. J., J. L. Falter, M. D. Bandet, G. Pawlak, M. J. Atkinson, S. G. Monismith, and J. R. Koseff (2005), Spectral wave dissipation over a barrier reef, *J. Geophys. Res.*, *110*, 16.

Lowe, R. J., J. L. Falter, S. G. Monismith, and M. J. Atkinson (2009a), Wave-Driven Circulation of a Coastal Reef-Lagoon System, *Journal of Physical Oceanography*, *39*(4), 873-893.

Lowe, R. J., J. L. Falter, S. G. Monismith, and M. J. Atkinson (2009b), A numerical study of circulation in a coastal reef-lagoon system, *J. Geophys. Res.*, *114*(C6), C06022.

Madin, J. S., and S. R. Connolly (2006), Ecological consequences of major hydrodynamic disturbances on coral reefs, *Nature*, *444*, 477-480.

Madsen, O. S., Y.-K. Poon, and H. C. Graber (1988), Spectral wave attenuation by bottom friction: Theory, paper presented at Proceedings of 21th International Conference on Coastal Engineering, Am. Soc. of Civ. Eng., New York.

Malhadas, M., R. Neves, P. Leitão, and A. Silva (2009), Influence of tide and waves on water renewal in Óbidos Lagoon, Portugal, *Ocean Dynamics*, *60*(1), 41-55.

MARGINS (2010), MARGINS Program description. , *http://www.nsf-margins.org/MARGINS_Office/AboutMARGINS.html*.

Massel, S. R., and M. R. Gourlay (2000), On the modelling of wave breaking and set-up on coral reefs, *Coastal Engineering*, *39*(1), 1-27.

Milliman, J. D., and J. P. M. Syvitski (1992), Geomorphic/tectonic control of sediment discharge to the ocean: the importance of small mountainous rivers, *Journal of Geology*, *100*, 525-544.

Moberly, R., and T. Chamberlain (1964), Hawaiian Beach Systems, Hawai‘i Institute of Geophysics Report 64-2, University of Hawai‘i, Honolulu.

Monsen, N. E., J. E. Cloern, L. V. Lucas, and S. G. Monismith (2002), A Comment on the Use of Flushing Time, Residence Time, and Age as Transport Time Scales, *Limnol. Oceanogr.*, *47*(5), 1545-1553.

Mulligan, R. P., A. E. Hay, and A. J. Bowen (2008), Wave-driven circulation in a coastal bay during the landfall of a hurricane, *J. Geophys. Res.*, *113*, C05026.

Munk, W., and M. Sargent (1948), Adjustment of Bikini Atoll to waves, *Transactions, Am. Geo. Union*, *29*(6), 855-860.

Nittrouer, C. A., and J. H. Kravitz (1996), STRATAFORM: A Program to study the creation and interpretation of sedimentary strata on continental margins, *Oceanography*, *9*(3), 146-152.

O’Connor, B. A., and D. Yoo (1988), Mean bed friction of combined wave-current flow, *Coastal Engineering*, *12*, 1-21.

Pawlowicz, R., B. Beardsley, and S. Lentz (2002), Classical tidal harmonic analysis including error estimates in MATLAB using T_TIDE, *Computers & Geosciences*, *28*(8), 929-937.

Polyakov, V., A. Fares, D. Kubo, J. Jacobi, and C. Smith (2007), Evaluation of a non-point source pollution model, AnnAGNPS, in a tropical watershed, *Environmental Modelling & Software*, *22* 1617-1627.

Ris, R., L. Holthuijsen, and N. Booij (1999), A third-generation wave model for coastal regions: 2. Verification, *J. Geophys. Res.*, *104*, 7667- 7681.

Roelvink, J. A., and C. K. F. M. v. Banning (1994), Design and development of DELFT3D and application to coastal morphodynamics, in *Hydroinformatics '94*, edited by A. Verwey, et al., Balkema, Rotterdam, Balkema, Rotterdam.

Roelvink, J. A., and D. J. Wasltra (2004), Keeping in simple by using complex models, in *6th International Conference on Hydroscience and Engineering, Advances in Hydro-Science and Engineering*, edited, Brisbane, Australia., Brisbane, Australia.

Roger, C. S. (1993), Hurricanes and coral reefs: the intermediate disturbance hypothesis revisited., *Coral Reefs*, *12*(2), 127-138.

Soulsby, R. L., L. Hamm, G. Klopmanc, D. Myrhaugd, R. R. Simonse, and G. P. Thomas (1993), Wave-current interaction within and outside the bottom boundary layer, *Coastal Engineering*, *21*, 41-69.

Storlazzi, C. D., A. S. Ogston, M. H. Bothner, M. E. Field, and M. K. Presto (2004), Wave- and tidally-driven flow and sediment flux across a fringing coral reef: Southern Molokai, Hawaii, *Continental Shelf Research*, *24*(12), 1397-1419.

Storlazzi, C. D., E. K. Brown, M. E. Field, K. Rodgers, and P. L. Jokiel (2005), A model for wave control on coral breakage and species distribution in the Hawaiian Islands, *Coral Reefs*, *24*(1), 43-55.

Storlazzi, C. D., M. E. Field, M. H. Bothner, M. K. Presto, and A. E. Draut (2009), Sedimentation processes in a coral reef embayment: Hanalei Bay, Kauai, *Marine Geology*, *264* (3-4), 140–151.

Sutherland, J., A. H. Peet, and R. L. Soulsby (2004), Evaluating the performance of morphological models, *Coastal Engineering*, *51*(8-9), 917-939.

Syvitski, J. P. M., C. J. Vorosmarty, A. J. Kettner, and P. Green (2005), Impact of Humans on the Flux of Terrestrial Sediment to the Global Coastal Ocean, *Science*, *308*(5720), 376-380.

Tait, R. J. (1972), Wave Set-Up on Coral Reefs, *J. Geophys. Res.*, *77*(12), 2207-2211.

Thornton, E. B., and R. T. Guza (1983), Transformation of Wave Height Distribution, *J. Geophys. Res.*, *88*, 5925-5938.

Vitousek, S., C. H. Fletcher, M. A. Merrifield, G. Pawlak, and C. D. Storlazzi (2007), Model Scenerios of Shoreline Change at Kaanapali Beach, Maui, Hawaii: Seasonal and Extreme Events, ASCE, New Orleans, Louisiana.

von Arx, W. S. (1948), The circulation systems of Bikini and Rongelap lagoons, *Eos Trans. AGU*, *29*, 861-870.

Wang, X., and V. Swail (2006), Climate change signal and uncertainty in projections of ocean wave heights, *Climate Dynamics*, *26*(2), 109-126.

Warner, J. C., W. R. Geyer, and J. A. Lerczak (2005), Numerical modeling of an estuary: A comprehensive skill assessment, *J. Geophys. Res.*, *110*(C5), C05001.

Warner, J. C., B. Butman, and P. S. Dalyander (2008), Storm-driven sediment transport in Massachusetts Bay, *Continental Shelf Research*, *28*(2), 257-282.

Willmott, C. J., R. E. Davis, J. J. Feddema, K. M. Klink, D. R. Legates, C. M. Rowe, S. G. Ackleson, and J. O'Donnell (1985), Statistics for the evaluation and comparison of models, *J. Geophys. Res.*, *90*(C12), 8995-9005.

Wolanski, E., R. H. Richmond, G. Davis, and V. Bonito (2003), Water and fine sediment dynamics in transient river plumes in a small, reef-fringed bay, Guam, *Estuarine, Coastal Shelf Sci.*, *56*(5-6), 1029-1040.

Yang, Y., and Y.-L. Chen (2008), Effects of Terrain Heights and Sizes on Island-Scale Circulations and Rainfall for the Island of Hawaii during HaRP, *Monthly Weather Review*, *136*(1), 120-146.

Zalasiewicz, J., M. Williams, W. Steffen, and P. Crutzen (2010), The New World of the Anthropocene1, *Environ. Sci. Technol.*, *44*(7), 2228-2231.

4. Wave-driven sea level anomaly at Midway Atoll

Ron Hoeke[1,2], Jerome Aucan[3], and Mark Merrifield[4]

1. Joint Institute for Marine and Atmospheric Research (JIMAR)
   University of Hawaii and NOAA Pacific Islands Fisheries Science Center
   Honolulu, Hawaii, USA

2. School of Engineering and Physics
   James Cook University
   Townsville, Queensland, Australia

3. Bermuda Institute for Ocean Science
   St. George's. Bermuda

4. Department of Oceanography
   University of Hawaii at Manoa
   Honolulu, Hawaii, USA

Abstract

The oceanic coral atolls of the Pacific and Indian Oceans are exposed to high surface gravity wave energy. As this energy dissipates over their encircling reefs, it locally raises water levels and tends to force water flow over the reef into the lagoon. This process has been identified as the primary flushing mechanism for atolls, and the degree to which it occurs as an important determinant of lagoon water quality. Here we show not only that surface gravity waves dominate an atoll's circulation and flushing, we also show that large wave events are the primary driver of sea level anomaly (SLA) within the atoll. 60 years of (*in situ*) sea-level data at Midway Atoll (Hawaiian Islands) are compared with numerical wave hindcasts. Offshore wave forcing clearly dominates SLA in the lagoon; measured SLA is over a meter during the largest wave events. This process is further investigated by numerical simulation of SLA distribution during representative storm- and non-storm wave conditions; SLA is found to vary across the atoll interior by as much as a factor of 2. The resulting pressure gradients drive flow not only over the reef crests and out the channels, but also induce circulation within the atoll.

Concern has been raised that global mean sea-level rise will lead to inundation of low-lying atoll islands, displacing resident human populations. The research presented here suggests that these inundation events will be largely precipitated by large SLAs associated with episodic wave heights, and that the timing and severity of

these inundations will be highly dependent on both local atoll morphology and the wave climate.

4.1 Introduction

Global mean (eustatic) sea level rise (SLR) is of concern to coastal communities. In most cases, the first manifestation of SLR will be an increase in the frequency and severity of episodic inundation by short-term extreme sea-level events. Low-lying coral atolls are particularly at risk of increased episodic inundation (Church et al 2006; Dickinson 1999; Woodroffe, 2008). Most documented extreme sea-level events are along continental margins and result from storm surge primarily associated with a combination of the inverse barometer effect (IBE) and high wind-stress across continental shelves, both due to the passage of low-pressure systems, such as tropical cyclones and high-latitude storms. As we show here however, oceanic coral atolls can experience extreme sea-level events without low atmospheric pressure or strong winds in the vicinity; as they are impacted by large swells generated by distant storms. These large swells can cause significant flooding (Caldwell et al 2009; Harangozo 1992; Hoeke 2009; Oxfam 2009; White 2008), even during relatively quiescent meteorological conditions. This increase in sea-level due to waves, or wave setup, results from a transfer of momentum, i.e. the gradient of radiation stress produced as deepwater wave energy is dissipated (Longuet-Higgins & Stewart 1964; Symonds et al 1995). Breaking waves on the fore- (outward facing) reefs generate setup and usually result in cross-reef flow into the lagoon, causing an increase in sea-level in the entire lagoon (Callaghan et al 2006; Tait 1972).

This wave-driven cross-reef flow into the lagoon also has been shown to be the primary flushing mechanism of many atolls, and a primary factor influencing the lagoons residence time and water quality (Andrefouet et al 2001; Callaghan et al 2006; Kraines et al 2001; Munk & Sargent 1948). Thus the changes in the degree of wave setup and its variability has implications for lagoon water quality, sediment processes, and reef/island morphodynamics at many wave-exposed coral reef areas in the face of projected SLR.

In this paper, we investigate the non-tidal, high-frequency sea-level variations, or sea-level anomaly (SLA), as it relates to wave setup by examining 50 years of tide gauge data and two different hindcasts of wave data products at a wave-exposed atoll. We further examine processes affecting SLA within the atoll by implementing a coupled wave-flow numerical model validated with *in situ* observations. The study site, Midway Atoll, is in the Hawaiian Archipelago; it is seasonally subjected to frequent and high swell events from high-latitude storms in the north Pacific (Rooney et al 2008). The relative contribution of wave setup to SLA is estimated; the influence of intra-annual climate variations and the potential impact of SLR on both the magnitude of extreme sea-level events and lagoon flushing are discussed.

4.2 Methods

4.2.1 Study Site

Midway Atoll (28° 12′N, 177° 21′W) is a subtropical coral atoll in the Northwestern Hawaiian Islands (Figure 4.1). Despite its location near the (current) limit of coral atoll formation (Grigg 1982), it is of classic atoll morphology with a semi-circular reef crest (emergent to 0.5m deep in most places); enclosed reef flats and lagoon (1 – 12m deep); two small islands, both with maximum elevations of about 2.5 m, along the southern reef crest; and a single naturally occurring pass (~1km wide, 5m deep) on the western side. The atoll was the site of a U.S. Navy base (the World War II "Battle of Midway" occurred here) for much of the 20th Century. During this time period, parts of the lagoon were dredged and a narrow (artificial) pass created between the two main islands. Of these two islands, only Sand Island currently maintains permanent human habitation, an active airport, and a harbor, although both islands have extensive coastal armoring and other remnant infrastructure from the atoll's years as a naval base. National Oceanic and Atmospheric Administration (NOAA) maintained sea level station this study draws heavily on, is located in the atoll lagoon on the northern shore of Sand Island.

Tides in the area are of a mixed microtidal regime, with neap ranges of around 0.3 m and spring ranges around 0.6 m. Trade winds are the most prevalent throughout the year (typically 5-10 $m \cdot s^{-1}$ from the east); however due to Midway's position towards the northern edge of the north Pacific trade wind belt, trade wind events are somewhat reduced in frequency and intensity compared to more southerly locations in the Hawaiian Islands. Wave conditions associated with trade wind conditions are typically 1-3 m in height with 8-11 s periods from the east-southeast. Episodic large swells from the north-west (NW) quadrant occur during the winter, with 1-6 m waves and 10-16 s periods common; wave heights in excess of 7 m may occur several times a year. During these swell events, winds usually become westerly and rotate clockwise back to the northeast, as cyclonic low-pressure systems producing the swell pass to the north of Midway, although this is not always the case. These are the same systems that produce episodic NW swell much of the Pacific.

4.2.2 Data

In situ sea level data

The Midway Sea Level Station (SLS) currently is maintained and operated by the Center for Operational Oceanographic Products and Services (CO-OPS), NOAA. Water level data for 1947 through 2010 were obtained from the UH Sea Level Center/National Oceanographic Data Center Joint Archive for Sea Level (http://ilikai.soest.hawaii.edu/). Measurements were made using an analog mechanical gauge (1947-1974), an analog-to-digital recorder with a six-minute sampling interval (1975-1991), and an acoustic gauge recording three-minute averages every six minutes (1992-present). Data used in this study are hourly averages of these measurements.

Sea surface height deviation (SSHD)

The AVISO (http://www.aviso.oceanobs.com/duacs/) merged multi-satellite altimetry sea surface height (absolute dynamic topography product, 0.25 resolution) was obtained from the NOAA CoastWatch Program, West Coast Regional Node (http://coastwatch.pfel.noaa.gov/). This data spanned 1992-2010 and is interpreted to represent regional sea surface heights around the study site associated with mesoscale activity and wind-driven and steric changes. (Satellite data: Jason-1, Envisat, GFO, ERS-1, ERS-2 and Topex/Poseidon).

Winds and sea level atmospheric pressure (SLP)

Hourly average 10-m wind speed, maximum gust, wind directions, and sea level atmospheric (barometric) pressure measure by a surface meteorology station on Sand Island were obtained from the National Oceanic and Atmospheric Administration (NOAA) National Climate Data Center (NCDC, http://www.ncdc.noaa.gov) for years 1947-2010. Gaps in this data record were filled with four-times daily NCEP Reanalysis data (Kalnay et al 1996), provided by the NOAA Earth System Research Laboratory (ESRL, http://www.esrl.noaa.gov/psd/).

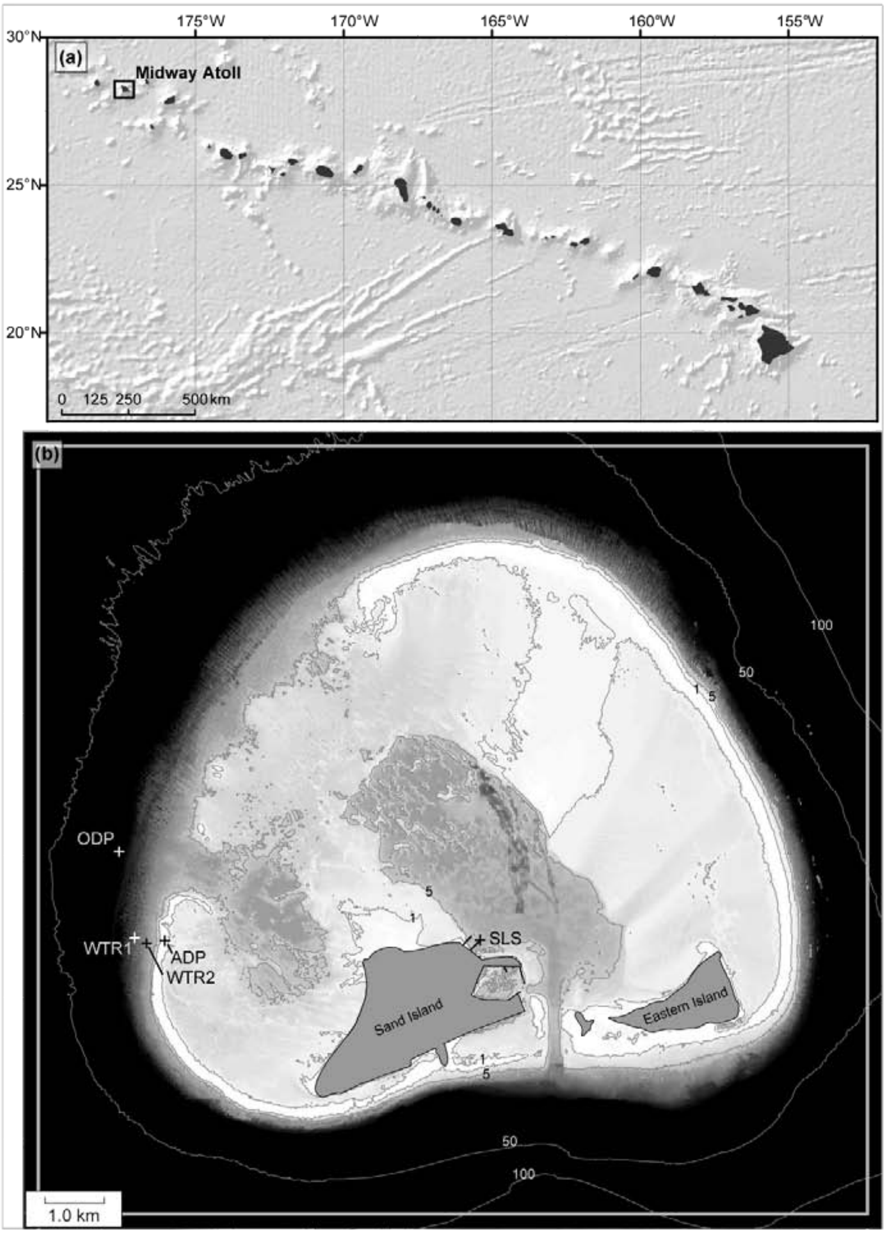

Figure 4.1: Study site. (a) Midway Atoll's location in the Hawaiian archipelago. (b) Midway Atoll with in situ observation sites indicated: "SLS" is the sea level station, see Table 4.1 for description; 100 m, 50 m, 5 m and 1 m bathymetric contours are indicated. The inner (nested) model grid boundaries is indicated by a heavy gray line on perimeter of (b).

Calculation of sea level anomaly (SLA) and inverse barometer effect (IBE)

The predicted tide was calculated by a harmonic tidal analysis of the de-trended hourly SLS timeseries (Leffler & Jay 2009; Pawlowicz et al 2002). Sea level anomaly in this paper is defined as SLA = hourly water level - predicted tide. The inverse barometer effect was calculated using the composite SLP for the study location (see above) and the world average SLP calculated from the NCEP reanalysis data.

Short term in situ observations

Two pressure sensors and two acoustic Doppler current profilers with integrated pressure sensors (ADCPs) were deployed to calibrate bed friction parameterization, empirical wave breaking, and to help validate circulation in the numerical model. Details on these instruments are given in Table 4.1, locations in Figure 4.1. The two pressure sensors (WTR1 and WTR2) and one of the current profilers (ADP) were deployed in a transect across the western forereef/reef crest to provide observations of wave dissipation and resulting setup and flow. The second profiler (ODP) provided information about the incident (deeper water) wave characteristics and to provide a measure of currents out/in the western reef pass. A cut-off frequency corresponding to periods of less than 4 s was used for the ODP due to this instrument's depth (and resulting attenuation of surface pressure fluctuations). This causes an inability to measure the higher frequency part of the wave spectrum. However, as discussed in Chapter 2, this typically accounts for only a small part of the wave energy spectrum in the Hawaiian Archipelago, and is assumed to introduce only very small errors into the calculation of bulk wave characteristics, such as significant wave height (H_s) and peak wave period (T_p).

Wave Hindcasts

In addition to the short term *in situ* observation of waves (sea below), H_s, mean wave period (T_m), and mean wave direction (D_m) were obtained from the European Centre for Medium-Range Weather Forecasts (ECMWF, http://www.ecmwf.int/) ERA Interim (1988-2010) reanalysis products (Berrisford et al 2009; Caires et al 2004). H_s, T_p, and peak direction (D_p) were also obtained from the higher resolution NOAA/NCEP Wave Watch III (Tolman 2002) hindcasts (1997-2010: WW3, http://polar.ncep.noaa.gov/waves/) for more detailed analysis of more recent conditions. Directional wave spectra from these WW3 hindcasts were also used as boundary condition for the hydrodynamic model of the atoll (see below). Wave setup within the lagoon was *a priori* assumed to be roughly proportional to wave energy flux (power); offshore unit wave power was estimated from the ERA and WW3 data using the linear wave theory definitions of energy (E) and group velocity (C_g):

$$EC_g = \frac{1}{8}\rho g H_s^{\,2}\cdot \frac{g}{\omega}\tanh(kh)\cdot \frac{1}{2}\left(1+\frac{2kh}{\sinh kh}\right) \qquad [1]$$

where g is gravitational acceleration, ρ is density of seawater h is mean water depth, and k is the wave number.

Table 4.1: Instruments deployed for model calibration. Deployments depths (*h*) and dates are given; for deployment locations, refer to Figure 4.1.

Site	Instrument	*h* (m)	dates
WTR1	Seabird Instrument SBE26p (pressure and temp.)	18.9	Sep26, 2008 – Mar19, 2009
WTR2	Seabird Instrument SBE26 (pressure and temp.)	9.7	Sep26, 2008 – Mar19, 2009
ADP	Nortek Aquadopp (2MHz current profiler w/pressure)	1.8	Sep26, 2008 – Mar21, 2009
ODP	Sontek/YSI ADP (1 MHz current profiler w/pressure)	29.0	Sep28, 2008 – Oct7, 2009

Climate indices

The monthly values of the multi-variate El Niño/Southern Oscillation (ENSO) index (MEI: (Wolter & Timlin 1998) and the North Pacific Index (PDI, (Trenberth & Hurrell 1994)) were used to investigate climate variability within the SLA and wave time series.

4.2.3 Numerical modeling

The Delft3D modeling system, a coupled flow/wave numerical solution designed for coastal applications, was selected for use in this study (Lesser et al 2004; Roelvink & Banning 1994). The flow module utilizes a finite-difference solution to the Navier-Stokes equations for unsteady flow on a three-dimensional, sigma coordinate, curvilinear grid. The wave module is built on the SWAN model, a phase-averaged solution of the discrete spectral balance of wave action density (Booij et al 1999; Ris et al 1999). The two modules are iteratively coupled so wave information from the wave module is passed to the flow module to compute mass transport by Stokes drift and wave forces due to radiation stress gradients, the subsequent water levels and currents are passed back to the wave module for use in calculating an updated wave field, and so on. A summary of model development is presented below.

Computational grid and boundary conditions

An outer 1 km spatial resolution rectangular Cartesian coordinate grid was constructed to incorporate all areas of Midway Atoll with depths < 250 m. A smaller inner Cartesian grid with 62.5 m spatial resolution was nested inside the larger grid such that the distance between the grid boundary to the atoll reef rime was ~1.5 km and all depths < 50 m were incorporated.

Lateral wave boundary conditions were applied to the outer grid, so that wave transformations in the 250-50 m depth range could be estimated before being passed to the inner, nested grid; these outer boundaries consisted of WW3 directional spectra for the WW3 grid point coinciding with Midway Atoll (the atoll is not resolved in the WW3 model). Lateral flow boundary conditions were applied along the inner grid, which consisted of uniform water levels on all four sides. These uniform water levels were calculated by summing predicted tide+SSHD+IBE. While in reality some water level gradient(s) undoubtedly exists at all times along the offshore boundaries, it is assumed that they are small compared to water level gradients across the atoll (within the inner grid interior) and therefore the uniform boundary assumption leads to relatively small errors in the processes of interest.

The Midway meteorology station provided 10-m height wind input. These hourly observations were applied uniformly over both the wave and flow model domains.

Bathymetry in the model was derived from a combination of multibeam bathymetry (varying spatial resolution, approx. 1-20 m [Miller et al 2003]) and satellite visible band reflectance derived pseudobathymetry in shallow areas (spatial resolution 4 m [Miller et al 2003; Stumpf et al 2003]). While Stumpf et al [2003] suggests a normalized rms error of 0.3 (30%) for the satellite pseudobathymetry, this may be worse in some areas than others, and 30% differences between estimated and real water depth may results in very large differences in calculated and real volume flux and other processes along the shallow atoll rim. This remains a largely unknown source of error in this study, as no better bathymetry data is available.

Chapters 2 and 3 as well as other studies [Hearn 1999; Lowe et al 2005] demonstrate a magnitude of difference between reef and unconsolidated sediment (sand) bottom boundary layer hydraulic roughness values. These areas were differentiated with satellite-derived benthic habitat maps (Holderied et al 2002) acquired from NOAA's National Centers for Coastal Ocean Science (NCCOS). Wave and flow hydraulic roughness length scales were varied from a minimum of 0.01 m in sandy areas to 0.20 m in reef and hard bottom areas; the higher range of these values (0.10-0.20 m) suggested for coral reefs from the previous studies. These values were calibrated in the models to best match the observations.

Model parameterization and validation

SWAN model simulations were conducted with wave spectra resolved for 25 logarithmic bins from 0.04 to 1 Hz ($\Delta\sigma/\sigma = 0.1$), directional resolution was set at $\Delta\theta = 3^{\circ}$, and simulations with and without phase-decoupled estimated diffraction [Holthuijsen et al., 2003]. Wave dissipation due to bottom friction was based on (Madsen et al 1988) using the hydraulic roughness values discussed above. SWAN uses the periodic bore model of (Battjes & Janssen 1978) to estimate dissipation due to wave breaking. The empirical proportionality constant of dissipation (α) the breaker height coefficient (γ_b) used in the breaker model were set to a value of 1 and 0.9, respectively, based on (Massel & Gourlay 2000).

The flow calculations were solved using a depth integrated, 2D implementation with the White-Colbrook formulation (Colebrook 1939) used to estimate bottom boundary layer structure. Horizontal eddy viscosity was varied between 0.1 and 1 m^2 s^{-1}; based on values observed or used for other coral reefs (Kraines et al 1998; Lowe et al 2009).

Three periods within the range of available short term *in situ* data were selected for modeling: a large NW swell episode (offshore H_s up to 8.2 m), Jan12 – 17, 2009; a relatively moderate NW swell episode (H_s up to 5.1 m), Nov10 - Nov15, 2008; and a moderate to energetic trade wind period (offshore H_s varying between of 2 and 3.8 m), Nov15 – Nov21, 2008. These periods were used to investigate the processes driving the positive SLA observed at the SLS and the ADP site and the distribution of these anomalies across the atoll. The normalized skill score termed the "index of agreement" by (IAS [Willmott et al 1985]), comparing scalar model predictions to *in situ* observations, was used to evaluate and calibrate the model. This index of agreement skill (IAS) is defined as:

$$IAS = 1 - \frac{\sum (predictions - observations)^2}{\sum \left(\left| predictions - \overline{observations} \right| + \left| observations - \overline{observations} \right| \right)^2} \qquad [2]$$

A skill value of one corresponds to a 100% agreement between model prediction and observations, while decreasing values indicate decreasing agreement, or poorer model performance. See (Lowe et al 2009; Sutherland et al 2004; Warner et al 2008; Willmott et al 1985) for further discussion of model skill and examples of metric used to evaluate numerical models.

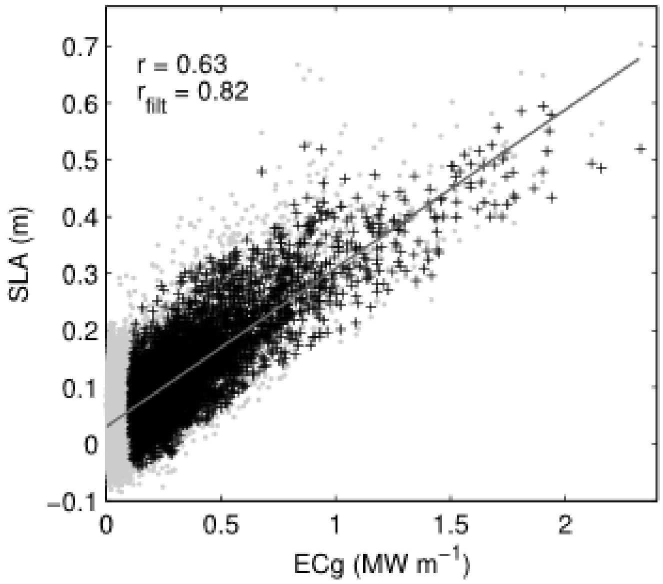

Figure 4.2: SLA at the Midway sea level station versus offshore wave energy flux (EC_g) calculated from NOAA/NCEP WaveWatch III numerical hindcasts, 1997-2010. Grey points represent all data; black points correspond to times when H_s>3m and SLA with a 6-hour low pass filter, smoothing stochastic SLA fluctuations not observed in the wave hindcast data.

4.3 Results

Comparison of offshore wave energy flux (EC_g) with SLA reveals a significant correlation (r = 0.62), particularly during time periods of larger waves (r = 0.82, Figure 4.2). SLA may exceed 0.5 m when EC_g exceeds 1 MW m^{-1}, corresponding to H_s of approximately 9 m and T_p of 10-12 s.

To inspect the relative seasonal contribution of IBE, wind stress, SSHD, and EC_g, to SLA, a linear regression is examined for each month of the year. A multiple linear regression of all variables describes 85-95% of the variance of SLA throughout the year (Figure 4.3a). However the variance explained by each variable separately differs drastically over the course of the year. In the (boreal) winter months of December through February, EC_g describes 65-75% of the observed variance in SLA. This drops to less than 20% in the summer months. The influence of IBE explains 50-60% of the variance during the winter months, dropping to a minimum of 19% in summer (Figure 4.3a). During summer months, SSHD dominates the signal,

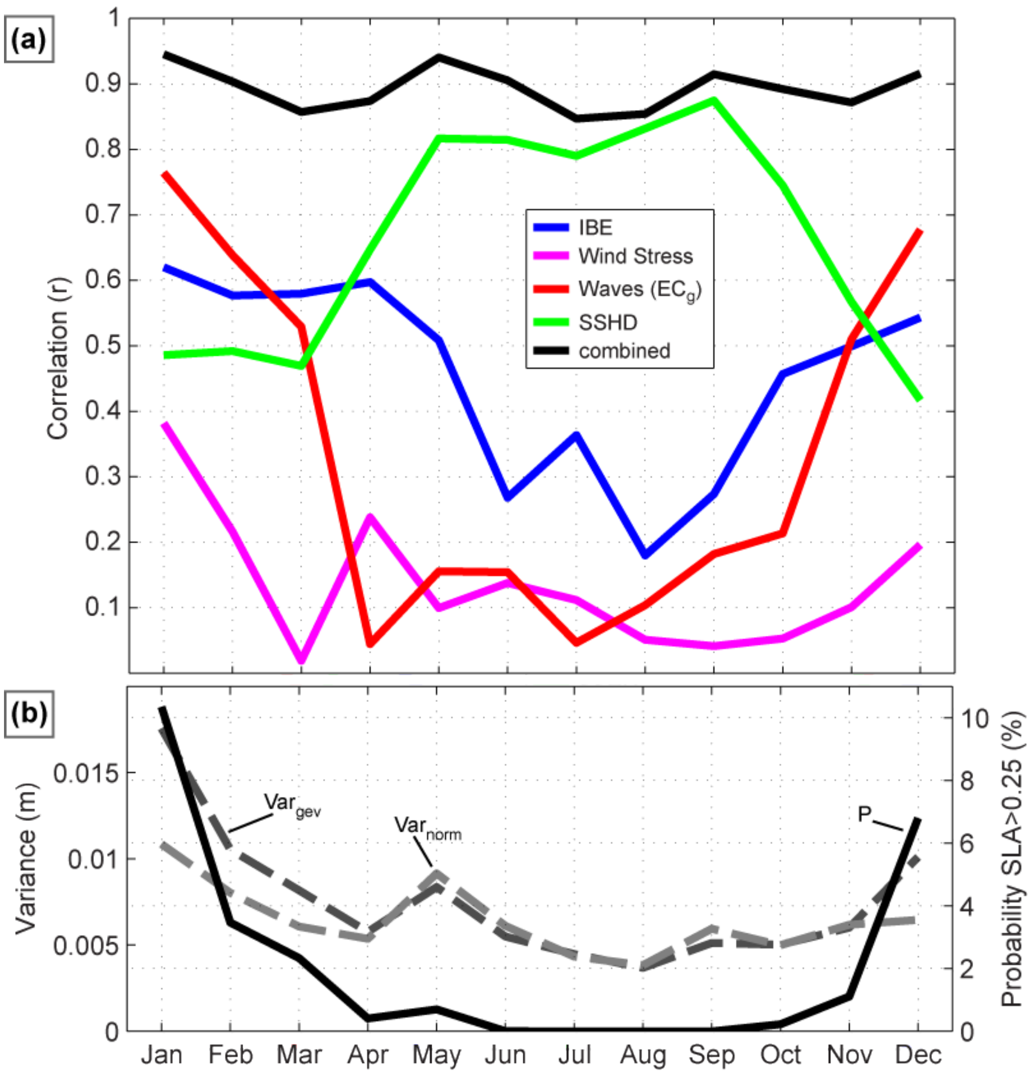

Figure 4.3: (a) Monthly correlation coefficients resulting from linear regression of SLA and inverse barometer effect (IBE), wind stress, wave energy flux (EC_g) and satellite sea surface height deviation (SSHD), as well multiple linear regression of all four variables ("combined"). (b) Monthly variance of SLA based on a normal fit (Var_{norm}) and a generalized extreme value (GEV) fit (Var_{gev}); the probability (P) of SLA exceeding 0.25 m on any given day during each month (in percent), based on a GEV fit, is also included.

explaining greater than 80% of SLA variance.

Based on all available sea level data from 1947-2010, variance in January is around a factor of 3 higher than in August (Figure 4.3b). This is largely driven by extreme positive SLA events: the probability of SLA exceeding 0.25 m at any time during the month of January is 10%, while in the probability in the months of June – August is much less than 0.01% (Figure 4.3b). These large seasonal changes in SLA correlation to forcing mechanisms (waves, IBE, and SSHD) are linked to the strong seasonal differences in overall of SLA magnitudes (variance). Based on all available sea level data from 1947-2010, variance in January is around a factor of 3 higher than in August (Figure 4.3b). This is largely driven by extreme positive SLA events: the probability of SLA exceeding 0.25 m at any time during the month of January is 10%, while in the probability in the months of June – August is much less than 0.01% (Figure 4.3b).

These seasonal changes in SLA variability can be explained by examining the study region's wave climate (Figure 4.4). In the summer H_s averages less than 2 m; while mean wintertime H_s is 3-4 and the total range is far greater in winter, with mean monthly maximums in the range of 7–8 m in December and January (Figure 4.4a). These large winter swells come primarily from the northwest, with T_p of 10-14 s, indicating they come from mid-latitude cyclones associated with the Aleutian low (Bromirski et al 2005; Chapter 2 and 3). During summer, the smaller waves tend to be from the east-south-east with T_p in the range of 6-10 s, indicating they are associated with the North Pacific trade wind belt (Midway is near the northern edge) and more locally generated (Chapter 2 and 3; Rooney et al 2008). Weak SLA variability in the summer appears to have less to do with trade wind waves than with changes in regional sea level, perhaps associated with mesoscale oceanographic eddies (e.g., (Firing et al 2004)) and other non-wave related processes. In winter, the large episodic swells associated with the passage of low pressures systems (usually well to the north), cause the SLA signal to be dominated by wave setup and IBE becomes more important, especially in the spring transition months.

The transformation of large winter swell at the Midway atoll is examined using numerical simulations for one of the large winter swell events that occurred

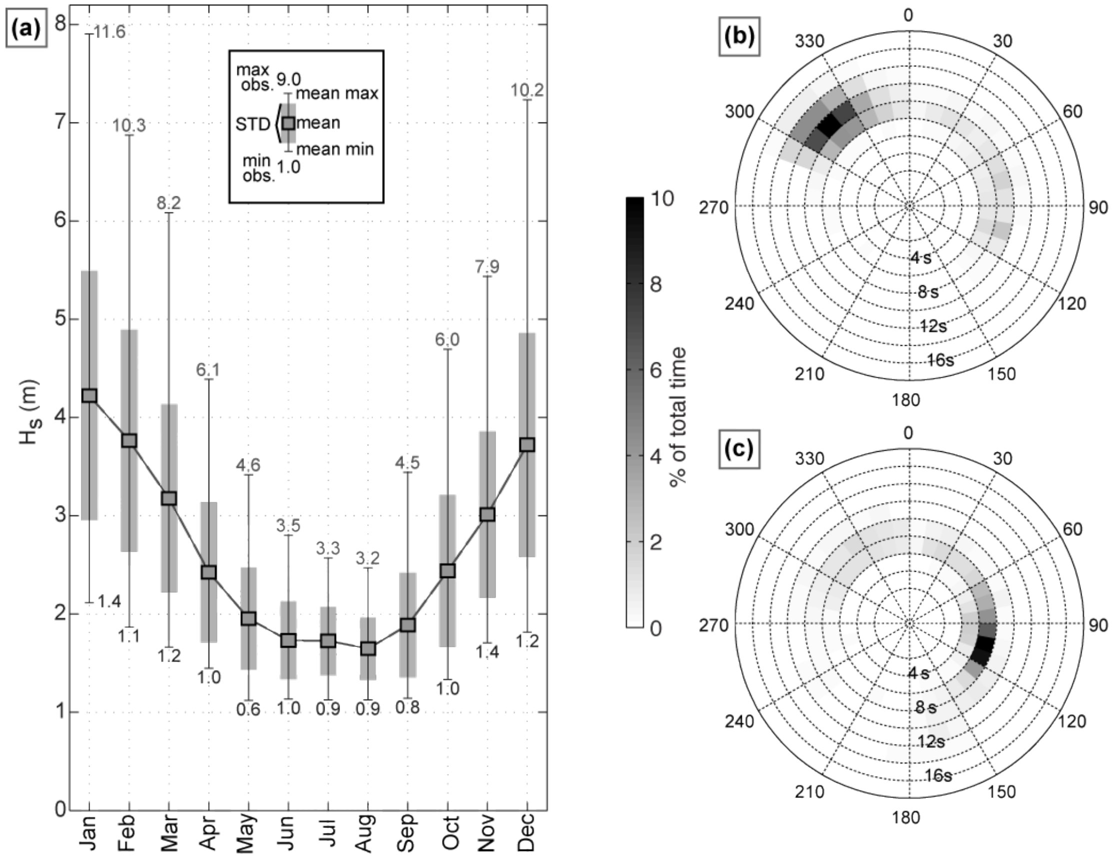

Figure 4.4: Wave Climatology, Midway Atoll: (a) monthly mean, standard deviation, mean monthly min/max and total observed min/max significant wave height (H_s) from model hindcast data from 1996 to 2010 (WW3); (b) mean frequency that peak direction (θ_p) and peak period (T_p) occurs in each 5° θ_p (from 0 - 360°, nautical convention) and 2s (from 2-18s) T_p bin in the hindcast data for the months of November – March; (c) same as (b), but for the months of May – September. Events occurring during the months of April and October, transition months, are omitted from (b) and (c) for clarity.

during the three selected modeling periods (Figure 4.5a). The event peaked on January 13, 2009, with a maximum offshore H_s of 8.3 m estimated by WW3. The rapid dissipation of the wave energy due to wave breaking over the steep slopes just offshore of the atoll rim is apparent. Waves in the atoll lagoon are generally less than 1 m, except near the more exposed western side of the atoll, particularly in the vicinity of the western channel. Wave refraction occurs around the atoll topography, and wave heights in the immediate lee of the atoll are reduced to 1-3m (Figure 4.5a).

As a result of wave dissipation around the atoll rim, the entire lagoon is setup with SLA ranging from 0.4 to 0.7 m. SLA over most of the lagoon is 0.5m. Wave-driven setup peaks in amplitude (>0.7m) at some of the more exposed and shallow parts of the atoll rim on the west and north sides. The modeled wave-driven flows tend to be directed along isobaths over the fore-reef on the north and west sides of the atoll, with weak fore reef flows in the lee. Inside of the main breaker zones on the north west sides of the atoll, flows on the order of 0.5 $m{\cdot}s^{-1}$ are directed into the lagoon over the rim, with some evidence of weak (<0.1 $m{\cdot}s^{-1}$) flow out of the lagoon on the leeward side. Strong flow out of the atoll occurs at the two main reef channels on the west and south sides of the atoll, with (depth averaged) speeds reaching 0.8 $m{\cdot}s^{-1}$ and 1.9 $m{\cdot}s^{-1}$, respectively.

The wave-forced model simulations are compared to the *in situ* observations for the three selected periods (Figure 4.6 and Table 4.2). There is close correspondence between modeled and *in situ* Hs at the WTR1 site, and modeled and *in situ* SLA at the ADP site and the SLS during the two NW swell events (Jan 12-17, 2009 and Nov 10-15, 2008), with other drivers of SLA (IBE and SSHD) exhibiting minimal influence. This is not the case during the modeled trade wind conditions (Nov 15 – 21, 2008), when the SLA trend does not appear to follow the less energetic and slowly varying trade wind wave heights, and instead appears to be dominated by the combined IBE and SSHD signal (Figure 4.6i). Simulated current magnitudes fell within the scatter of observations during all three modeling periods at the ADP site (Figure 4.6d,g, and j); both simulated and observed flows were consistently inward, perpendicular to the reef crest at this site (not shown). Curiously, the magnitude of flow, both simulated and observed, does not follow the trend in incident wave height for the large NW swell event (Jan 12-17, 2009), as it does for the other two modeling periods. Instead, it levels off at a maximum of approximately 0.6 $m{\cdot}s^{-1}$ after an abrupt rise. This suggests there may be some threshold for the magnitude of cross-reef flow, possibly due to some combination of hydraulic roughness of the reef crest and hydraulic head within the lagoon. The details of this phenomenon are not further considered in this work.

The maximum wave setup calculated by a relatively simple analytic solution for wave driven flow over a reef [Symonds et al 1995)] is also included for comparison with SLA at the ADP site (Figure 4.6 and Table 4.2), which is close to the local spatial maximum SLA at the reef crest during the two modeled NW swell periods. While this 1-dimensional solution cannot account for the two-dimensional reality of spatial

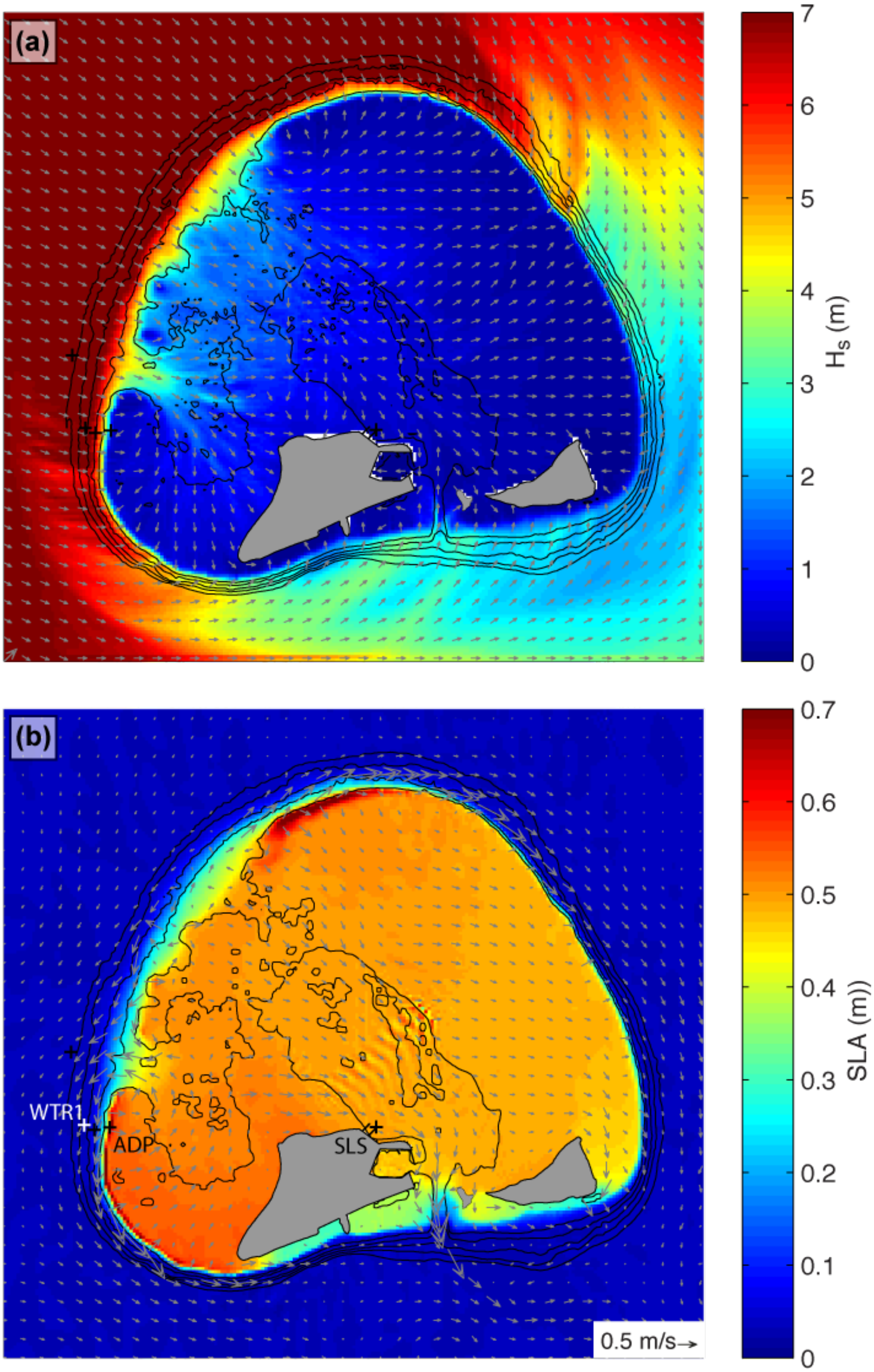

Figure 4.5: Numerical model output during a large NW swell, January 13, 2009, 15:00. (a) Significant wave height (H_s), peak direction (D_p) is indicated with arrows. (b) Sea level anomaly (SLA) with scaled arrows indicating current vectors. In both (a) and (b) the locations of available in situ observations is given by black crosses, including the location of the Midway sea-level station (SLS); bathymetric contours every 5 m from 25 to 5 m are indicated with black lines; the spatial resolutions of arrows (vectors) are decimated by a factor of 6 to ease interpretation.

variation in SLA, the solution's maximum wave setup is within approximately 0.05 m of observed SLA during the smaller NW swell event (Nov 10-15, 2008) and the trade wind event (Nov 15-21, 2008). The analytic solution overestimates water levels by almost 0.2 m during the larger NW swell event (Jan 12-17, 2009). This may be due to the aforementioned possible threshold in cross-reef flow of the analytic solution use of a linear approximation of friction (as opposed to the numerical solutions use of quadratic friction).

Minimum and maximum instantaneous flushing times (T_f), analogous to the "renewal time" discussed by (Andrefouet et al 2001), provide an estimate of overall mean atoll residence time under different conditions (Table 4.2). In this study, T_f is defined as the volume of water within the perimeter of the atoll (V) divided by the mean depth-inegrated flux of water into and out of the perimeter (Q, e.g. $T_f = V/Q$). Q is calculated from the current fields of the numerical model, with the location of the perimeter definded by the shallowest part of the reef rim . For an explicit description of this volume flux-based method of estimating residence times and its limitations, see (Monsen et al 2002)). The minimum T_f during the two modeled NW swell periods are a factor of 2-3 times shorter than the two periods maximum T_f , as well as the T_f at any time during the trade wind period. These greatly decreased flushing times indicate that the observed wave-driven positive SLA events are associated with episodic flushing of materials from the atoll's interior.

Overall values for model skill are calculated by averaging IAS values resulting from all available *in situ* observations of H_s, SLA, and current magnitudes ($|U|$) with model data (Table 4.2). These values are similar to those considered acceptable by other researchers using coupled wave-flow models (Lowe et al 2009; Malhadas et al 2009; Warner et al 2005), although the model skill for the larger of the two NW swell periods is noticeably poorer than the smaller NW period or the trade wind period. This may be due to limitations in using input wave data (WW3) to characterize extreme wave events (e.g. (Hanson et al 2006)), and/or performance issues with the coupled model for energetic hydrodynamic conditions.

The annual number of wave events with peak wave energy flux (EC_g) greater than 0.4 MW m^{-1} (roughly equivalent to H_s = 5 m, T_p = 14 s) for the years 1988-2010,

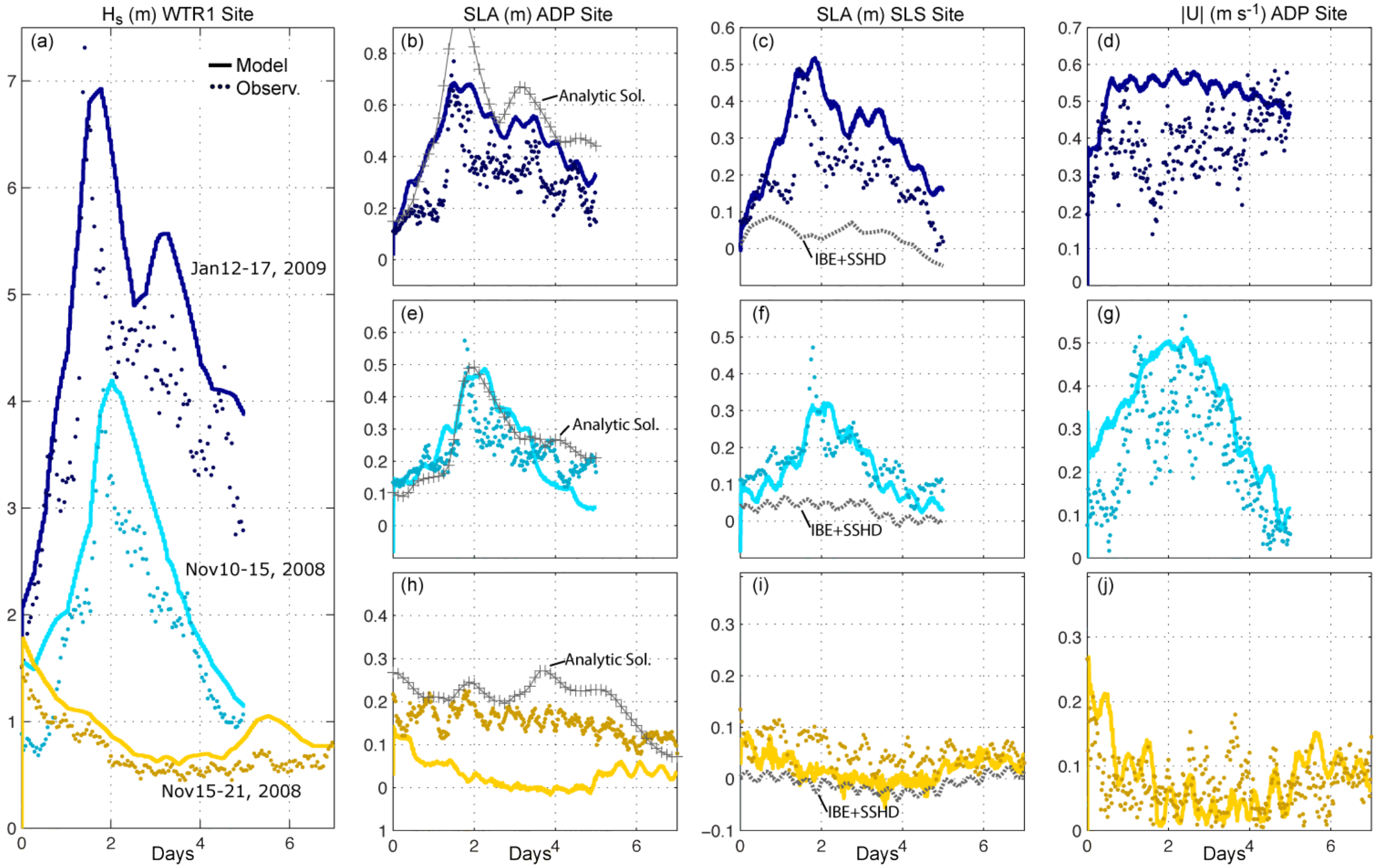

Figure 4.6: Model and observed significant wave height (H_s), sea-level anomaly (SLA), and depth-averaged cross-reef current magnitude (|U|) for the three selected modeling periods. All x-axes indicate days from the start of the respective modeling period. (a) H_s for all three for the three modeling periods at the WTR1 site. (b) SLA at the ADP site; (c) SLA at the SLS site; (d) and |U| at the ADP site for the modeling period Jan 12-17. (e-g) and (h-j) are for the same variables as (b-d) but for modeling periods Nov 10-15, 2008 and Nov 15-21, respectively. In the SLA at the ADP site plots (b,e,h), the analytic solution for maximum wave setup (Symonds et al 1995) is plotted for reference. In the SLA at the SLS site plots (c,f,i), the inverse barometer effect (IBE) on water level, combined with the sea surface height deviation (SSHD), is also plotted for reference.

Table 4.2: Summary of conditions and model calculations during the three periods selected for numerical modeling. Columns are defined as follows: The wave parameters "Max H_s", "Max T_p", and "Max D_p" are the maximum offshore significant wave height and the peak period and direction coincident with " max H_s" for each model period (from WW3); "Max SLA: ADP site" and "Max SLA: SLS site" are the maximum sea-level anomaly (SLA) observed or calculated at these two respective sites, where "model", "obs.", and "analy." are the SLA calculated by the numerical model, (*in situ*) observed, and the maximum calculated by (Symonds et al 1995)'s analytic solution, respectively. " "Flushing time" is the minimum and maximum volume flux based instantaneous residence time of the entire atoll (T_f), over the course of each model run, and "Model skill" is the overall mean index of agreement (IAS) resulting from the comparison of all available in situ observations of Hs, SLA, and current magnitudes with model data.

model period	max H_s (m)	max T_p (s)	max D_p (°)	Max SLA: ADP site (m)			Max SLA: SLS site (m)		Flushing time (hours)		Model skill
				model	obs.	analy.	model	obs.	min	max	
Jan12 - 17, 2009	8.3	15.9	305.8	0.686	0.769	0.973	0.518	0.488	8.6	27.5	0.73
Nov10 - 15, 2008	5.1	14.2	314.0	0.487	0.574	0.492	0.321	0.471	12.5	28.5	0.91
Nov15 - 21, 2008	3.8	8.5	99.6	0.141	0.225	0.271	0.090	0.134	20.5	38.3	0.82

calculated from the ERA Interim reanalysis, is presented in Figure 4.7a. The correlation between the annual number of these extreme wave events and annual SLA events greater than 0.3 m is 0.75; if annual extreme wave events are calculated from WW3, the correlation rises to 0.95, suggesting that ERA Interim may underestimate or omit some extreme wave events. However, because the available WW3 time period (years 1997-2010) is short and does not fully include the strong El Niño years of 1997-1998, the ERA Interim wave events are used for comparison to the climate indices MEI and winter NPI. Significant interannual variability exists in the annual number of extreme wave events, which appears to be connected to the climate indices (Figure 4.7a). All cases of four or more extreme wave events occur only when the MEI is positive and NPI is negative (Figure 4.7a). Bivariate linear regression of MEI and NPI on the annual number of extreme wave events provides a significant correlation of 0.62.

4.4 Summary and Discussion

The observed SLA signal within the perimeter of the reef crest at Midway Atoll is seasonally dominated by wave setup, with large SLA events (greater than around 0.25 m) occurring on average 7-8 times each winter (Figure 4.3b). The events are coincident with open ocean swell heights of around 4 m or greater arriving from the northwest. The typically long period of these swells (10-16s, Figure 4.4b), combined with the fact that they do not necessarily coincide with a local variation in barometer pressure (e.g. Figure 4.6c and f), indicate that the center of atmospheric low pressure and the associated wind fields creating these swell events may be on the order of thousand of kilometers distant. This is consistent with the genesis of most large swell events impacting Midway by mid-latitude cyclones; the mean location of the highest density of these storms' tracks lies approximately between 40°N and 50°N latitude (Rodionov et al 2007), 1500 km north of Midway.

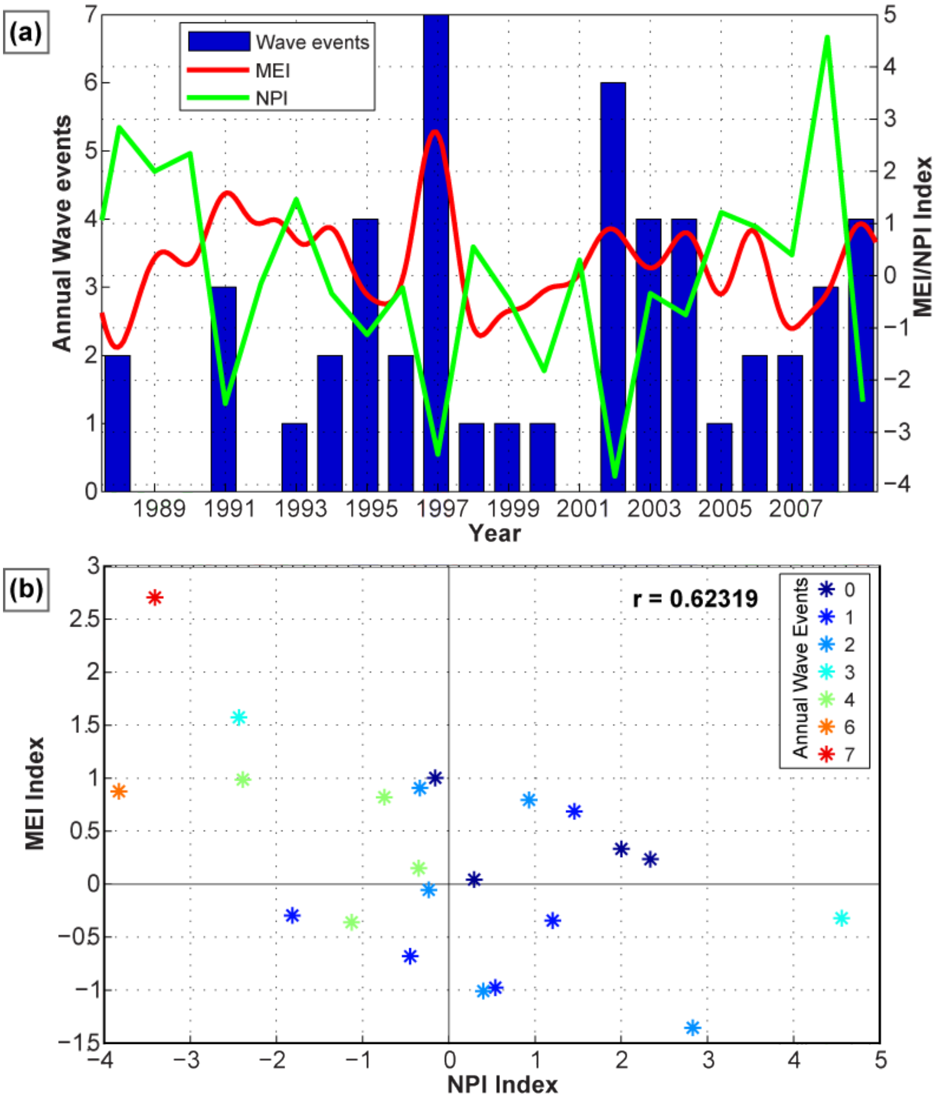

Figure 4.7: (a) The annual number of waves events with a deep water energy flux>0.4 MW m^{-1} at Midway Atoll (estimated from the ECMWF Interim Reanalysis); the Multi-variate ENSO Index (MEI, [Wolter & Timlin 1998]) and the NDJFM North Pacific Anomalies Index (NPI, [Trenberth & Hurrell 1994]) are also plotted for comparison. (b) The co-variance of the annual number of wave events with MEI and NPI. The correlation coefficient (r) is from the multiple linear regression of the annual number of wave events with MEI and NPI as predictors.

The wave-flow coupled numerical model used in this study predicted observed SLA to within approximately 30% at worst, and within 10% at best at two different sites within the atoll (Table 4.2 and Figure 4.6), and revealed large morphology-dependent spatial variation in wave-setup/local water levels (up to 0.7 m) across the atoll (Figure 4.6). The maximum wave setup calculated by a 1-dimensional analytic model (Symonds et al 1995) performed similarly for observations near the reef crest exposed to incident waves, but could not account for sea-level variations across the atoll away from the reef crest. The analytic model also tended to over-estimate large events and under-estimate small events (Table 4.2 and Figure 4.6); this may be due to the use of linear friction terms (as opposed to the quadratic formulation of the numerical model) in the analytic model (Gourlay & Colleter 2005; Symonds et al 1995), or the possibility of a maximum threshold in cross-reef flow due to hydrodynamics not accounted for in the analytic solution. Input wave data for both models (boundary conditions), were likely a significant source of error, as hourly variations in SLA were often large, while the hindcast data used as boundary conditions (WW3) was available only every three hours.

The high dependence of (modeled) overall atoll flushing times and (modeled and observed) currents on offshore wave height and subsequent water levels across the atoll (Table 4.2, Figure 4.5, Figure 4.6) suggests that the number and intensity of high wave events are key controls to water quality and the (episodic) transport of sediment and other materials, into, out of, and within the atoll. Given the large inter-annual variability of wave events (Figure 4.7), water quality, sedimentation, and risk of atoll island inundation are likely dynamic on annual and greater timescales, as recent geological work suggests (Webb & Kench 2010; Woodroffe 2008). The correlation of the annual number of extreme swell events impacting Midway and the MEI and North Pacific Index (e.g. Figure 4.7), suggests that climate indices may provide a useful tool for assessing SLA climatology.

4.5 Conclusions

The wave setup events identified at Midway Atoll in this study are as large, if not larger, than previously identified drivers of SLA at tropical Pacific islands. Wave setup, as measured by the sea level station at Midway, is on the order of +0.25 m and greater than +1 m has occurred several times in the ~60 year record; the inverse barometer effect of atmospheric pressure and sea surface height deviation due to mesoscale oceanographic features (e.g. Rossby waves) is on the order of ±0.05 m;

ENSO interannual variability, though not a large factor at high-latitude Midway, may be up to ±0.2 m in the equatorial Pacific (Church et al 2006). While Midway, with its exceptionally high latitude for a coral atoll (28.2°N), may experience an especially energetic wave climate, long period swells generated by high-latitude storms in both hemispheres, as well as tropical cyclones, propagate throughout much of the Pacific, and thus most likely impact sea-level signals at many locations. Examples include locations within the Tuamotus, the Cook Islands, Kiribati, Tuvalu, Micronesia and the Marshall Islands in the Pacific Ocean and the Maldives in the Indian Ocean. The magnitude and interannual variability of wave setup events may introduce a large and currently unaccounted for uncertainty in contemporary sea-level analyses of tide gauges e.g. (Church et al 2006; Firing et al 2004; Woodworth et al 2009) at such locations.

Traditional coastal inundation risk assessment typically identifies “storm surge”, usually composed primarily of wave runup, wind stress setup and inverse barometer effect associated with a storm in the immediate vicinity, as the driver of coastal inundation events (e.g. (McInnes et al 2009; Thompson et al 2009)). This may be applicable to continental margins, however this research shows that wave-driven SLA events with the potential for island inundation may occur at oceanic coral atolls when the nearest storm is thousands of kilometers distant. Inundation of low lying islands, some severe, has been documented throughout the Pacific and in the Indian Oceans when distant source, long-period ocean swells coincide with local astronomical high tides (Caldwell et al 2009; Harangozo 1992; Hoeke 2009; Oxfam 2009; White 2008).

The historical analysis and modeling tools utilized in this study allow for the effect of wave setup to be examined and predicted to within a reasonable degree of accuracy. The input wave data used here, WW3, provides forecasts up to 180 hours, allowing for prediction of potential inundation events due to wave setup. However, the modeling results also indicate that large spatial variations in the magnitude of setup can be expected both within an individual reef system and between neighboring reefs; (Andrefouet et al 2001) found significant variation in residence times and related wave (setup) driven flows within the Tuamotu Archipelago. Therefore vulnerability of islands to flooding is likely highly dependent on reef morphology, island locations within the atoll, and local wave climate. Detailed setup predictions require coupled wave-flow numerical models with horizontal spatial resolution on the order of 50m (such as the one used here). These models depend on accurate bathymetric measurements of the entire atoll, which currently are not available at many of the remote atolls throughout the Pacific and Indian Oceans.

While recent evidence suggests that atoll islands may exhibit greater resilience to permanent inundation from eustatic sea-level rise than previously thought (through dynamic geomorphic response, e.g. Webb & Kench [2010]), increased rates of sea level rise will surely result in increased frequency and severity of short term inundation events, and the nature of this geomorphic response will depend on the hydrodynamics of the inundation events. Implementation of numerical models such as the one presented in this paper may be a necessary first step in predicting the geomorphic response of low lying islands in the Pacific and Indian oceans to projected increases in eustatic sea-level.

4.6 Acknowledgments

This work was primarily supported by the NOAA Coral Reef Conservation Program, with additional support from the Australia Institute of Marine Science AIMS@JCU program.

ECMWF ERA-Interim data used in this study/project have been provided by ECMWF.

The altimeter products were produced by *Ssalto*/*Duacs* and distributed by *Aviso*, with support from *Cnes* (http://www.aviso.oceanobs.com/duacs/).

4.7 References

Andrefouet S, Pages J, Tartinville B. 2001. Water renewal time for classification of atoll lagoons in the Tuamotu Archipelago (French Polynesia). *Coral Reefs* 20:399-408

Battjes JA, Janssen JPFM. 1978. Energy loss and set-up due to breaking of random waves. *16th International Conference Coastal Engineering*, pp. 563-87. Hamburg, Germany: New York, NY: ASCE

Berrisford P, Dee D, Fielding K, Fuentes M, Kallberg P, et al. 2009. The ERA-Interim archive, ECMWF, Reading

Booij N, Ris RC, Holthuijsen LH. 1999. A third-generation wave model for coastal regions, Part I, Model description and validation. *J. Geophys. Res.* 104:7649-66

Bromirski PD, Cayan DR, Flick RE. 2005. Wave spectral energy variability in the northeast Pacific. *J. Geophys. Res.* 110

Caires S, Sterl A, Bidlot J-R, Graham N, Swail V. 2004. Intercomparison of Different Wind–Wave Reanalyses. *J. Clim.* 17:1893-913

Caldwell PC, Vitousek S, Aucan JP. 2009. Frequency and Duration of Coinciding High Surf and Tides along the North Shore of Oahu, Hawaii, 1981‚Äì2007. *J. Coastal Res.* 25:734-43

Callaghan DP, Nielsen P, Cartwright N, Gourlay MR, Baldock TE. 2006. Atoll lagoon flushing forced by waves. *Coastal Engineering* 53:691-704

Church JA, White NJ, Hunter JR. 2006. Sea-level rise at tropical Pacific and Indian Ocean islands. *Global and Planetary Change* 53:155-68

Colebrook CF. 1939. Turbulent flow in pipes with particular reference to the transition region between the smooth- and rough-pipe laws. *Journal of the Institution of Civil Engineers* 11

Dickinson WR. 1999. Holocene Sea-Level Record on Funafuti and Potential Impact of Global Warming on Central Pacific Atolls. *Quaternary Research* 51:124-32

Firing YL, Merrifield MA, Schroeder TA, Qiu B. 2004. Interdecadal Sea Level Fluctuations at Hawaii. *Journal of Physical Oceanography* 34:2514-24

Gourlay MR, Colleter G. 2005. Wave-generated flow on coral reefs--an analysis for two-dimensional horizontal reef-tops with steep faces. *Coastal Engineering* 52:353-87

Grigg R. 1982. Darwin Point: A threshold for atoll formation. *Coral Reefs* 1:29-34

Hanson JL, Tracy BA, Tolman HL, Scott D. 2006. Pacific hindcast performance evaluation of three numerical wave models. *9th International workshop on Wave Hindcasting and Forecasting. Victoria, Canada*

Harangozo SA. 1992. Flooding in the Maldives and its implications for the global sea level rise debate. In *Sea Level Changes: Determination and Effects*, ed. PL Woodworth, DT Pugh, JG DeRonde, RG Warrick, J Hannah, pp. 95-9: American Geophysical Union

Hearn CJ. 1999. Wave-breaking hydrodynamics within coral reef systems and the effect of changing relative sea level. *J. Geophys. Res.* 104:30,007–30,19

Hoeke R. 2009. NOAA Ship Hi`ialakai. Cruise Report No. CRHI0901, National Oceanic and Atmospheric Administration (NOAA) Pacific Islands Fisheries Science Center Honolulu, Hawai'i

Holderied K, Stumpf RP, Rohmann SO, Shapiro A, Anderson M, Smith W. 2002. Benthic habitat mapping of Pacific Ocean coral reefs with high-resolution satellite imagery. *Seventh International Conference on Remote Sensing for Marine and Coastal Environments*. Miami, USA

Kalnay E, Kanamitsu M, Kistler R, Collins W, Deaven D, et al. 1996. The NCEP/NCAR 40-Year Reanalysis Project. *Bull. Am. Meteorol. Soc.* 77:437-71

Kraines S, Isobe M, Komiyama H. 2001. Seasonal variations in the exchange of water and water-borne particles at Majuro Atoll, the Republic of the Marshall Islands. *Coral Reefs* 20:330-40

Kraines S, Yanagi T, Isobe M, Komiyama H. 1998. Wind-wave driven circulation on the coral reef at Bora Bay, Miyako Island. *Coral Reefs* 17:133-43

Leffler KE, Jay DA. 2009. Enhancing tidal harmonic analysis: Robust (hybrid L1/L2) solutions. *Continental Shelf Research* 29:78-88

Lesser GR, Roelvink JA, van Kester JATM, Stelling GS. 2004. Development and validation of a three-dimensional morphological model. *Coastal Engineering* 51:883-915

Longuet-Higgins MS, Stewart RW. 1964. Radiation stresses in water waves; a physical discussion, with applications. *Deep Sea Research* 11:529-62

Lowe RJ, Falter JL, Bandet MD, Pawlak G, Atkinson MJ, et al. 2005. Spectral wave dissipation over a barrier reef. *J. Geophys. Res.* 110:16

Lowe RJ, Falter JL, Monismith SG, Atkinson MJ. 2009. A numerical study of circulation in a coastal reef-lagoon system. *J. Geophys. Res.* 114:C06022

Madsen OS, Poon Y-K, Graber HC. 1988. Spectral wave attenuation by bottom friction: Theory. *Proceedings of 21th International Conference on Coastal Engineering, Am. Soc. of Civ. Eng.*, pp. 492–504. New York

Malhadas M, Neves R, Leitão P, Silva A. 2009. Influence of tide and waves on water renewal in Óbidos Lagoon, Portugal. *Ocean Dynamics* 60:41-55

Massel SR, Gourlay MR. 2000. On the modelling of wave breaking and set-up on coral reefs. *Coastal Engineering* 39:1-27

McInnes K, Macadam I, Hubbert G, O'Grady J. 2009. A modelling approach for estimating the frequency of sea level extremes and the impact of climate change in southeast Australia. *Natural Hazards* 51:115-37

Miller J, Hoeke R, Appelgate B, Johnson P, Smith J. 2003. Bathymetric Atlas of the Northwestern Hawaiian Islands - A Planning Document for Benthic Habitat Mapping - Draft, May 2003. In *http://crei.nmfs.hawaii.edu/BathyAtlas/*: NOAA

Monsen NE, Cloern JE, Lucas LV, Monismith SG. 2002. A Comment on the Use of Flushing Time, Residence Time, and Age as Transport Time Scales. *Limnol. Oceanogr.* 47:1545-53

Munk W, Sargent M. 1948. Adjustment of Bikini Atoll to waves. *Transactions, Am. Geo. Union* 29:855-60

Oxfam. 2009. The Future is Here: Climate Change in the Pacific, Oxfam Australia/New Zealand, Carlton, Victoria, Austalaia

Pawlowicz R, Beardsley B, Lentz S. 2002. Classical tidal harmonic analysis including error estimates in MATLAB using T_TIDE. *Computers & Geosciences* 28:929-37

Ris R, Holthuijsen L, Booij N. 1999. A third-generation wave model for coastal regions: 2. Verification. *J. Geophys. Res.* 104:7667- 81.

Rodionov SN, Bond NA, Overland JE. 2007. The Aleutian Low, storm tracks, and winter climate variability in the Bering Sea. *Deep Sea Research Part II: Topical Studies in Oceanography* 54:2560-77

Roelvink JA, Banning CKFMv. 1994. Design and development of DELFT3D and application to coastal morphodynamics. In *Hydroinformatics '94*, ed. A Verwey, AW Minns, V Babovic, C Maksimovic. Balkema, Rotterdam: Balkema, Rotterdam

Rooney J, Wessel P, Hoeke R, Weiss J, Baker J, et al. 2008. Geology and geomorphology of coral reefs of the Northwestern Hawaiian Islands. In *Coral Reefs of the USA*, ed. B Riegl, R Dodge. Berlin, Germany: Springer

Stumpf R, Holderied K, Sinclair M. 2003. Determination of water depth with high-resolution satellite imagery over variable bottom types. *Limnol. Oceanogr* 48:547-56

Sutherland J, Peet AH, Soulsby RL. 2004. Evaluating the performance of morphological models. *Coastal Engineering* 51:917-39

Symonds G, Black KP, Young IR. 1995. Wave-driven flow over shallow reefs. *J. Geophys. Res.* 100:2639–48

Tait RJ. 1972. Wave Set-Up on Coral Reefs. *J. Geophys. Res.* 77:2207-11

Thompson K, Bernier N, Chan P. 2009. Extreme sea levels, coastal flooding and climate change with a focus on Atlantic Canada. *Natural Hazards* 51:139-50

Tolman HL. 2002. User manual and system documentation of WAVEWATCH-III version 2.22. , Washington, DC

Trenberth KE, Hurrell JW. 1994. Decadal Atmosphere-Ocean Variations in the Pacifc. *Climate Dynamics* 9:303-19

Warner JC, Butman B, Dalyander PS. 2008. Storm-driven sediment transport in Massachusetts Bay. *Continental Shelf Research* 28:257-82

Warner JC, Geyer WR, Lerczak JA. 2005. Numerical modeling of an estuary: A comprehensive skill assessment. *J. Geophys. Res.* 110:C05001

Webb AP, Kench PS. 2010. The dynamic response of reef islands to sea-level rise: Evidence from multi-decadal analysis of island change in the Central Pacific. *Global and Planetary Change* 72:234-46

White R. 2008. Coastal Inundation and Associated Flooding in Majuro and some of the outer atolls in RMI, National Oceanic and Atmospheric Administration (NOAA), Majuro

Willmott CJ, Davis RE, Feddema JJ, Klink KM, Legates DR, et al. 1985. Statistics for the evaluation and comparison of models. *J. Geophys. Res.* 90:8995-9005

Wolter K, Timlin MS. 1998. Measuring the strength of ENSO events - how does 1997/98 rank? *Weather*: 315-24

Woodroffe CD. 2008. Reef-island topography and the vulnerability of atolls to sea-level rise. *Global and Planetary Change* 62:77-96

Woodworth PL, White NJ, Jevrejeva S, Holgate SJ, Church JA, Gehrels WR. 2009. Evidence for the accelerations of sea level on multi-decade and century timescales. *International Journal of Climatology* 29:777-89

5. General Conclusions and implications of research

In broad term, the research presented in the previous chapters adds confirmation to existing knowledge of coral reef hydrodynamics, especially that wave-driven flows are a principle driver of circulation for most coral reefs [*Monismith*, 2007]. This finding of further support is hardly surprising, since coral reefs are generally found in coastal or oceanic (e.g. most atolls) locations in less than 100 m of water. These are areas where the orbital velocities associated with the passage of surface gravity waves are typically by far the most energetic hydraulic motion [*Massel*, 1996], and thus the most energetic motion a particular reef will experience. And as these energetic motions are dissipated along reefs' rugose seaward perimeters, barotropic pressure gradients (wave setup) result, becoming the primary drivers of currents, even quite far from the regions of dissipation (i.e. in the sheltered back-reef and lagoon areas) at many reefs.

The more novel contribution the research presented here is two-fold. First, it shows that hydrodynamic quanta (current velocities, residence times, bed-shear stress, etc.) can be estimated at high spatial and temporal resolutions (at the reef scale) with reasonable accuracy. Second, it illustrates the importance of episodic events: that these events may incur hydrodynamics orders of magnitude more energetic than during "normal" conditions.

While researchers have been evolving the ability of numerical models to estimate these hydrodynamic quanta (e.g. *Prager* [1991] and *Kraines et al.* [1999] and more recently by *Lowe et al.* [2009] and *Tamura et al.* [2007]), and numerous other researchers have pointed out the importance of episodic or extreme events [e.g. *Dollar and Tribble*, 1993; *Hench et al.*, 2008; *Madin and Connolly*, 2006; *Maragos et al.*, 1973; *Rooney and Fletcher*, 2005; *Woodroffe*, 2008], to this author's knowledge, the research presented here is the first to numerically model a large range of conditions at coral reefs, at the reef scale, including more extreme events.

This is an important step forward, since beyond providing the ability to predict important physical processes (e.g. island inundation events), it sets the stage for the integration of spatially and temporally discrete hydrodynamic quanta over a range of conditions into models (both conceptual and quantitative) of chemical, ecological, and geological processes. For instance, could the complex morphological response of atoll islands to sea level fluctuations (and rise) described by [*Webb and Kench*, 2010] be predicted? It is difficult to see how without using numerical models with the ability to simulate episodic events as a basis. It is also evident that land use changes may severely impact coral reef health through increased sedimentation [*Fabricius*, 2005]. The nature of the impact and fate of the sediment is heavily dependent on resuspension events and transport [e.g. *Storlazzi et al.*, 2004], which can be effectively modeled, as illustrated Chapter 3. There are many other examples of these models' potential utility. While overall increasing ocean acidification in coming decades seems a certainty [*Doney et al.*, 2009; *Kleypas et al.*, 1999], the complex small scale biogeochemical processes which define its effect on reef building organisms [e.g *Atkinson and Cuet*, 2008; *Langdon and Atkinson*, 2005] are heavily dependent on small scale physical properties and processes which the models presented here can provide estimates of. Still other examples include better understanding recruitment of fish and coral larvae [e.g. *DeMartini et al.*, 2009] and processes affecting water quality [e.g. *Andrefouet et al.*, 2006].

The above examples illustrate how chemical, biological, and physical processes of coral reefs are tightly coupled, with changes in one leading to changes in another, often with considerable feedback. Changes may have considerable impact to human populations, such as when greater amounts of wave energy reach shore when offshore reefs suffer mortality events, leading to shoreline changes, [*Sheppard et al.*, 2005]. Thus, understanding and predicting changes to the tightly coupled coral reef systems is of great importance to coastal communities in tropical and subtropical areas. The modeling techniques presented here are a step towards this ability.

These models are not without there shortcomings, however. At present, the computational costs are high, particularly if one were to attempt simulations on timescales necessary to elucidate certain biological and geological processes. It is also possible that model inaccuracies (on the order of 20% in the work presented here) may be propagated into estimates of other processes, ultimately changing outcomes. These are areas for future research. The most significant shortcoming, however, may lie in the requisite geophysical data. High resolution, accurate bathymetric data and information on sea-bed roughness is required to construct the models and estimates of geophysical time series (wind, waves, tides, etc.) of sufficient resolutions are required to drive them. Model performance, at best, will ultimately be only as good as the data used to inform it. The study sites presented here were graced with a relative abundance of geophysical observations (although poor input wave data was the single largest source of error in Chapter 4). In other areas, particularly more remote oceanic locations, such data may be poor or simply not be available. This provides another example of the importance of earth observations to inform earth science, and the relative dearth of these observations in the ocean [*Alverson and Baker*, 2006].

Despite these shortcomings, the research presented here highlights and improves upon a very powerful tool towards the integrated understanding of the coastal zones of the tropics and subtropics. It is essential to gain a better understanding of how this important and dynamic zone works, not only for the sustainable resource management of the residents of this zone, but also how it fits into the global picture. The need for this understanding is hastened by the likely departures from the historical physical, chemical and ecological conditions as we continue our transition into the Anthropocene [*Zalasiewicz et al.*, 2011].

5.1 References

Alverson, K., and D. J. Baker (2006), Taking the Pulse of the Oceans, *Science*, *314*(5806), 1657-1657.

Andrefouet, S., et al. (2006), Review of solutions for 3D hydrodynamic modeling applied to aquaculture in South Pacific atoll lagoons, *Mar. Pollut. Bull.*, *52*(10), 1138-1155.

Atkinson, M. J., and P. Cuet (2008), Possible effects of ocean acidification on coral reef biogeochemistry: topics for research, *Marine Ecology Progress Series*, *373*, 249-256.

DeMartini, E., B. Zgliczynski, R. Boland, and A. Friedlander (2009), Influences of wind-wave exposure on the distribution and density of recruit reef fishes at Kure and Pearl and Hermes Atolls, Northwestern Hawaiian Islands, *Environmental Biology of Fishes*, *85*(4), 319-332.

Dollar, S. J., and G. W. Tribble (1993), Recurrent storm disturbance and recovery: a long-term study of coral communities in Hawaii, *Coral Reefs*, *12*(3), 223-233.

Doney, S. C., V. J. Fabry, R. A. Feely, and J. A. Kleypas (2009), Ocean Acidification: The Other CO2 Problem, *Annual Review of Marine Science*, *1*(1), 169-192.

Fabricius, K. E. (2005), Effects of terrestrial runoff on the ecology of corals and coral reefs: review and synthesis, *Mar. Pollut. Bull.*, *50*(2), 125-146.

Hench, J. L., J. J. Leichter, and S. G. Monismith (2008), Episodic circulation and exchange in a wave-driven coral reef and lagoon system, *Limnol. Oceanogr*, *53*(6), 2681-2694.

Kleypas, J. A., R. W. Buddemeier, D. Archer, J.-P. Gattuso, C. Langdon, and B. N. Opdyke (1999), Geochemical Consequences of Increased Atmospheric Carbon Dioxide on Coral Reefs, *Science*, *284*(5411), 118-120.

Kraines, S. B., A. Suzuki, T. Yanagi, M. Isobe, X. Guo, and H. Komiyama (1999), Rapid water exchange between the lagoon and the open ocean at Majuro Atoll due to wind, waves, and tide, *J. Geophys. Res.*, *104*(C7), 15635-15653.

Langdon, C., and M. J. Atkinson (2005), Effect of elevated pCO2 on photosynthesis and calcification of corals and interactions with seasonal change in temperature/irradiance and nutrient enrichment, *J. Geophys. Res.*, *110*(C9), C09S07.

Lowe, R. J., J. L. Falter, S. G. Monismith, and M. J. Atkinson (2009), A numerical study of circulation in a coastal reef-lagoon system, *J. Geophys. Res.*, *114*(C6), C06022.

Madin, J. S., and S. R. Connolly (2006), Ecological consequences of major hydrodynamic disturbances on coral reefs, *Nature*, *444*, 477-480.

Maragos, J. E., G. B. K. Baines, and P. J. Beveridge (1973), Tropical Cyclone Bebe Creates a New Land Formation on Funafuti Atoll, *Science*, *181*(4105), 1161-1164.

Massel, S. R. (1996), *Ocean surface waves : their physics and prediction / Stanislaw R. Massel*, World Scientific, Singapore.

Monismith, S. G. (2007), Hydrodynamics of Coral Reefs, *Annu. Rev. Fluid Mech.*, *39*(1), 37-55.

Prager, E. (1991), Numerical simulation of circulation in a Caribbean-type backreef lagoon, *Coral Reefs*, *10*(4), 177-182.

Rooney, J. J. B., and C. H. Fletcher (2005), Shoreline Change and Pacific Climatic Oscillations in Kihei, Maui, Hawaii, *J. Coastal Res.*, *21*(3), 535-547.

Sheppard, C., D. J. Dixon, M. Gourlay, A. Sheppard, and R. Payet (2005), Coral mortality increases wave energy reaching shores protected by reef flats: Examples from the Seychelles, *Estuarine, Coastal Shelf Sci.*, *64*(2-3), 223-234.

Storlazzi, C. D., A. S. Ogston, M. H. Bothner, M. E. Field, and M. K. Presto (2004), Wave- and tidally-driven flow and sediment flux across a fringing coral reef: Southern Molokai, Hawaii, *Continental Shelf Research*, *24*(12), 1397-1419.

Tamura, H., K. Nadaoka, and E. Paringit (2007), Hydrodynamic characteristics of a fringing coral reef on the east coast of Ishigaki Island, southwest Japan, *Coral Reefs*, *26*(1), 17-34.

Webb, A. P., and P. S. Kench (2010), The dynamic response of reef islands to sea-level rise: Evidence from multi-decadal analysis of island change in the Central Pacific, *Global and Planetary Change*, *72*(3), 234-246.

Woodroffe, C. D. (2008), Reef-island topography and the vulnerability of atolls to sea-level rise, *Global and Planetary Change*, *62*(1-2), 77-96.

Zalasiewicz, J., M. Williams, A. Haywood, and M. Ellis (2011), The Anthropocene: a new epoch of geological time?, *Philosophical Transactions of the Royal*

Society A: Mathematical, Physical and Engineering Sciences, *369*(1938), 835-841.